technische universität
dortmund

Dynamic Correlations in One-Dimensional Quantum Magnets at Finite Temperature

—

A Diagrammatic Approach

Dissertation
zur Erlangung des akademischen Grades
Dr. rer. nat.
der Fakultät Physik
der Technischen Universität Dortmund

vorgelegt von
Benedikt Fauseweh
geboren in Paderborn

Lehrstuhl für Theoretische Physik I
Fakultät Physik
Otto-Hahn-Str. 4
Technische Universität Dortmund

2016

1. Gutachter: Prof. Dr. G. S. Uhrig
2. Gutachter: Prof. Dr. I. Eremin

Contents

Abstract

In this thesis we investigate dynamical correlations of spin systems at finite temperature. Especially we focus on the anomalous decoherence effects found previously in experiments of several quantum magnets. We develop and apply a diagrammatic perturbative approach, which incorporates the hard-core bosonic nature of spin excitations. This allows for a computation of the leading low-temperature contributions to the spectral function. The Jordan-Wigner transformation is used to benchmark the approach against exact results of the XX-chain in a strong transverse field. To tackle also more complex problems and vertex corrections we combine the approach with effective models derived by continuous unitary transformations. We perform an in-depth analysis of the approach to assess its properties in the context of conserving approximations in the sense of Baym and Kadanoff. The key result of this thesis is the investigation of two quantum magnets: $BaCu_2V_2O_8$ and $Cu(NO_3)_2 \cdot 2.5\ D_2O$. We show that the anomalous decoherence observed can be traced back to non-trivial scattering processes of the hard-core bosonic excitations. This indicates, that quantum coherence plays a significant role in describing dynamical correlations, even at finite temperature. Finally we show, how additional interactions can be taken into account in the full diagrammatic approach, going beyond a mean-field decoupling.

Kurzzusammenfassung

In der vorliegenden Arbeit werden dynamische Korrelationen in Spin Systemen bei endlicher Temperatur untersucht. Ein besonderer Fokus liegt dabei auf den anormalen Dekohärenzeffekten, die in Experimenten in einer Reihe von Quantenmagneten gefunden wurden. Dazu wird eine diagrammatische Störungstheorie entwickelt und angewendet, die die hard-core bosonische Natur der elementaren Anregungen in Spin Systemen berücksichtigt. Dies erlaubt es die führenden Beiträge in einer Tieftemperaturentwicklung der Spektralfunktion zu identifizieren und zu berechnen. Die Methode wird mithilfe der XX-Kette in einem starken externen Magnetfeld geeicht. Für diese existieren exakte Ergebnisse, die mithilfe der Jordan-Wigner Transformationen bestimmt werden. Um auch komplexere Probleme behandeln und Vertex Korrekturen berücksichtigen zu können, wird die Theorie mit effektiven Modellen kombiniert, die durch eine kontinuierliche unitäre Transformation bestimmt werden. Im Rahmen einer ausführlichen Analyse werden die Eigenschaften der Theorie hinsichtlich erhaltender Näherungen nach Baym und Kadanoff untersucht. Eines der Hauptresultate dieser Arbeit ist die Untersuchung von dynamischen Korrelationen in echten Materialien: $BaCu_2V_2O_8$ und $Cu(NO_3)_2 \cdot 2.5$ D_2O. Es wird gezeigt, dass die anormalen Dekohärenzeffekte auf Streuprozesse der hard-core bosonischen Anregungen zurückgeführt werden können. Dies zeigt, das Quantenkohärenz auch bei endlicher Temperatur einen signifikanten Einfluss auf dynamische Korrelationen haben kann. Zuletzt wird die Theorie auf zusätzliche Wechselwirkungen im effektiven Model erweitert. Hierbei wird die volle diagrammatische Entwicklung des Wechselwirkungsvertex bestimmt, ohne auf eine Mean-Field Näherung zurückzugreifen.

1 Introduction

Understanding and characterizing quantum phenomena in many body systems is a far-reaching research field, allowing us to explore a complete new world of exotic phases and excitations. The importance of this research is underlined by the Nobel Prize in Physics 2016 for the pioneer work of David J. Thouless, F. Duncan M. Haldane and J. Michael Kosterlitz in this field [1–5]. In their decision, the Nobel committee stressed, that the laureates used "advanced mathematical methods" to "study unusual phases, or states, of matter", opening a way for future applications in material science.
In particular strongly correlated materials show unusual electronic and magnetic properties at low temperature, which could be used in new generations of electronics. Especially from a theoretical point of view, the research on quantum coherence and new states of matter has brought numerous surprising results to light, extending previously established concepts of order.
One essential challenge in theory and in application, is the interplay of quantum effects with thermal fluctuations. In many experiments an enormous effort is required to cool down samples and equipment in order to observe a physical process dominantly driven by quantum fluctuations. Famous examples include super conductivity and fluidity [6–8], the integer quantum Hall effect [9] and ultracold bosonic atoms in optical lattices [10]. In contrast, at very high temperature, many quantum aspects are not observable any more, because the system is now dominated by classical statistics and a quantum theory is unnecessary to describe the physics. But in the intermediate regime the combination of thermal and quantum fluctuations can lead to a variety of interesting features [11–14].

1.1 Anomalous quantum coherence in magnets

One specific class of many body systems where quantum, as well as thermal, fluctuations play a significant role, are the magnetic properties of insulators. Typically these systems can be described by spin models, where the spins are localized at the positions of magnetic ions. Especially in the case of low spin quantum number S, quantum fluctuations are important in order to describe the properties of such systems.
Different microscopic interactions in quantum magnets can lead to a wide range of fascinating phenomena, such as quasi-particle fractionalization [15, 16], the spin-Peierls transition [17, 18], quantum phase transitions [19] or Bose-Einstein-Condensation [20].
In order to observe these phenomena, several experimental methods have been devel-

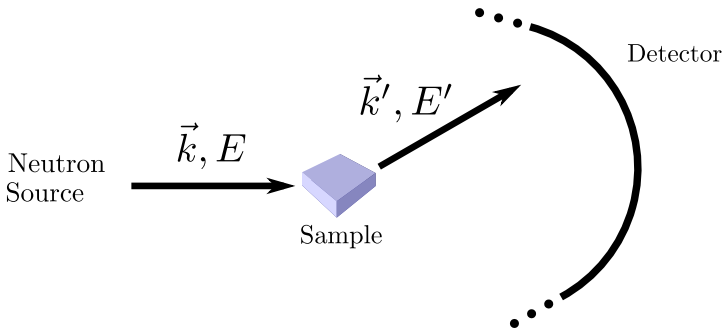

Figure 1.1: Schematic representation of inelastic neutron scattering experiments.

oped. Many of them are based on spectroscopy. While electromagnetic spectroscopy is useful for studying the electronic degrees of freedom, it can only indirectly explore the magnetic degrees of freedom, because the photon has no magnetic moment.
To explore also the magnetic properties of solid state systems in more detail, inelastic neutron scattering (INS) experiments are conducted [21]. In INS experiments a collimated neutron beam is focused on a sample and the scattering of the neutron beam provides information about the physical properties of the sample. The key idea is sketched in Fig. 1.1. In theoretical terms, the intensity of the scattered neutrons as a function of momentum-transfer $\vec{Q} = \vec{k} - \vec{k}'$ and energy-transfer $\hbar\omega = E - E'$ is proportional to the dynamic structure factor $S(\vec{Q}, \omega)$ [21]. The dynamic structure factor is defined as the fourier transform of the time- and space-dependent spin-spin correlation function,

$$S^{xx}(\vec{Q}, \omega) = \frac{1}{N} \sum_{l,n} \int_{-\infty}^{\infty} dt \, \exp[-i(\vec{Q} \cdot \vec{R}_n - \omega t)] \langle S_l^x(t) S_{l+n}^x \rangle. \tag{1.1}$$

In gapped quantum magnets at zero temperature, the dynamic structure factor is typically dominated by a single quasi-particle peak at low energy and weaker multi-particle continua at higher energies.
One specific example for a gapped and strongly correlated quantum magnet is $Cu(NO_3)_2 \cdot 2.5D_2O$ (copper nitrate) [22]. It is an excellent realization of the dimerized spin-1/2 Heisenberg chain, where the ground state of the system is formed by dimers of singlets on the strongest anti-ferromagnetic bonds. Excitations are formed by triplet states (referred to as triplons [23]) confined within a narrow band. The INS spectrum of copper nitrate is shown in Fig. 1.2 from Ref. [24]. It shows a comparison of the experimental data with a theory developed in Ref. [25]. Note that the single quasi-particle peak in Fig. 1.2(c) is the dominating part of the dynamic structure factor.

The dynamic structure factor is directly connected to the spectral function of the system through the fluctuation-dissipation theorem. In theoretical physics the spectral function is an important quantity since it provides valuable information about elementary excitations, their mutual interaction, and many matrix elements of the Hamiltonian. In general the spectral function exhibits δ-peaks at zero temperature in frequency and momentum space at the position of stable quasi-particles in the system.

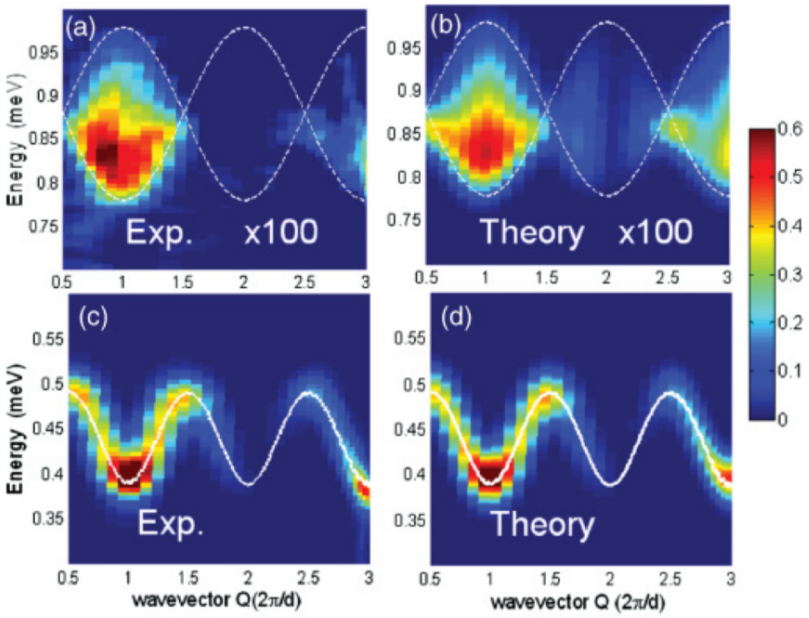

Figure 1.2: Left panel: Neutron scattering spectrum of $Cu(NO_3)_2 \cdot 2.5\ D_2O$ at very low temperature $T \approx 0.12K$ for the single particle mode (c) and the two particle continuum (a) from Ref. [24]. Note that the intensity of the two particle continuum has been multiplied by 100 in order to be visible. Right Panel: Comparison to the theoretical calculation developed in [25].

Upon increasing temperature, a finite density of thermal fluctuations occurs and the propagation of injected quasi-particles is hindered, due to scattering processes with the thermal excitations. This leads to a loss of coherence of the quasi-particles in the time domain and hence to a broadening of the δ-peak in frequency space. In the conventional picture, the decay is purely exponential with a fixed decay rate in the time domain, corresponding to a symmetric Lorentzian spectral function in frequency space. For quantum magnets many studies suggest a universal Lorentzian line shape for gapped as well as gapless excitations [26–31] at low temperature.

However, recent investigations of one-dimensional [24, 32] and three-dimensional [33] materials of coupled spin dimers using INS show, that the line shape in the frequency domain develops an asymmetric tail. Additionally, the positions of the modes seems to shift as a function of temperature, resulting in a band narrowing of the single particle dispersion [34]. One of the first materials where the line shape was investigated intensively is the previously mentioned copper nitrate, see Fig. 1.3. Here we see how single particle peaks in frequency domain broaden as temperature increases. Take note, that the peaks are not symmetric and spectral weight is transferred towards the center of the band.

Similar observations where made in the compound $Sr_3Cr_2O_8$, see Fig. 1.4 from Ref. [33]. This material is also strongly dimerized, but the triplon excitations are not confined to one dimension, due to additional Heisenberg interactions in all three spacial directions. Thus the observed effect is not limited to one dimension, where quantum effects are

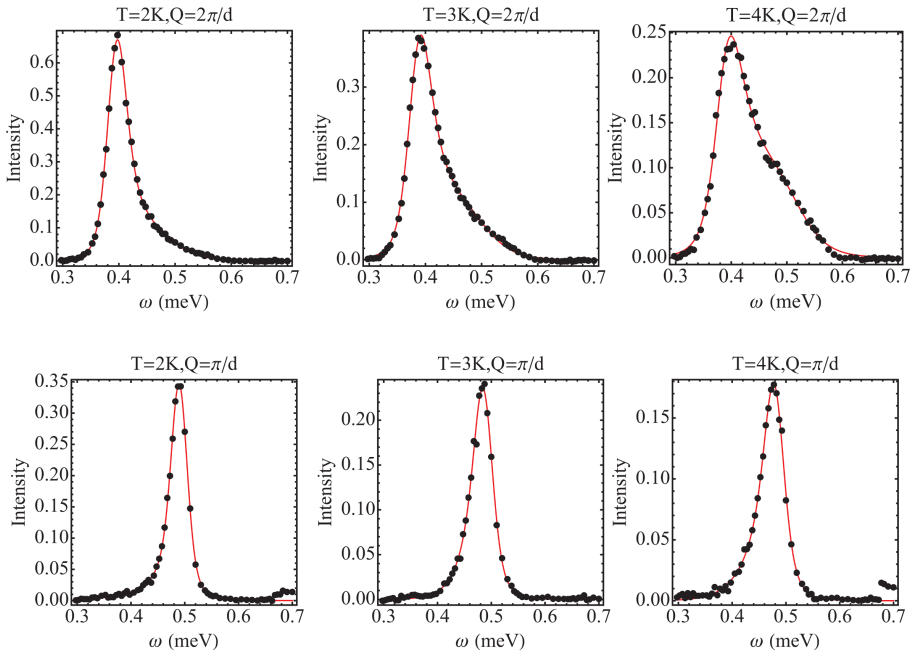

Figure 1.3: Neutron scattering spectrum of $Cu(NO_3)_2 \cdot 2.5\ D_2O$ for the gap mode (upper panel) and the maximum mode (lower panel) of the dispersion. Temperature increases from left to right. Figure taken from Ref. [24].

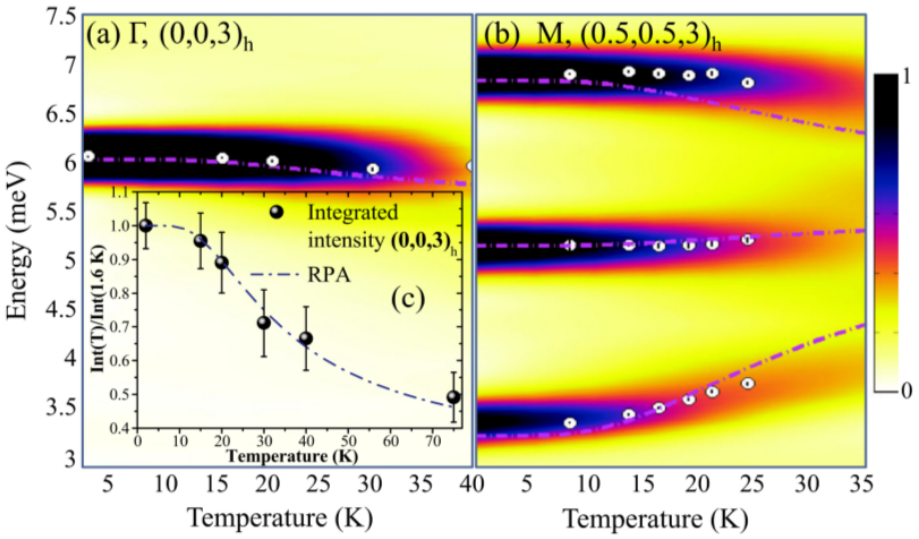

Figure 1.4: INS spectrum of $Sr_3Cr_2O_8$ at $(0, 0, 3)$ (a) and $(0.5, 0.5, 3)$ (b) and the integrated density at $(0, 0, 3)$ (c). Dashed lines result from an random phase approximation. Figure taken from Ref. [33]

particularly strong.

These studies show, that the conventional picture of thermal decoherence is not valid for a broad range of quantum magnets and that the thermal window for universal line shape broadening seems to be much smaller than expected. Although the asymmetric broadening is a subtle effect, it demonstrates that the interplay of finite temperature and quantum coherence extends also to elevated temperatures, which is especially relevant for potential applications in quantum devices.

1.2 Theoretical approaches

In order to explain the specific form of the spectral function at finite temperatures, various theoretical approaches have been applied in the field of quantum magnets. One of them is complete diagonalization to compute the Lehmann representation of the DSF [35,36]. Essler and co-workers developed a variety of approaches based on integrability, Bethe-Ansatz equations and fermionization in Refs. [25,37–40] for one-dimensional systems. Certain thermal effects, such as the narrowing of the dispersion and shifts of spectral weight, can already be captured by mean-field approaches [41]. The combination of integrability and density-matrix renormalization is a very successful strategy where applicable [42]. Recently an advanced numerical approach was developed, based on density-matrix renormalization formulated in matrix product states directly in frequency space [43].

The above listed methods rely essentially on the one-dimensionality of the system under study. In principle, the complete diagonalization can be applied to any dimension. But the tractable system size measured in the linear extension becomes very small for dimensions higher than one. Thus, recent finite temperature experiments on 3D materials [33] cannot be described by these approaches. A $1/z$ expansion with z being the coordination number by Jensen [44] agrees remarkably with the experimental data. The underlying idea relies on a description of the scattering of the elementary excitations with an effective medium [45–47]. The caveat of the approach is, that it is unclear how it can be systematically extended beyond the linear order in $1/z$. Already in this linear order, non-physical double poles have to be eliminated by a plausible assumption in order to preserve causality.

At zero temperature it is often advantageous to describe the low energy physics of a solid state system by deriving an effective model for quasi-particles the number of which is conserved or almost conserved. Such models can result for instance from various renormalization procedures [48,49], continuous unitary transformations (CUTs) [50–53], and variational approaches based essentially on intuition [54,55] and on matrix product states (MPS) [56–58].

Generically, the quasi-particles in quantum magnets are hard-core bosons, i.e. they behave like normal bosons on different lattice sites, but at one site only a single excitation is allowed at maximum [51]. A variety of elementary hardcore bosonic excitations exist in quantum magnets, e.g., spin-flip excitations in polarized systems [59], domain walls in one-dimensional systems with degenerate ground states [60], or triplon excitations in strongly dimerized systems [23]. In contrast to free bosons or free fermions, the thermal properties of hardcore bosons are unknown and non trivial even if they are not subject to further interactions.

Although the effective models describe the dynamics of the hard-core bosons at zero temperature, they do not address the thermal effects directly, which renders quantitative comparisons with experiments more difficult.

In this thesis we want to investigate the main mechanism behind the line shape broadening of hard-core bosons in quantum magnets. In order to do so, we develop and apply a diagrammatic perturbative approach based on a low-temperature expansion which does not require a particular dimensionality. A key ingredient for the applicability of the advocated approach is the direct combination with the aforementioned effective models at $T = 0$ derived by other methods. Thus combining the high precision description of quantum fluctuations at zero temperature with the flexibility of diagrammatic perturbation theory.

This thesis is set up as follows. In the next chapter 2, we will introduce the diagrammatic approach and derive the equations to calculate the spectral function. In chapter 3 we will benchmark the approach using the XX-chain in a strong transverse field. Then we will extend the approach in chapter 4 to treat additional interactions in a mean-field approach, and to include flavored excitations as well. There we will also study finite temperature vertex corrections to the structure factor, using the transverse field Ising model as an example. Next we will combine the diagrammatic approach with two experimental measurements of quantum magnets in chapters 5 and 6. In chapter 7 we will further extend the approach to include additional interactions beyond the simple mean-field approximation in a full diagrammatic treatment. Finally we will conclude in chapter 8.

2 Diagrammatic Brückner approach

For hard-core bosonic systems the diagrammatic Brückner theory for thermal fluctuations is derived in this chapter. First we give a short introduction to the key ideas of the Brückner approach in section 2.1. Next we discuss the properties of the models to which the approach is applied in section 2.2. Section 2.3 derives the main equations for the Brückner approach at finite temperatures and in section 2.4 the approach is extended to include all self-consistent diagrams. Finally some important details on the implementation are given in section 2.5.

Parts of this chapter have been published in Physical Review B as a regular article [61][1]. The manuscript and the interpretation of the data contain contributions from Götz S. Uhrig, Joachim Stolze and myself. Additionally I implemented the equations for the Brückner approach and created all figures.

2.1 Introduction

Understanding and calculating the finite temperature effects in correlated quantum systems is a complicated problem. Especially for temperatures where thermal and quantum fluctuations are of equal strength, the interplay between these two effects make it difficult to obtain a systematic starting point for a calculation. Hence many approaches rely on other restrictions, such as low dimensionality or finite system size, to potentially obtain a valid description of the physics.
On the other hand, a variety of methods to calculate pure zero temperature quantum fluctuations have been developed. In this case the low energy characteristics of a quantum system can often be understood by means of an effective model, which describes the ground state properties as wells as the propagation and interaction of conserved excitations. Because the excitations obtain "particle-like" features, such as an energy gap and momentum, they are often called quasi-particles. This process is an emergent phenomenon, with characteristics depending on the underlying microscopic physics.
The corresponding effective Hamiltonian in terms of creation- and annihilation-operators can be derived systematically by continuous unitary transformations [59, 62–64] or by variational techniques [56–58]. Within the effective model, the ground state of the system is given by the vacuum of excitations and the low energy sector corresponds to

[1]

states with only a few quasi-particles.
At zero temperature, the ground state completely characterizes the static properties of the system, such as ground state energy or total magnetization. Dynamic properties are associated with excitations in the system, the simplest being the energy dispersion of a single quasi-particle.
Closely related to the energy dispersion is the spectral function of a single quasi-particle,

$$A(p,\omega) = \frac{-1}{\pi} \lim_{i\omega_\nu \to \omega + i0^+} \mathrm{Im} \int_0^\beta \mathrm{d}\tau e^{i\omega_\nu \tau} \frac{1}{\sqrt{N}} \sum_l e^{-ipl} G(l,\tau), \tag{2.1}$$

where p denotes momentum, β is inverse temperature, ω denotes frequency and $G(l,\tau)$ is the space and time dependent single particle Green function,

$$G(j,\tau) = -\left\langle \mathrm{T} b_j^\dagger(-i\tau) b_0(0) \right\rangle. \tag{2.2}$$

and N is the system size. Note that τ is the imaginary time and T is the time-ordering super operator.
At zero temperature and if the single quasi-particle block of the Hamiltonian is separated from the ground state and from higher quasi-particle spaces, i.e. by an energy gap or by non-existent matrix elements connecting the different quasi-particle spaces, the spectral function is simply a delta function. It is located at the energy dispersion,

$$A(p,\omega) = \delta(\omega - \omega(p)), \tag{2.3}$$

where $\omega(p)$ is the single quasi-particle dispersion. The delta function signals free quasi-particles that propagate through the system unhindered.
The spectral function is a central quantity in the theory of many-body physics of interacting systems, since it contains all the information of the Green function. It is also directly connected to the dynamic structure factor (DSF) by means of the fluctuation-dissipation theorem,

$$S(p,\omega) = \frac{1}{1 - e^{-\beta\omega}} \left[A(p,\omega) + A(p,-\omega) \right]. \tag{2.4}$$

The DSF is a quantity that can be directly measured in experiments, e.g. in inelastic neutron scattering, opening a way to direct comparison between theoretical calculations on dynamical correlations with experimentally accessible observations.
At finite temperature the situation changes: The system is now characterized by a density matrix, describing a mixing between the ground state and the excited states. Static properties can now be computed using a thermodynamic potential, effectively replacing the role of the ground state energy.
Dynamic properties, such as the spectral function, are affected by temperature effects as well, due to the additional thermal excitations being present in the system.

The aim of the Brückner approach is to capture the finite temperature fluctuations quantitatively on the level of single particle correlations, and to provide a method to calculate the finite temperature spectral function, which is universally applicable in any dimension. A key ingredient for this method are the aforementioned effective models, which describe the zero temperature quantum fluctuations of quasi-particles in the system under investigation. On top of this effective Hamiltonian, we apply the Brückner approach to treat the thermal effects in the spectrum. Thus the zero temperature spectral function provides a well defined starting point for a perturbative approach in the density of thermal fluctuations.
The method is motivated by the Brückner theory, long known in nuclear matter [65] and discussed as the T-matrix approximation in Ref. [66]. But it has also been employed for spin systems at zero temperature by Sushkov and co-workers [67,68]. In these applications, however, the diagrammatic approach was used on *quantum fluctuations*, since the Brückner idea was not applied to a particle-conserving model [69]. This makes its application non trivial even at zero temperature.

2.2 Hard-core bosonic models

A variety of elementary excitations exist in quantum magnets. Although they often result from different microscopic interactions in the Hamiltonian, many of them share similar attributes due to constraints in the Hilbert space. One of these attributes is the hard-core bosonic commutator relation for the creation and annihilation operators of the quasi-particles. Hence these quasi-particles are often called hard-core bosons.
Hard-core bosons behave like normal bosons on different lattice sites, but at one site only a single excitation is allowed at maximum, similar to fermionic excitations. In contrast to free bosons or free fermions, the thermal properties of hardcore bosons are unknown and non trivial even if they are not subject to further interactions.
To introduce the diagrammatic expansion for hard-core bosons, we choose a simple model: a Hamiltonian with no additional interactions besides the hard-core constraint. It is assumed, that no additional quantum numbers are needed to describe the states of the system, besides the occupation number basis. In chapter 4 we will relax these restrictions and explain, how the Brückner approach is modified to include additional quantum numbers and interactions.
In real space the dynamics of a free hard-core bosonic system can be completely described by the bilinear Hamiltonian

$$H = \sum_{i,d} t(d) b_i^\dagger b_{i+d} + \text{h.c.}, \tag{2.5}$$

where $b_i^\dagger$ and b_i are creation and annihilation operators at site i, which fulfill the hard-core boson relation,

$$\left[b_j, b_i^\dagger\right] = \delta_{i,j}\left(1 - 2b_i^\dagger b_i\right). \tag{2.6}$$

Note that these sites can be an element of a lattice in any dimension. The hopping amplitudes $t(d)$ determine the dispersion relation $\omega(p)$ of the hard-core bosons. In the following we assume, that the dispersion has a finite energy gap Δ. The ground state of the system is given by the vacuum of quasi-particles.
Note, that even for this very simple Hamiltonian, the finite temperature spectral function is unknown, due to the complicated form of the local hard-core commutator. Transforming the operators into momentum space,

$$b_p^\dagger = \frac{1}{\sqrt{N}} \sum_j b_j^\dagger e^{ijp} \tag{2.7}$$

yields for the hard-core commutator,

$$\left[b_p, b_{p'}^\dagger\right] = \delta_{p,p'} - \frac{2}{N} \sum_{q_3} b_{q_3-p+p'}^\dagger b_{q_3}. \tag{2.8}$$

This shows, that a local commutation affects all momenta in the Brillouin zone.
Terms that change the number of quasi-particles are not included in the Hamiltonian (2.5), because they would induce additional quantum fluctuations and the vacuum can not be identified as the ground state of the system. It is implied that particle number violating terms have been renormalized to vanish in the effective Hamiltonian. Thus anomalous Green functions, such as

$$G(l,\tau)_{\text{anomalous}} = -\left\langle T b_0^\dagger(-i\tau), b_j^\dagger(0)\right\rangle, \tag{2.9}$$

which change the number of particles, vanish in a particle conserving model.
Take note, that in section 4.1 in chapter 4 we will show, how to obtain an effective particle conserving model based on continuous unitary transformations.
Another important difference between hard-core bosons and normal bosons concerns sum rules for spectral functions. In general the weight of the spectral function is determined by

$$\int_{-\infty}^{\infty} A(p,\omega)\mathrm{d}\omega = \left\langle \left[b_p, b_p^\dagger\right]\right\rangle. \tag{2.10}$$

For normal bosons, the commutator is a constant as a function of temperature and so is the right hand side of the sum rule. In contrast, for hard-core bosons, the hard-core

commutator is given by Eq. (2.8) and the sum rule is modified,

$$\int_{-\infty}^{\infty} A(p,\omega)\mathrm{d}\omega = 1 - 2n(T) \tag{2.11}$$

where $n(T) = \frac{1}{N}\sum_q \langle b_q^\dagger b_q \rangle$ is the thermal occupation function. At zero temperature, $n(T=0) = 0$ holds and the sum rule yields unity like in the bosonic case. The opposite case is at infinite temperature, where $n(T=\infty) = 1/2$ holds: a site is occupied with probability 50% and the spectral weight over all positive and negative frequencies adds up to zero.

2.3 Diagrammatic approach

In this section, we introduce the diagrammatic approach to calculate the spectral function at finite temperatures. For an overview on diagrammatic perturbation theory, we refer the reader to appendix A.

Note, that the free propagator at finite temperature for hard-core bosons is unknown, due to the non-scalar commutator for hard-core bosons in Eq. (2.8). Hence the application of Wick's theorem is non-trivial and no diagrammatic perturbation theory exists for hard-core bosons comparable to the standard Feynman perturbation theory for normal bosons and fermions.

The idea of the Brückner approach is to adapt the standard perturbation theory for normal bosons by enforcing the hard-core constraint not on the operator level but by a local infinite interaction. Thereby we replace the effective Hamiltonian in (2.5) by

$$H \to H_B = H + H_U \qquad\qquad H_U = \lim_{U\to\infty} \frac{U}{2} \sum_i b_i^\dagger b_i^\dagger b_i b_i\,, \tag{2.12}$$

where U is the strength of the auxiliary local repulsion. Note that the repulsion penalizes a double occupancy with an energy U, which is then taken to infinity, to realize the hard-core constraint. Thus we replace all hard-core bosonic operators with normal bosonic operators and all free propagators, without the interaction U,

$$G_0(k, i\omega_k) = \int_0^\beta \mathrm{d}\tau e^{i\omega_k \tau} \frac{1}{\sqrt{N}} \sum_l e^{-ipl} G_0(l,\tau) = \frac{1}{i\omega_k - \omega(k)} \tag{2.13}$$

are trivial also at finite temperature.

In order to use momentum dependent diagrammatic perturbation theory, we transform the Hamiltonian H_B into reciprocal space,

$$H_B = \sum_q \omega(q) b_q^\dagger b_q + \frac{U}{2N} \sum_{q,p,k} b_{p+q}^\dagger b_{-q}^\dagger b_{p+k} b_{-k}. \tag{2.14}$$

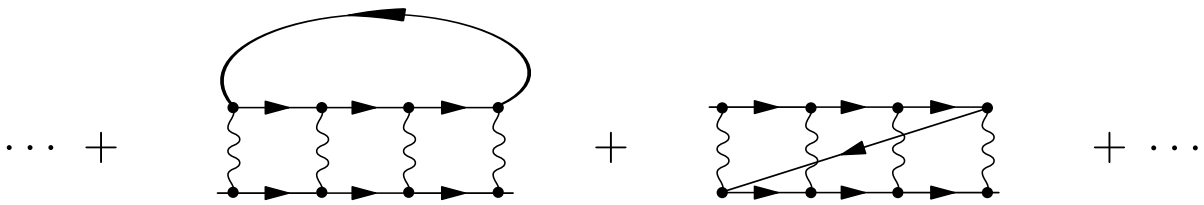

Figure 2.1: Ladder diagrams for the one-particle self-energy

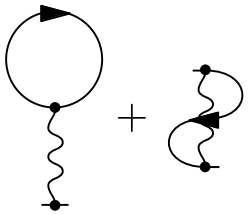

Figure 2.2: Hartree- and Fock-Diagram

Since the interaction is completely local in real space, it scatters all momenta equally in reciprocal space.

On the one hand, the interaction strength is sent to infinity, so that ordinary perturbation theory in U is not a useful starting point for a calculation. On the other hand, at $T = 0$, all self-energy diagrams have a vanishing contribution, because there are no thermal fluctuations present. Consequently, the key concept of the Brückner approach is an expansion in the density of thermal fluctuations. Note that the thermal density is exponentially suppressed if the quasi-particles have an energy gap Δ. The system is treated as a dilute Bose gas, where the density of thermal excitations is the perturbative expansion parameter, aiming at an expansion in the small parameter $\exp(-\beta\Delta)$.

We start by identify all diagrams, that contribute to the single particle self-energy in leading order in the density of thermal excitations. More precisely we identify all diagrams which are of first order in $\exp(-\beta\Delta)$.

One observes, that each propagator running backwards in imaginary time is associated with a Bose function, implying a factor $\exp(-\beta\Delta)$. Thus, in first order, we need to sum all self-energy diagrams with one backward running propagator.

This amounts to the summation of all ladder-diagrams, as depicted in Fig. 2.1. The wiggling lines represent the interaction U, whereas straight lines are free propagators $G_0(k, i\omega_k)$. The interaction is a vertex that has two lines going inwards, representing the annihilation of two hard-core bosons, and two lines going outwards, the two particles which are created. The imaginary time axis goes from left to right, whereas the vertical axis represents the space or momentum dimension.

Note, that all these diagrams have only one propagator backwards in imaginary time, going from the right to the left of the ladder diagrams. The most trivial contribution are the Hartee- and Fock-Diagram given in Fig. 2.2. They have only a single interaction vertex and no propagators running forward in imaginary time.

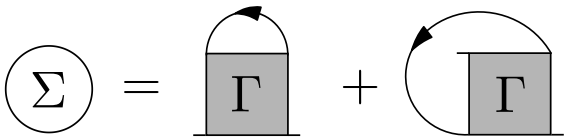

Figure 2.3: Self-energy diagrams in leading order in $\exp(-\beta\Delta)$. The first diagram are Hartree-like diagrams and the second refers to the Fock-like diagrams with a renormalized interaction given by the scattering amplitude Γ.

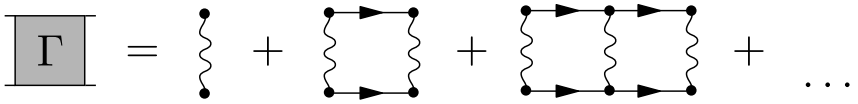

Figure 2.4: Scattering amplitude Γ

Analogously to the single Hartree- and Fock-Diagram, the full contribution from all ladder diagrams can be written compactly by introducing a new effective interaction, see Fig. 2.3. The effective interaction Γ is also called the scattering amplitude, since it describes the infinite scattering process between two particles. It is given by the sum of all ladder diagrams truncated by the propagators running backwards in imaginary time, see Fig. 2.4. Once the scattering amplitude is known, we can calculate the self-energy by evaluating the two contributions given in Fig. 2.3.
It is easily seen that the scattering amplitude is generated by a Dyson-like equation, the Bethe-Salpeter equation, shown in Fig. 2.5. In order to lighten the notation we introduced the 2-momentum

$$P = (p, i\omega_p) \tag{2.15a}$$

and the corresponding summation

$$\sum_P = \sum_p \sum_{i\omega_p}. \tag{2.15b}$$

This notation combines the parameters for Matsubara frequencies and momenta into one single object. If frequency and momentum must be treated separately, we will do so by explicitly writting p and $i\omega_p$ again.
Using the rules of diagrammatic perturbation we can translate the Bethe-Salpeter equation into formulae,

$$\Gamma(P, K, Q) = \frac{U}{N\beta} - \frac{U}{N\beta} \sum_L \Gamma(P, K, L) G_0(P + L) G_0(-L). \tag{2.16}$$

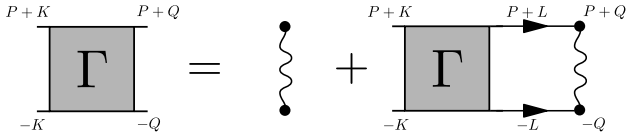

Figure 2.5: Bethe-Salpeter equation for the scattering amplitude with momenta labels.

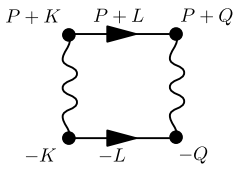

Figure 2.6: Second term in the ladder summation.

The scattering amplitude only depends on total momentum P, due to the simple structure of H_U in reciprocal space. We want to show this property in the follwing: Since the first summand in Fig. 2.4 does not depend on any momentum, we start with the diagram in Fig. 2.6. It translates into the expression

$$-\frac{U^2}{\beta^2}\sum_L G_0(P+L)G_0(-L). \tag{2.17}$$

The pure interaction U is momentum independent so that there is no dependence on the momenta K and Q and the whole expression only depends on total momentum P. Since all ladder diagrams are just concatenated diagrams of the type in Fig. 2.6, we see, that the scattering function also only depends on total momentum,

$$\Gamma(P) = \frac{U}{N\beta} - \frac{U}{N\beta}\sum_L \Gamma(P)G_0(P+L)G_0(-L). \tag{2.18}$$

As a result the Bethe-Salpeter equation can be easily solved for $\Gamma(P)$

$$\Gamma(P) = \frac{U/(N\beta)}{1+UM(P)}, \tag{2.19}$$

where we introduced

$$M(P) = \frac{1}{N\beta}\sum_L G_0(P+L)G_0(-L). \tag{2.20}$$

The function $M(P)$ is a two particle Green function, hence it is at least of order $\mathcal{O}(1/\omega)$ in frequency space, so that a Hilbert representation exists; it reads

$$M(i\omega_p, p) = \int_{-\infty}^{\infty} \mathrm{d}x \frac{\rho_p(x)}{i\omega_p - x}. \tag{2.21}$$

The corresponding spectral function $\rho_p(x)$ can be obtained from the imaginary part of the two particle Green function

$$\rho_p(x) = \frac{-1}{\pi}\lim_{i\omega_p\to x+i\delta}\mathrm{Im}\frac{1}{N}\sum_l \frac{1}{i\omega_p - [\omega(-l)+\omega(p+l)]}\cdot\left(\frac{1}{e^{-\beta\omega(-l)}-1} - \frac{1}{e^{\beta\omega(p+l)}-1}\right) \tag{2.22a}$$

$$= \frac{-1}{N}\sum_l \delta(x - [\omega(-l)+\omega(p+l)])\cdot\left(\frac{1}{e^{\beta\omega(p+l)}-1} - \frac{1}{e^{-\beta\omega(-l)}-1}\right), \tag{2.22b}$$

where the limit implies $\delta \to 0^+$. The Bose functions result from the Matsubara Summation over $i\omega_l$ in Eq. (2.20), we refer the reader to appendix B.1 for details. Note that $\rho_p(x)$ has compact support, given by the two particle continuum

$$\omega_{\text{lower}}(p) = \min_l \left[\omega(-l) + \omega(p+l)\right] \quad \text{and} \quad \omega_{\text{upper}}(p) = \max_l \left[\omega(-l) + \omega(p+l)\right]. \quad (2.23)$$

Since we now have a spectral representation for $M(P)$, the analytical continuation to real frequencies is straight forward.
For $\omega > \omega_{\text{upper}}(p)$ the function $M(\omega, p)$ is purely real and negative, since the spectral function $\rho_p(x)$ is negative. Note that the real part of M can be calculated by the principal value integral

$$\operatorname{Re} M(\omega, p) = \mathcal{P} \int_{-\infty}^{\infty} \mathrm{d}x \frac{\rho_p(x)}{\omega - x}. \quad (2.24)$$

The spectral density $\rho_p(x)$ can be calculated either analytically or numerically for a given dispersion $\omega(k)$. For computational details we refer the reader to section 2.5.
For $T \ll \Delta$ the thermal factor can be expanded according to

$$\left(\frac{1}{e^{\beta\omega(p+l)} - 1} - \frac{1}{e^{-\beta\omega(-l)} - 1}\right) = 1 + \mathcal{O}\left(e^{-\beta\Delta}\right), \quad (2.25)$$

which we will use later.
It is not trivial to take the limit $U \to \infty$ already in Eq. (2.19), because there exists no spectral representation for $\Gamma(P)$ and the expansion of $\Gamma(P)$ in $1/U$ is unclear in its present form. This is one of the main differences to Ref. [70], where the Brückner theory was applied to the double-layer Heisenberg antiferromagnet at finite temperatures. In that model, quantum fluctuations are present, but the imaginary part of the self-energy was neglected and therefore broadening was omitted. Then, the spectral function $A(p, \omega)$ remains a sharp δ-function even at finite temperature, but its position in frequency depends on temperature.
Although there exists no spectral representation for $\Gamma(P)$, there is one for $\Gamma(P) - U$, since $\frac{U}{1+UM(\omega,p)} - U \propto \mathcal{O}(1/\omega)$ holds. It is given by,

$$\frac{U}{1 + UM(\omega, p)} - U = \int_{-\infty}^{\infty} \mathrm{d}x \frac{\bar{\rho}_p(x)}{\omega - x}, \quad (2.26)$$

which again is determined by the imaginary part of the left hand side. Note, that we still assume that U has a finite value, so that the imaginary part reads

$$\frac{-1}{\pi} \lim_{\omega \to x + i\delta} \operatorname{Im}\left[\frac{U}{1 + UM(\omega, p)} - U\right] = \frac{-U^2 \rho_p(x)}{\left[1 + U\mathcal{P}\int_{-\infty}^{\infty} \frac{\rho_p(y)}{x-y}\mathrm{d}y\right]^2 + \left[U\rho_p(x)\pi\right]^2}. \quad (2.27)$$

As long as $\omega \ll U$, we can take the limit $U \to \infty$ and define the spectral function

$$f_p(x) = \frac{-\rho_p(x)}{\left[\mathcal{P}\int_{-\infty}^{\infty} \frac{\rho_p(y)}{x-y}\mathrm{d}y\right]^2 + [\rho_p(x)\pi]^2}, \tag{2.28}$$

which can be directly evaluated using $\rho_p(x)$.
It is important to note, that Eq. (2.28) is not the only contribution to the spectral function of $\Gamma(P) - U$, because for any finite but large value of U, there is another contribution coming from an anti-bound state of two particles with energy $\omega \propto U$. This contribution can be understood intuitively, since for any finite value of U, the effective interaction $\Gamma(P)$ describes an infinite number of scattering processes between two bosons with interaction U. More rigorously, the anti-bound state is signalled by a vanishing denominator in Eq. (2.26) for $\omega \approx U$, because the real part of $M(\omega, p)$ becomes negative in this region.
In the context of our approach, however, it is a mathematical artifact because in the final limit $U \to \infty$ the anti-bound state does not occur directly in any measurable quantity. This would be different in systems where U is very large, but not infinite, for instance for ultracold atoms in optical lattices. We stress, that in spite of the limit $U \to \infty$, which moves the anti-bound to infinity, it leaves traces at finite energies. To our knowledge, this has not been discussed in detail before. We will derive these effects in the following.
Expanding the denominator in Eq. (2.26) for large frequency in $1/\omega$ yields,

$$\frac{U}{1 + UM(\omega, p)} - U \approx \frac{U}{1 + U\rho_0(p)\frac{1}{\omega} + U\rho_1(p)\frac{1}{\omega^2}} - U, \tag{2.29}$$

where $\rho_0(p)$ and $\rho_1(p)$ are the weight and the first moment in frequency space of $\rho_p(x)$, respectively,

$$\rho_0(p) = \int_{-\infty}^{\infty} \rho_p(x)\mathrm{d}x, \tag{2.30a}$$

$$\rho_1(p) = \int_{-\infty}^{\infty} x\rho_p(x)\mathrm{d}x. \tag{2.30b}$$

Based on Eq. (2.22b) it is possible to show, that $\rho_0(p)$ actually does not depend on p. Therefore the p dependence can be ignored in the following calculations. Extracting the imaginary part from Eq. (2.29) leads to

$$\frac{-1}{\pi} \lim_{\omega \to x + i\delta} \mathrm{Im}\left[\frac{U\omega^2}{\omega^2 + U\rho_0\omega + U\rho_1(p)}\right] = \frac{-U}{\pi} \lim_{\omega \to x + i\delta} \mathrm{Im}\left[\frac{\omega^2}{(\omega - \omega_1)(\omega - \omega_2)}\right], \tag{2.31a}$$

where

$$\omega_1 = -\frac{U\rho_0}{2} + \sqrt{\frac{U^2\rho_0^2}{4} - U\rho_1(p)}, \tag{2.31b}$$

$$\omega_2 = -\frac{U\rho_0}{2} - \sqrt{\frac{U^2\rho_0^2}{4} - U\rho_1(p)}. \tag{2.31c}$$

We point out that $\omega_1 = \mathcal{O}(U)$ is the energy of the anti-bound state while $\omega_2 = \mathcal{O}(U^0)$ is a spurious root due to the expansion in $1/\omega$. Next we use Dirac's identity

$$-\pi\delta\left(\omega - \omega_0\right) = \mathrm{Im} \lim_{\delta\to 0^+} \frac{1}{\omega - \omega_0 + i\delta} \tag{2.32}$$

to obtain

$$\frac{-1}{\pi} \lim_{\omega\to x+i\delta} \mathrm{Im}\left[\frac{U\omega^2}{\omega^2 + U\rho_0\omega + U\rho_1(p)}\right] = U\left(\frac{x^2}{x-\omega_2}\delta(x-\omega_1) + \frac{x^2}{x-\omega_1}\delta(x-\omega_2)\right). \tag{2.33}$$

In the following, we can drop the contribution of the spurious root. Combination with Eq. (2.28) yields

$$\bar{\rho}_p(x) = f_p(x) + U\left(\frac{\omega_1^2}{\omega_1 - \omega_2}\delta(x-\omega_1)\right). \tag{2.34}$$

We can now seperate clearly between the low energy contribution $f_p(x)$ and the non trivial high energy anti-bound state.
To finally obtain the single particle self-energy, we calculate the diagrams in Fig. 2.3. Due to the simple structure of the interaction, both diagrams yield the same contribution to the self-energy

$$\Sigma(P) = \frac{-2}{N\beta}\sum_K G_0(K) e^{i\omega_k 0^+}\Gamma(P+K). \tag{2.35}$$

Inserting the spectral representation (2.26) yields

$$\Sigma(P) = \frac{-2}{N\beta}\sum_K G_0(K)\cdot e^{i\omega_k 0^+}\left(\int_{-\infty}^{\infty}\frac{\bar{\rho}_{p+k}(x)}{i\omega_p + i\omega_k - x}\mathrm{d}x + U\right). \tag{2.36}$$

Since we only have a spectral representation for $\Gamma(P) - U$, we have to add the constant U contribution to the self-energy. Note that the constant contribution is actually the pure Hartree and Fock contribution.

Next we sum over all Matsubara frequencies $i\omega_k$, see appendix B.2,

$$\begin{aligned}\Sigma(P) = &\frac{2}{N}\sum_k \frac{U}{e^{\beta\omega(k)}-1} \\ &+ \frac{2}{N}\sum_k \int_{-\infty}^{\infty} U\left(\frac{\omega_1^2}{\omega_1-\omega_2}\delta(x-\omega_1)\right)\frac{1}{i\omega_p-(x-\omega(k))}\left[\frac{1}{e^{\beta\omega(k)}-1}-\frac{1}{e^{\beta x}-1}\right]\mathrm{d}x \\ &+ \frac{2}{N}\sum_k \int_{-\infty}^{\infty} \frac{f_{p+k}(x)}{i\omega_p-[x-\omega(k)]}\left[\frac{1}{e^{\beta\omega(k)}-1}-\frac{1}{e^{\beta x}-1}\right]\mathrm{d}x\end{aligned} \tag{2.37}$$

evaluating the delta distribution yields

$$\begin{aligned}\Sigma(P) = &\frac{2}{N}\sum_k \frac{U}{e^{\beta\omega(k)}-1} \\ &+ \frac{2}{N}\sum_k U\left(\frac{\omega_1^2}{\omega_1-\omega_2}\right)\frac{1}{i\omega_p-(\omega_1-\omega(k))}\left[\frac{1}{e^{\beta\omega(k)}-1}-\frac{1}{e^{\beta\omega_1}-1}\right]\mathrm{d}x \\ &+ \frac{2}{N}\sum_k \int_{-\infty}^{\infty} \frac{f_{p+k}(x)}{i\omega_p-[x-\omega(k)]}\left[\frac{1}{e^{\beta\omega(k)}-1}-\frac{1}{e^{\beta x}-1}\right]\mathrm{d}x\end{aligned} \tag{2.38}$$

Note that both, ω_1 as well as ω_2, depend on U. Hence we expand the second term in $1/U$

$$U\left(\frac{\omega_1^2}{\omega_1-\omega_2}\right)\frac{1}{i\omega_p-(\omega_1-\omega_k)} = U\left(-1+\left[\frac{i\omega_p}{\rho_0}-\frac{\rho_1(p+k)}{\rho_0^2}+\frac{\omega(k)}{\rho_0}\right]\frac{1}{U}+\mathcal{O}\left(\frac{1}{U^2}\right)\right) \tag{2.39}$$

as a result, all terms proportional to U vanish, i.e. the leading contribution of the anti-bound state exactly cancels the Hartee- and Fock-diagram. Now we can easily take the limit $U\to\infty$. Splitting the self-energy into real and imaginary parts leads to

$$\mathrm{Re}\Sigma(p,\omega) = \frac{2}{N}\sum_k\left[\frac{\omega}{\rho_0}-\frac{\rho_1(p+k)}{\rho_0^2}+\frac{\omega(k)}{\rho_0}\right]\frac{1}{e^{\beta\omega(k)}-1}+\mathcal{P}\int_{-\infty}^{\infty}\frac{\rho_{\Sigma,p}(x)}{\omega-x}\mathrm{d}x \tag{2.40a}$$

$$\mathrm{Im}\Sigma(p,\omega) = -\pi\rho_{\Sigma,p}(\omega), \tag{2.40b}$$

where $\rho_{\Sigma,p}(\omega)$ is the spectral function of the self-energy

$$\rho_{\Sigma,p}(\omega) = \frac{2}{N}\sum_k f_{p+k}(\omega+\omega(k))\left[\frac{1}{e^{\beta\omega(k)}-1}-\frac{1}{e^{\beta(\omega+\omega(k))}-1}\right]. \tag{2.40c}$$

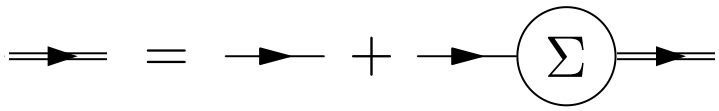

Figure 2.7: Dyson equation for the full propagator

Note that the self-energy in Eq. (2.35) vanishes for $T \to 0$, so that at base temperature the original propagator is recovered. The self-energy defines the full propagator via the Dyson equation, given in Fig. 2.7. The spectral function is given by the imaginary part of the full propagator,

$$A(p,\omega) = \frac{-1}{\pi}\mathrm{Im}G(p,\omega) = \frac{1}{\pi}\frac{\mathrm{Im}\Sigma(\omega,p)}{\left(\omega - \omega(p) - \mathrm{Re}\Sigma(\omega,p)\right)^2 + \left(\mathrm{Im}\Sigma(\omega,p)\right)^2}. \tag{2.41}$$

The real part of the self-energy describes the shift of the peak position due to the interaction with the thermally populated background. The imaginary part describes the broadening of lines of the single excitations due to the hard-core interactions. If the imaginary part of the self-energy has only a negligible dependence on ω, the spectral function $A(p,\omega)$ is a symmetric Lorentzian with full width $2\mathrm{Im}\Sigma$ at half maximum. In chapter 3 we will analyse the diagrammatic Brückner approach in more detail for a simple 1D model.

2.4 Complete self-consistency

One of the main advantages of the Brückner approach is given by the fact, that the ladder diagrams allow for a self-consistent evaluation. Thus the spectral function that enters into the calculation is the same, as the one obtained from the ladder diagrams. In literature this trick was applied in order to improve the results obtained from diagrammatic perturbation theory, since then higher order diagrams are taken into account by the approximation. Strictly speaking the results are correct only in first order of $\exp(-\beta\Delta)$, since the self-consistent calculation contains only an incomplete subset of all higher order diagrams.
Note, that all ladder diagrams are skeleton diagrams, the self-consistent calculation does not over count higher order diagrams. In order to compute the spectral function self-consistently, each bare propagator must be replaced by the fully dressed propagator

$$G(P) = \int_{-\infty}^{\infty} \frac{A(p,x)}{i\omega_p - x}\mathrm{d}x. \tag{2.42}$$

On the diagrammatic level, this means that higher order diagrams are also taken into account, which consist of propagators with self-energy insertions, see Figs. 2.8 and 2.9.

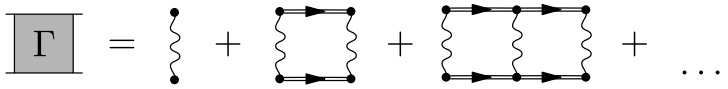

Figure 2.8: Self-consistent ladder summation with the full propagator.

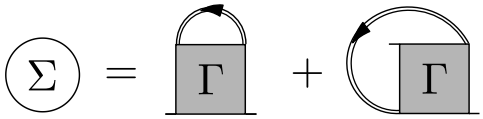

Figure 2.9: Self-consistent self-energy

This changes the calculation of $M(P)$ in (2.20),

$$M(P) = \frac{1}{N} \sum_l \int_{-\infty}^{\infty} \int_{-\infty}^{\infty} \mathrm{d}x \mathrm{d}x' \frac{A_{p+l}(x) A_{-l}(x')}{i\omega_p - (x' + x)} \left(\frac{1}{e^{-\beta x'} - 1} - \frac{1}{e^{\beta x} - 1} \right), \tag{2.43}$$

which leads to a modified expression for $\rho_p(y)$

$$\rho_p(y) = \frac{-1}{N} \sum_l \int_{-\infty}^{\infty} \mathrm{d}x \left(\frac{A_l(x)}{e^{\beta x} - 1} A_{p-l}(y - x) - A_l(x) \frac{A_{p-l}(y - x)}{e^{-\beta(y-x)} - 1} \right). \tag{2.44}$$

Note that Eq. (2.44) is a two-dimensional convolution in the parameters x and l. The calculation of $f_p(x)$ in (2.28) remains unchanged so that $\bar{\rho}_p(x)$ now reads

$$\bar{\rho}_p(x) = f_p(x) + U \left(\frac{\omega_1^2(p)}{\omega_1(p) - \omega_2(p)} \delta(x - \omega_1(p)) \right). \tag{2.45a}$$

where

$$\omega_1(p) = -\frac{U\rho_0(p)}{2} + \sqrt{\frac{U^2 \rho_0(p)^2}{4} - U\rho_1(p)}, \tag{2.45b}$$

$$\omega_2(p) = -\frac{U\rho_0(p)}{2} - \sqrt{\frac{U^2 \rho_0(p)^2}{4} - U\rho_1(p)}. \tag{2.45c}$$

Due to the self-consistency, the weight function $\rho_0(p)$ now depends on total momentum p. The spectral function for the self-energy reads

$$\rho_{\Sigma,p}(y) = \frac{2}{N} \sum_k \int_{-\infty}^{\infty} \mathrm{d}x \left[f_k(x) \frac{A_{k-p}(x - y)}{e^{\beta[x-y]} - 1} - \frac{f_k(x)}{e^{\beta x} - 1} A_{k-p}(x - y) \right], \tag{2.46}$$

which is again a two-dimensional convolution

$$\rho_{\Sigma,p}(y) = \frac{2}{N} \sum_k \int_{-\infty}^{\infty} \mathrm{d}x \left[f_k(x) \frac{A_{-(p-k)}(-(y - x))}{e^{-\beta[y-x]} - 1} - \frac{f_k(x)}{e^{\beta x} - 1} A_{-(p-k)}(-(y - x)) \right]. \tag{2.47}$$

The real and imaginary parts of the self-energy finally read

$$\mathrm{Re}\Sigma(p,\omega) = \frac{2}{N}\sum_k \int_{-\infty}^{\infty} \mathrm{d}x' A_k(x') \left[\frac{\omega}{\rho_0(p+k)} - \frac{\rho_1(p+k)}{\rho_0^2(p+k)} + \frac{x'}{\rho_0(p+k)}\right] \frac{1}{e^{\beta x'}-1} \tag{2.48a}$$

$$+ \mathcal{P}\int_{-\infty}^{\infty} \frac{\rho_{\Sigma,p}(x)}{\omega - x}\mathrm{d}x,$$

$$\mathrm{Im}\Sigma(p,\omega) = -\pi\rho_{\Sigma,p}(\omega). \tag{2.48b}$$

Note that in the self-consistent case, no strict upper and lower boundaries exist for the spectral functions $\rho_p(x)$, $\bar{\rho}_p(x)$ and $\rho_{\Sigma,p}(x)$ since the full propagator can contain long tails in frequency space.

2.5 Implementation

The evaluation of the spectral function in the Brückner theory contains three major steps. First, the spectral function $\rho_p(x)$ must be calculated for a given dispersion. In the one-dimensional case we employ a common identity for the delta distribution composed with a function

$$\rho_p(x) = \frac{-1}{2\pi}\int_0^{2\pi} \mathrm{d}l\delta(x - [\omega(-l)+\omega(p+l)])\left(\frac{1}{e^{\beta\omega(p+l)}-1} - \frac{1}{e^{-\beta\omega(-l)}-1}\right) \tag{2.49a}$$

$$= \frac{-1}{2\pi}\sum_i \frac{1}{|\omega'(-l_i)+\omega'(p+l_i)|}\left(\frac{1}{e^{\beta\omega(p+l_i)}-1} - \frac{1}{e^{-\beta\omega(-l_i)}-1}\right) \tag{2.49b}$$

where $\omega'(l)$ is the derivative of the dispersion with respect to l. The values l_i are the roots of the function $g(l) = x - [\omega(-l)+\omega(p+l)]$.
If $\omega(l)$ has a complicated form, a numerical evaluation of the equation suggests itself. In that case, we discretize frequency and momentum space and evaluate all equations on a grid. For the non self-consistent evaluation, the grid can have an adaptive step size to account for the strongly changing weight in the spectral function. Note that the summation over the Matsubara frequencies has been carried out analytically and no complex continuation from imaginary to real frequencies must be applied.
The roots l_i can be calculated using a one-dimensional root finding algorithm. For higher dimensions this approach can be applied as well, using higher dimensional root finding algorithms. However, we will later see, that the self-consistent calculation offers a much more robust way, to calculate the spectral function efficiently.

In the self-consistent case the calculation can be carried out most effectively on a regular lattice in frequency and momentum space. This is due to the fact that Eq. (2.44) represents a convolution in the variables l and x. It can be calculated using conventional, fast convolution algorithms, based on fast Fourier transforms (FFTs).
The second step is the calculation of $f_p(x)$ in (2.28). Here the main intricacy is the calculation of the principal value. In the self-consistent case it can be carried out efficiently using the tricks proposed by Liu and Kosloff [71].
The third step is the calculation of $\rho_{\Sigma,p}(\omega)$ in (2.40c). In the non-self-consistent case this can be done using standard integration algorithms, while the self-consistent case can again be mapped to a higher dimensional convolution, see (2.47).

3 Results for the nearest neighbor hard-core chain

In this chapter, a simple 1D model is chosen to benchmark and test the diagrammatic Brückner approach. First, we will give an overview of the model and its properties in section 3.1. Next we show, how the dynamics of this simple model can be mapped to Jordan-Wigner fermions and how correlation functions can be evaluated in the fermionic picture, see section 3.2. In section 3.3 we will discuss the real part of the self-energy for the 1D model. Finally, in section 3.4, we will compare the results of the Brückner approach quantitatively to the fermionic results for various observables.

Parts of this chapter have been published in Physical Review B as a regular article [61][1]. The manuscript and the interpretation of the data contain contributions from Götz S. Uhrig, Joachim Stolze and myself. Additionally I implemented the equations for the Brückner approach and I created all figures. Joachim Stolze provided the data for the fermionic results.

3.1 Model

To benchmark the Brückner approach we choose a simple 1D model with nearest neighbor hopping and no additional interactions besides the hard-core constraint. Every site can either be occupied or empty, so that the local Hilbert space is two dimensional. In real space the Hamiltonian reads

$$H = \sum_{i=1}^{N} \left(\Delta + \frac{W}{2}\right) b_i^\dagger b_i - \sum_{i=1}^{N-1} \frac{W}{4} \left(b_i^\dagger b_{i+1} + \text{h.c.}\right), \tag{3.1}$$

where $b_i^\dagger$ and b_i are hard-core bosonic operators at site i. For the Brückner approach the boundary condition do not matter, for the fermionic approach we use open boundary condition.
The Hamiltonian (3.1) consists of a local energy term and a nearest neighbor hopping.

[1]

The energy gap is given by $\Delta > 0$, while $W > 0$ is the band-width of the dispersion

$$\omega(k) = \Delta + \frac{W}{2}\left[1 - \cos(k)\right]. \tag{3.2}$$

Note, that the dispersion is a pure cosine band with the minimum of value Δ found at $k = 0$. The ground state of the system is given by the vacuum state and no quantum fluctuations are present at $T = 0$.
In the following sections we will analyse two cases for the nearest neighbor chain: (i) The narrow band case, where $W < \Delta$ and (ii) the wide band case, where $W > \Delta$. In the narrow band case the group velocity of the excitations is low but with increasing temperature, the band is filled faster than the wide band, since the wide band has more states with higher energy.
An important property of the Hamiltonian in Eq. (3.1) is, that it can be interpreted as an anisotropic spin model, the XX-chain. Note, that $S_i^+ = S_i^x + iS_i^y$ is identical to the hard-core boson creation operator $b_i^\dagger$, see Eq. (2.6). The open-ended N-site $S = 1/2$ XX-chain in a homogeneous magnetic field h is defined by

$$H_{\mathrm{XX}} = -J\sum_{i=1}^{N-1}(S_i^x S_{i+1}^x + S_i^y S_{i+1}^y) + h\sum_{i=1}^{N}(S_i^z + \frac{1}{2}). \tag{3.3}$$

Comparing the Hamiltonians leads to the identification $J = \frac{W}{2}$ and $h = \Delta + \frac{W}{2}$.

3.2 Mapping to Jordan-Wigner fermions

To test the diagrammatic results, we make use of the fact that the hard-core bosonic operators can be mapped to fermions by the Jordan-Wigner transformation [72, 73]

$$c_j = \exp(\pi i\sum_{l<j} b_l^\dagger b_l)b_j, \qquad c_j^\dagger = \exp(-\pi i\sum_{l<j} b_l^\dagger b_l)b_j^\dagger, \tag{3.4a}$$

$$b_j = \exp(-\pi i\sum_{l<j} c_l^\dagger c_l)c_j, \qquad b_j^\dagger = \exp(\pi i\sum_{l<j} c_l^\dagger c_l)c_j^\dagger. \tag{3.4b}$$

The operators $c_j^\dagger$ and c_j fulfill fermionic anti-commutator relations. After a Fourier transformation to reciprocal space, the Hamiltonian (3.1) in terms of fermionic operators reads

$$H = \sum_k \omega(k) c_k^\dagger c_k. \tag{3.5}$$

This mapping is only possible on a chain with open boundary conditions. Cyclic boundary conditions lead to additional interactions in the fermionic language which would make the evaluation much more difficult, if not impossible.
The fermionic ground state is given by the state where all single-particle states with

negative energies are occupied. In our case $h > J$ holds and the ground state is completely empty. In the intermediate field range, $|h| < J$, the ground state is a fermi sea. Note that even though the above fermionic Hamiltonian is diagonal and bilinear, the calculation of dynamic correlations remains a challenging task because of the non-locality of the Jordan-Wigner transformation. In the following we will show how to calculate the spin-spin correlation function $\langle S_i^x(t) S_j^x \rangle$ in space and time domain using the evaluation of Paffians. Then a Fourier transformation is applied to obtain the dynamic structure factor, in order to compare the Brückner approach to the fermionic results.
Using the fermionic identity

$$\exp(i\pi c_l^\dagger c_l) = (c_l^\dagger + c_l)(c_l^\dagger - c_l) \tag{3.6}$$

applied to the Jordan-Wigner transformation (3.4), the correlation function may be expressed in terms of the auxiliary operators $A_l = c_l^\dagger + c_l$ and $B_l = c_l^\dagger - c_l$,

$$\langle S_i^x(t) S_j^x \rangle = \frac{1}{4} \langle A_1(t) B_1(t) A_2(t) B_2(t) ... A_{i-1}(t) B_{i-1}(t) A_i(t) A_1 B_1 A_2 B_2 ... A_{j-1} B_{j-1} A_j \rangle \,. \tag{3.7}$$

Using Wick's theorem [74], the expectation value can be expanded into a product of $2(i+j-1)$ two-point expectation values. The result can be expressed as a Paffian

$$4\langle S_i^x(t) S_j^x \rangle \;=\;$$

$$\left| \begin{array}{ccccccc} \langle A_1(t)B_1(t)\rangle & \langle A_1(t)A_2(t)\rangle & \cdots & \langle A_1(t)A_1\rangle & \langle A_1(t)B_1\rangle & \cdots & \langle A_1(t)A_j\rangle \\ & \langle B_1(t)A_2(t)\rangle & \cdots & \langle B_1(t)A_1\rangle & \langle B_1(t)B_1\rangle & \cdots & \langle B_1(t)A_j\rangle \\ & & \cdots & \cdots & \cdots & \cdots & \cdots \\ & & & \cdots & \cdots & \cdots & \cdots \\ & & & & \cdots & \cdots & \cdots \\ & & & & & \cdots & \cdots \\ & & & & & & \langle B_{j-1}A_j\rangle \end{array} \right| \,. \tag{3.8}$$

where the elements of the Paffian can be easily evaluated using the bilinear Hamiltonian,

$$\langle A_j(t) A_l \rangle = \frac{2}{N+1} \sum_k \sin(kj) \sin(kl) \left[\cos\left(\omega(k)t\right) - i \sin\left(\omega(k)t\right) \tanh\left(\frac{\beta\omega(k)}{2}\right) \right], \tag{3.9a}$$

$$\langle A_j(t) B_l \rangle = \frac{2}{N+1} \sum_k \sin(kj) \sin(kl) \left[i \sin\left(\omega(k)t\right) - \cos\left(\omega(k)t\right) \tanh\left(\frac{\beta\omega(k)}{2}\right) \right]. \tag{3.9b}$$

The numerical evaluation of Paffians is similar to that of determinants. Possible algorithms are described by Derzhko and Krokhmalskii [75] and Jia and Chakravarty [76]. The dynamic structure factor $S^x(q,\omega)$ is the Fourier transform of the dynamic correla-

tion $\langle S_i^x(t)S_j^x\rangle$ with respect to space and time

$$S^x(q,\omega) = \sum_n \int_{-\infty}^{\infty} dt\ \exp[-i(qn-\omega t)]\langle S_l^x(t)S_{l+n}^x\rangle. \tag{3.10}$$

From it we can obtain the spectral function via the fluctuation-dissipation theorem in Eq. (2.4). Since the calculations are done on a finite open-chain, only spins which are sufficiently far away from the boundaries can be considered. Here "sufficiently" means, that for the examined time-span, the propagation of the fermions due to the finite group velocity does not lead to reflections from the chain boundaries. On the contrary, the time span must be as large as possible, to increase the frequency resolution in the Fourier transformation. Hence a trade-off between computation time, which scales as N^4, and frequency resolution must be made. This limits the use of the fermionic approach to higher temperatures, since at low temperatures very sharp features must be resolved in the frequency domain.
All results discussed here are for the gapped case, $|h| > J$ (or $\Delta > 0$). DSF data for the case $|h| < J$ were published some years ago [77] as were results for dimerized XX-chains [78].

3.3 Real part of the self-energy for the cosine band

In this section we will discuss the real part of the self-energy for the pure cosine band, i.e. for the nearest neighbor chain. It turns out, that the leading, linear contribution in $\exp(-\beta\Delta)$ in the general calculations can be evaluated analytically for this case. This allows us to evaluate the real part of the self-energy exactly in this order. First we calculate $\rho_p(x)$ in leading order of $\exp(-\beta\Delta)$

$$\rho_p(x) \;=\; -\frac{1}{\pi}\left[\left[W\cos\left(\frac{p}{2}\right)\right]^2 - [2\Delta + W - x]^2\right]^{-1/2} + \mathcal{O}\left(e^{-\beta\Delta}\right). \tag{3.11}$$

The corresponding real part of $\rho_p(x)$ vanishes if x lies within the two particle band. Using the expansion of $\rho_p(x)$ to calculate the expansion of $f_p(x)$ leads to

$$f_p(x) = \frac{1}{\pi}\sqrt{\left(W\cos\left(\frac{p}{2}\right)\right)^2 - (2\Delta + W - x)^2} + \mathcal{O}\left(e^{-\beta\Delta}\right). \tag{3.12}$$

For the spectral function of the self-energy $\rho_{\Sigma,p}(x)$ we deduce

$$\rho_{\Sigma,p}(x) = \frac{2}{N}\sum_k f_{p+k}(x+\omega(k))e^{-\beta\omega(k)} + \mathcal{O}\left(e^{-2\beta\Delta}\right), \tag{3.13a}$$

where we used the following expansion if the energy x is close to the gap

$$\frac{1}{e^{\beta\omega(k)}-1}-\frac{1}{e^{\beta(x+\omega(k))}-1}=e^{-\beta\omega(k)}+\mathcal{O}\left(e^{-2\beta\Delta}\right), \tag{3.13b}$$

We want to examine the real part of the self-energy describing the shift of the spectral function $A(p,\omega)$. The expansion in $\exp(-\beta\Delta)$ yields

$$\begin{aligned}\operatorname{Re}\Sigma(p,\omega)=\frac{2}{N}\sum_k\left[-\omega-\rho_1(p+k)-\omega(k)+\mathcal{P}\int_{-\infty}^{\infty}\frac{f_{p+k}(x+\omega(k))}{\omega-x}\mathrm{d}x\right]e^{-\beta\omega(k)}\\ +\mathcal{O}\left(e^{-2\beta\Delta}\right),\end{aligned} \tag{3.14}$$

where we made use of the temperature expansion of the weight of ρ

$$\rho_0=-1+\mathcal{O}\left(e^{-\beta\Delta}\right). \tag{3.15}$$

Next we consider $\rho_1(p+k)$ and expand it in $\exp(-\beta\Delta)$

$$\rho_1(p)=\int_{-\infty}^{\infty}\rho_p(x)x\mathrm{d}x, \tag{3.16a}$$

$$=-2\bar{\omega}+\mathcal{O}\left(e^{-\beta\Delta}\right). \tag{3.16b}$$

where $\bar{\omega}$ is the average value of the dispersion in the Brillouin zone, i.e. averaged over momentum p. In case of the cosine band it is given by

$$\bar{\omega}=\Delta+\frac{W}{2}. \tag{3.17}$$

As a last step, the principal value integral in (3.14) reads for the cosine band

$$\mathcal{P}\int_{-\infty}^{\infty}\frac{f_{p+k}(x+\omega(k))}{\omega-x}\mathrm{d}x=\omega-\left[\Delta+\frac{W}{2}(1+\cos(k))\right]+\mathcal{O}\left(e^{-\beta\Delta}\right), \tag{3.18}$$

as long as $|\omega-\left[\Delta+\frac{W}{2}(1+\cos(k))\right]|<|W\cos(p/2+k/2)|$ holds. This is always true for $\omega=\omega(p)$. Inserting eqs. (3.16) and (3.18) into the real part of the self-energy (3.14) yields

$$\operatorname{Re}\Sigma(p,\omega)=0+\mathcal{O}\left(e^{-2\beta\Delta}\right). \tag{3.19}$$

This shows, that the real part of the self-energy vanishes in first order of $\exp(-\beta\Delta)$. Note that this result holds rigorously, since the diagrammatic Brückner approach is correct in first order. As a result, the shift of the spectral function is a second order effect in the expansion parameter $\exp(-\beta\Delta)$. This conclusion is confirmed by evaluating the equivalent fermionic model in the next sections. We will also show in chapter 4, that this result holds in the case of multi-flavor hard-core bosons such as triplons because the

multiplicity of the flavors only affects the prefactor of the self-energy.

3.4 Analysis of the spectral function

In this section we will study the single quasi-particle spectral function of the nearest neighbor chain calculated by the diagrammatic approach. First we gauge the method by comparing it with the numerically exact results obtained from the equivalent fermionic model. Then we apply a more detailed analysis by studying the thermal occupation function, which can be extracted from the single-particle Green function. We will compare the thermal occupation function to various approximations used in literature and to the exact result available due to fermionization. In subsection 3.4.3, we study the real and imaginary parts of the self-energy obtained by the diagrammatic approach and discuss their general features. In the final two subsections 3.4.4 and 3.4.5 we show the finite temperature effects on the spectrum and we will identify the mechanism behind the thermal narrowing of the band and the asymmetry of the spectral peak.

3.4.1 Comparison to the exact fermionic evaluation

To compare the results from fermionization to the Brückner approach we must first map the DSF to the single particle spectral function $A(p,\omega)$ via Eq. (2.4). It turns out that the spectral function has almost no weight for $\omega < 0$ in the parameter regime which we are focusing on. Therefore, we can approximate the relation between $A(p,\omega)$ and $S(p,\omega)$ by

$$S(p,\omega) = \frac{1}{1-e^{-\beta\omega}} A(p,\omega) \ , \ \omega > 0. \tag{3.20}$$

All diagrammatic results presented are calculated self-consistently, if not mentioned otherwise. The spectral function at finite temperature obtained by the fermionic approach and by the diagrammatic Brückner approach is compared in Fig. 3.1, at a temperature of $T = 0.434\Delta$, i.e. $\exp(-\beta\Delta) = 0.100$, and a narrow band-width of $W = 0.5\Delta$. A very good agreement is achieved for the maximum mode at $p = \pi$ but for $p = 0$,i.e. the gap mode, a slight deviation in the peak height is visible. To put this difference into perspective, we consider the following: Since the weight of the spectral function depends only little as function of temperature, see Figs. 3.7 and 3.8, the height of the peak is approximately inversely proportional to the width. The width represents the decay rate of the excitation and is given by the imaginary part of the self-energy. As we have seen, the self-energy is exponentially small in temperature, namely proportional to $\exp(-\beta\Delta)$. Due to this strong dependence on T, even very small inaccuracies of 2% in the gap, which modifies the real part of the self-energy, induces a 5% error in the height. For $\exp(\beta\Delta) = 100$ the relative error would even rise to 10%.

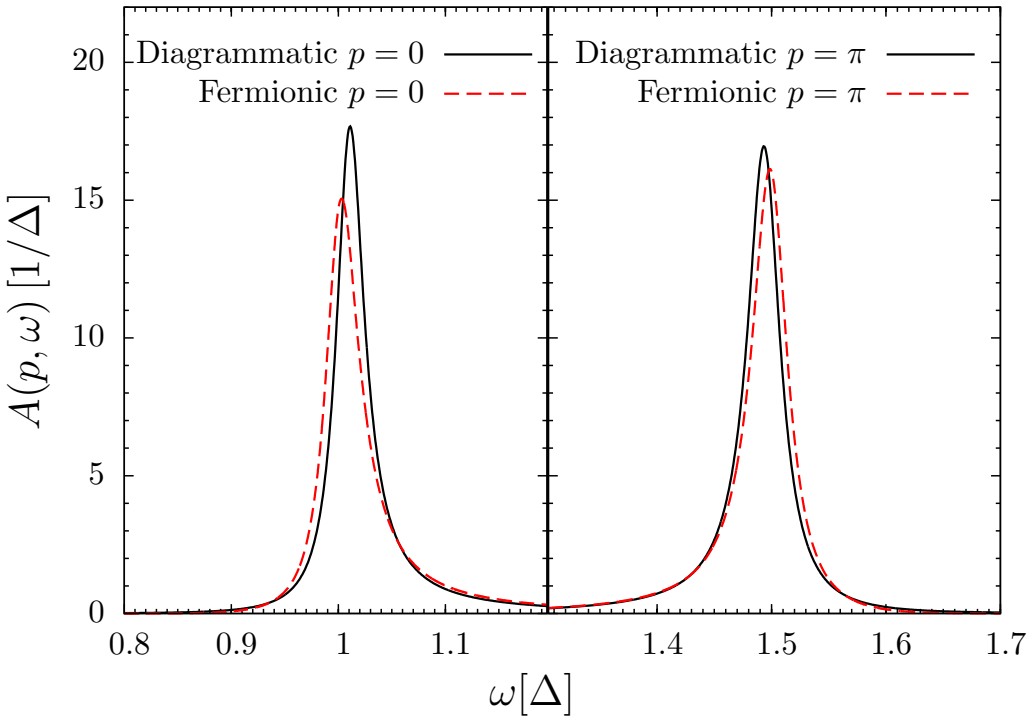

Figure 3.1: Comparison between the spectral function obtained from the fermionic approach and from the diagrammatic expansion. Parameters are $p = 0$ and $p = \pi$ with $W = 0.5\Delta$ and $T = 0.434\Delta$, i.e., $\exp(-\beta\Delta) = 0.100$

.

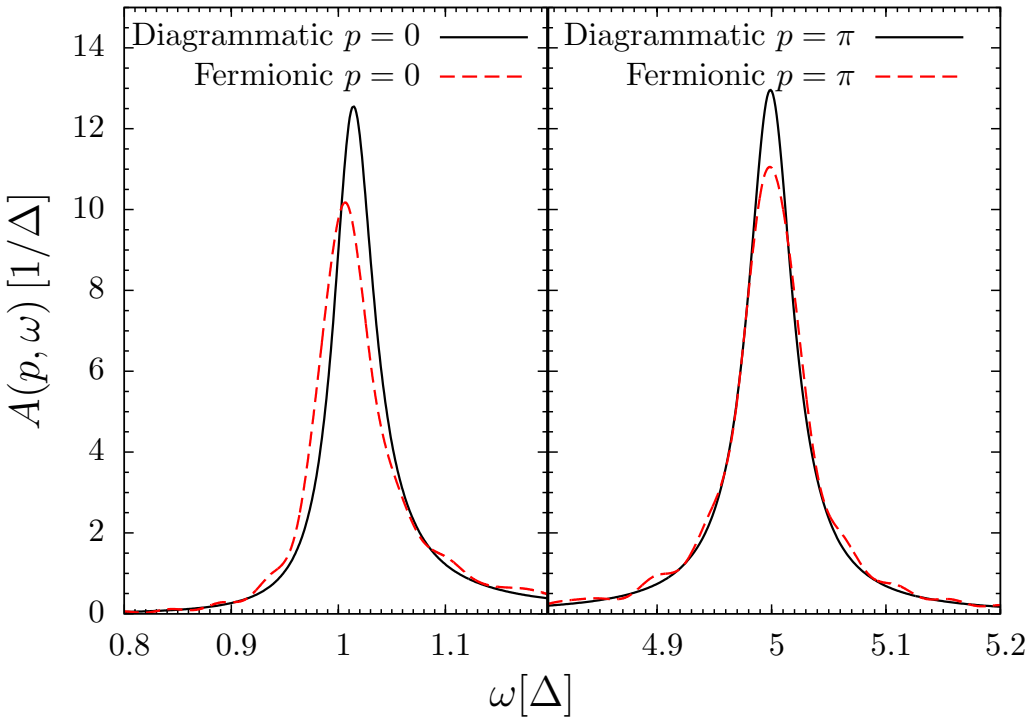

Figure 3.2: Comparison between the spectral function obtained from the fermionic approach and from the diagrammatic expansion. Parameters are $p = 0$ and $p = \pi$ with $W = 4\Delta$ and $T = 0.434\Delta$, i.e., $\exp(-\beta\Delta) = 0.100$

.

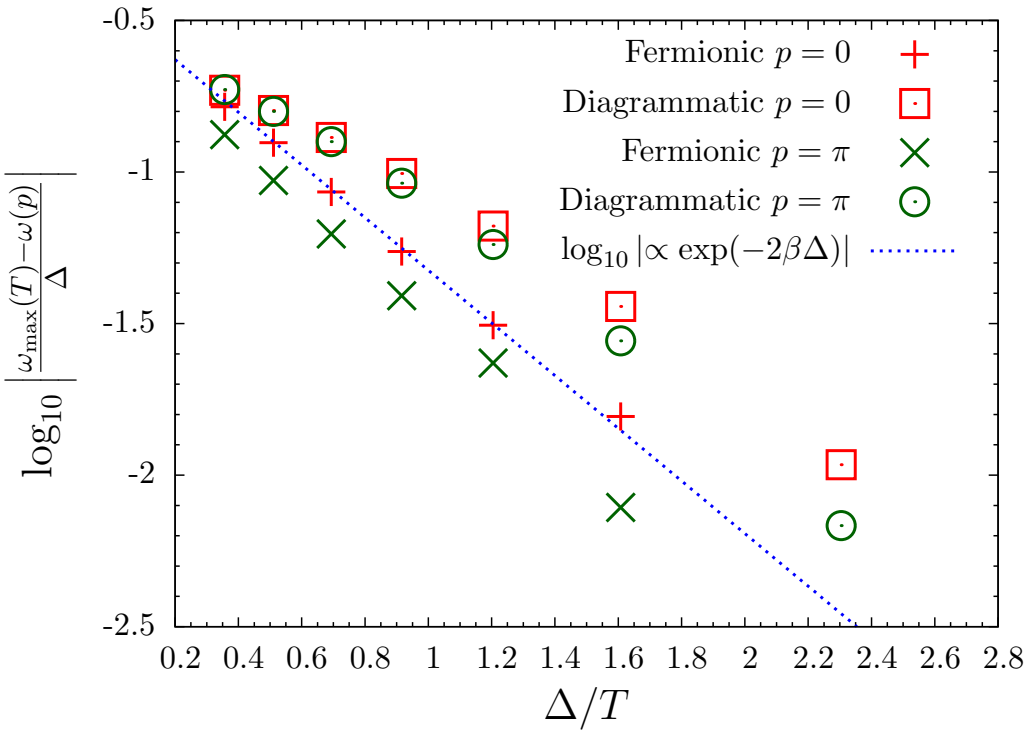

Figure 3.3: Peak shift for $W = 0.5\Delta$ as function of the inverse temperature. Crosses represent results obtained in the fermionic approach while boxes and circles represent results obtained by the diagrammatic expansion. The function $\log_{10}(A \cdot \exp(-2\beta\Delta)$ has been aligned to the data using the parameter A.

We attribute the differences to two sources: (i) The ladder approximation is not able to capture all relevant physical processes at this fairly elevated temperature. (ii) The data obtained in the fermionic approach has a finite resolution in the time domain which implies inaccuracies in the frequency domain. Hence the fermionic approach represents a complementary method to calculate finite temperature spectral functions, working best at high temperature. In view of these considerations the agreement between the two methods is remarkable.

Note that the shift of the peak position is overestimated by the diagrammatic expansion. Since the shift is a second order effect $\exp(-2\beta\Delta)$ for the pure cosine band, the deviations in the Brückner approach are expected. We do not include peaks at lower temperatures because they become very quickly extremely sharp so that it is difficult to evaluate their shape with appropriate numerical precision in the fermionic approach. We emphasize, that by construction the diagrammatic approach becomes better and better for lower and lower temperature.

Figure 3.2 shows the spectral functions for the wide band case $W = 4\Delta$ at finite temperature $T = 0.434\Delta$, i.e., $\exp(-\beta\Delta) = 0.100$. Due to the larger band-width, the group velocity of the excitations is increased and the finite system size in the fermionic evaluation induces additional errors. This is clearly visible in the additional wiggling of the spectral function obtained in the fermionic approach. We want to study the temperature dependence of the peak position in more detail. Figs 3.3 and 3.4 show the shift for

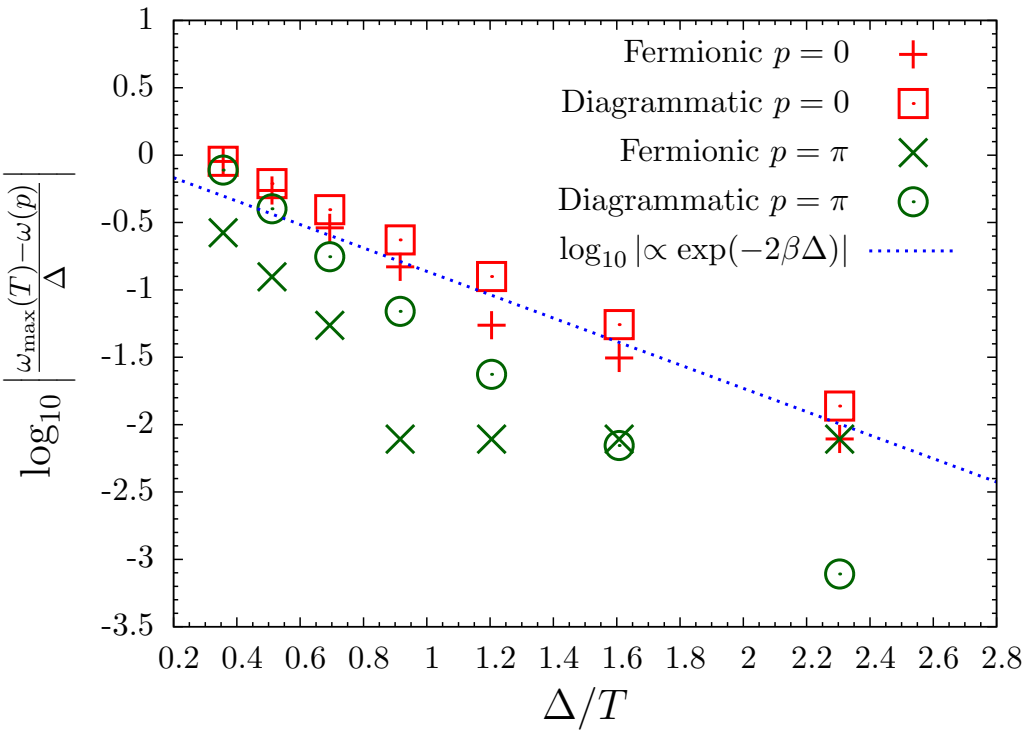

Figure 3.4: Peak shift for $W = 4\Delta$ as function of the inverse temperature. Crosses represent results obtained in the fermionic approach while boxes and circles represent results obtained by the diagrammatic expansion. The function $\log_{10}(A \cdot \exp(-2\beta\Delta)$ has been aligned to the data using the parameter A.

the cases $W = 0.5\Delta$ and $W = 4\Delta$ as function of inverse temperature $1/T$. Note, that although the predicted shift differs between the two methods, they both show, that the shift is a second order effect in $\exp(-\beta\Delta)$. In this order, the diagrammatic Brückner approach is expected to yield incorrect results, due to the missing diagrams in second order perturbation theory. Note that for $W = 4\Delta$ and $p = \pi$ four data points obtained by the fermionic approach show the same shift. This error is caused by the finite frequency resolution used in the fermionic approach. We stress again that the exact fermionic expressions are difficult to evaluate numerically, in particular for low temperatures.

Next the width of the spectral function is investigated by measuring the full width at half maximum (FWHM). Figs. 3.5 and 3.6 show the FWHM for the narrow band and for the wide band case. For low temperatures, the data of both approaches agrees well. Both data sets support our analytic finding in Eq. (2.40b) that the width is a first order effect in $\exp(-\beta\Delta)$.

Upon increasing temperature the diagrammatic expansion underestimates the broadening of the line shape. This can be attributed to the missing diagrams $\propto \exp(-2\beta\Delta)$ not included in our approach. These diagrams describe additional scattering processes increasing the decoherence and broadening the line shape further.

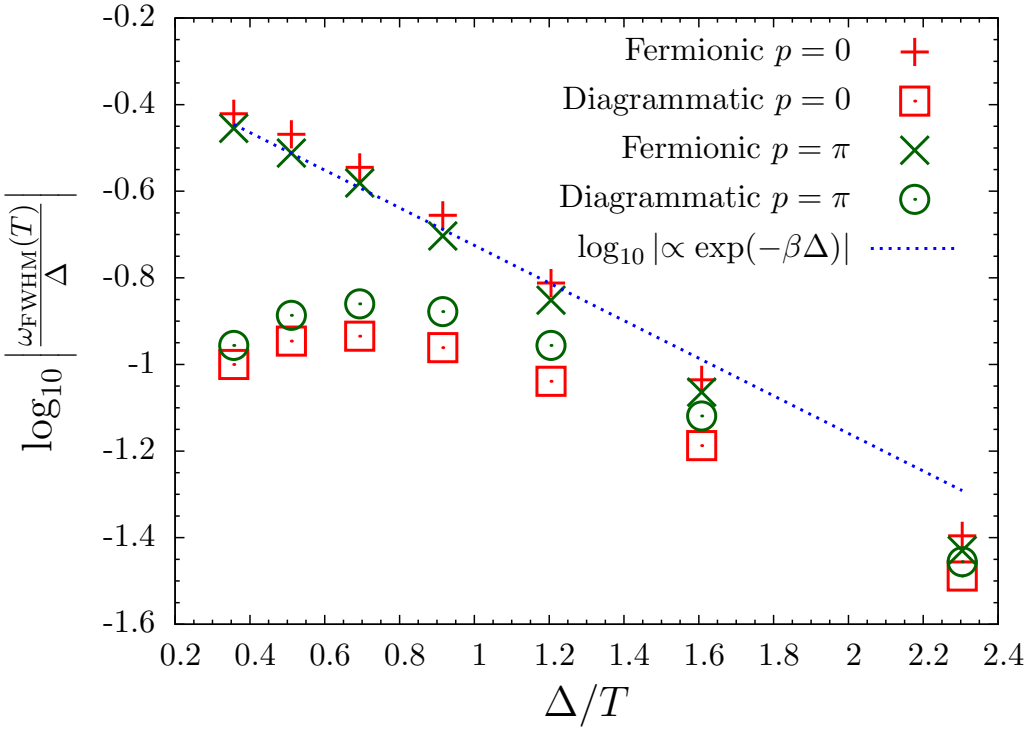

Figure 3.5: Full width at half maximum of the peak for $W = 0.5\Delta$ as function of the inverse temperature. Crosses represent results obtained in the fermionic approach while boxes and circles represent results obtained by the diagrammatic expansion. The function $\log_{10}(A \cdot \exp(-\beta\Delta))$ has been aligned to the data using the parameter A.

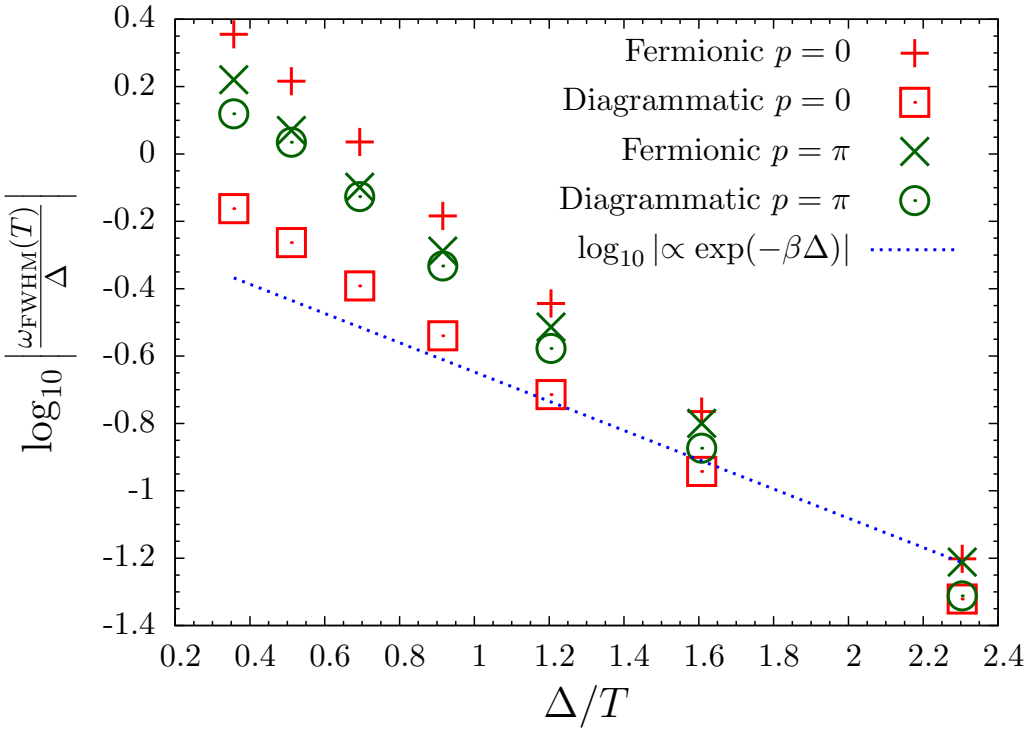

Figure 3.6: Full width at half maximum of the peak for $W = 4\Delta$ as function of the inverse temperature. Crosses represent results obtained in the fermionic approach while boxes and circles represent results obtained by the diagrammatic expansion. The function $\log_{10}(A \cdot \exp(-\beta\Delta))$ has been aligned to the data using the parameter A.

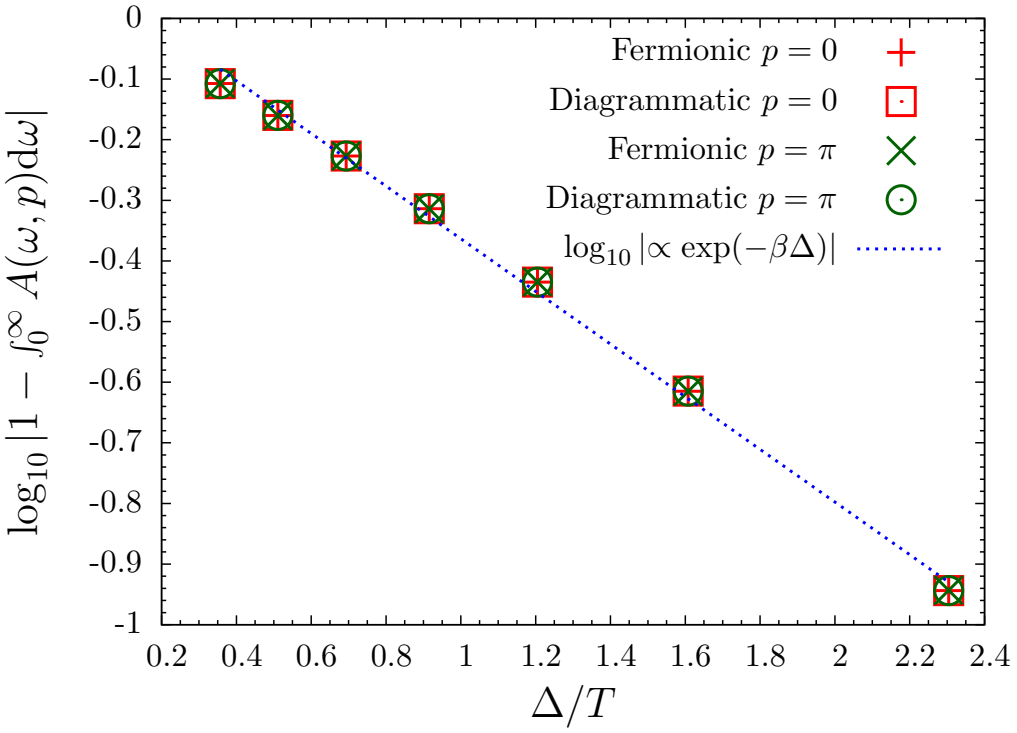

Figure 3.7: Weight of the spectral function for $W = 0.5\Delta$ as function of the inverse temperature. Crosses represent results obtained in the fermionic approach while boxes and circles represent results obtained by the diagrammatic expansion. The function $\log_{10}(A \cdot \exp(-\beta\Delta))$ has been aligned to the data using the parameter A.

For $W = 0.5\Delta$ and very high temperatures we even see that the broadening obtained from the ladder approximation decreases, which clearly indicates that the ladder diagrams no longer capture the dominant scattering processes.

Finally, we consider the temperature dependence of the weight of the spectral function. More specifically, we plot the deviation from unity in logarithmic scale $\log_{10}(1 - \int_{-\infty}^{\infty} A(p, \omega))$ for the narrow band in Fig. 3.7 and for the wide band in Fig. 3.8 versus the inverse temperature. For both cases an amazing agreement between the two methods is found.

A possible explanation for this observation is, that the ladder diagrams provide a conserving approximation for normal bosons in the sense of Baym and Kadanoff [79, 80]. These are approximation made on the level of self-energy diagrams, which can be deduced from a variation of a generating functional. If this function obeys certain symmetry condition, the resulting approximation for the single particle propagator obeys conservation laws for number, energy and momentum.

Since we have already shown in Sect. 3.1 that the weight of the spectral function is directly connected to the thermal occupation, see Eq. (2.11), we expect that the thermal occupation is captured very accurately by the diagrammatic expansion in agreement with the exact fermionic results, see also next subsection.

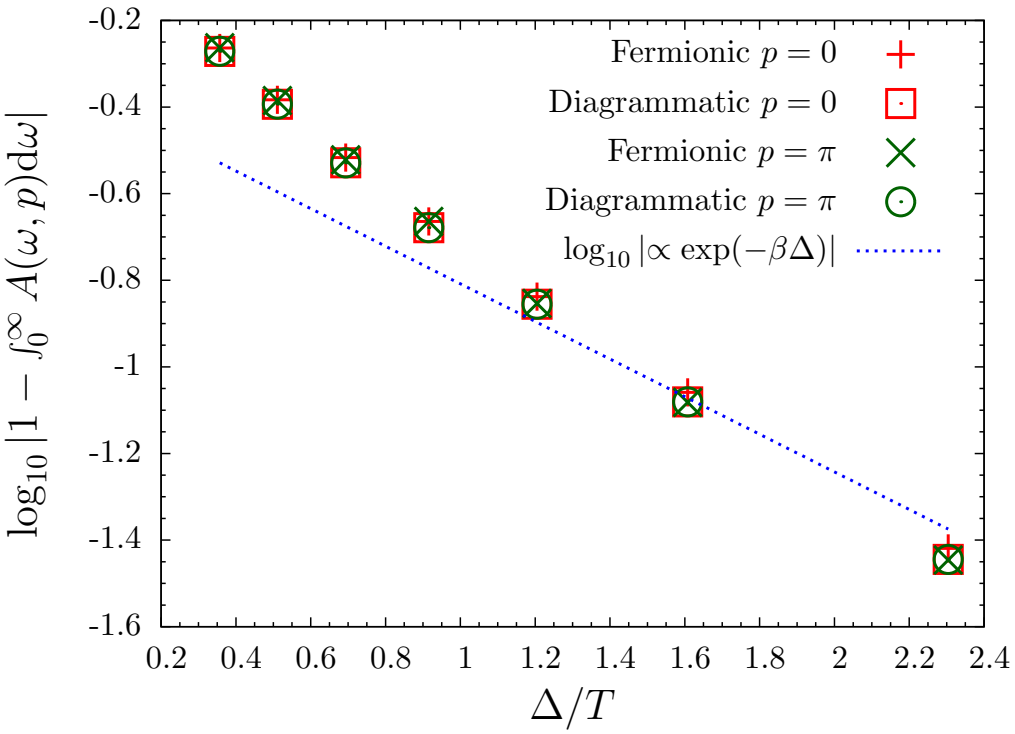

Figure 3.8: Weight of the spectral function for $W = 4\Delta$ as function of the inverse temperature. Crosses represent results obtained in the fermionic approach while boxes and circles represent results obtained by the diagrammatic expansion. The function $\log_{10}(A \cdot \exp(-\beta\Delta))$ has been aligned to the data using the parameter A.

3.4.2 Thermal occupation

Here we focus on the thermal occupation which can be determined from the spectral function by evaluating the integral

$$n(T) = \frac{1}{2\pi}\int_0^{2\pi} \langle b_k^\dagger b_k\rangle \mathrm{d}k = \int_0^{2\pi}\int_{-\infty}^{\infty} \frac{A(k,\omega)}{e^{\beta\omega}-1}\mathrm{d}\omega\mathrm{d}k. \tag{3.21}$$

Since the Jordan-Wigner Transformation maps the hard-core bosons to fermions without interaction, the exact expression for the thermal occupation is easily available

$$n(T) = \frac{1}{2\pi}\int_0^{2\pi} \langle b_k^\dagger b_k\rangle \mathrm{d}k = \frac{1}{N}\sum_i \langle b_i^\dagger b_i\rangle \tag{3.22a}$$

$$= \frac{1}{N}\sum_i \langle c_i^\dagger c_i\rangle = \frac{1}{2\pi}\int_0^{2\pi} \frac{1}{e^{\beta\omega(k)}+1}\mathrm{d}k. \tag{3.22b}$$

It is not possible to calculate the momentum dependent thermal occupation analytically, because it includes many-particle correlation functions in the fermionic picture, see Sec. 3.2.

A crude estimate for the occupation function of hard-core bosons was proposed in Ref. [81],

$$n(T,k)_{\mathrm{app}} = \frac{e^{-\beta\omega(k)}}{1+z(T)}, \tag{3.23}$$

where $z(T) = \sum_k \exp(-\beta\omega(k))$. It is correct for flat bands, i.e. $W = 0$, but often used as a first approximation also in the case of dispersive bands, see for instance Refs. [41,82]. The approximate thermal occupation can be obtained by integration over k, it reads

$$n(T)_{\mathrm{app}} = \frac{z(T)}{1+z(T)}. \tag{3.24}$$

We call the thermal occupation approximate hard-core statistics below because it only captures the local aspects of repelling bosons. The approximate statistics captures the correct values for $T = 0$ and $T = \infty$ for nonzero band-width. We therefore expect deviations from the exact expression to appear for moderate temperatures $T \sim \Delta$ and wide bands $W \gg \Delta$. The thermal occupation for the narrow band $W = 0.5\Delta$ is depicted in Fig. 3.9. For low T the precise statistics does not matter, so that even the free boson statistics

$$n(T)_{\mathrm{boson}} = \frac{1}{2\pi}\int_0^{2\pi} \frac{1}{e^{\beta\omega(k)}-1}\mathrm{d}k \tag{3.25}$$

captures the correct behaviour. This changes distinctively at higher temperatures. The occupation number for free bosons has no bound for rising temperature, while for hard-core bosons the limit $n(T=\infty) = 1/2$ has to be fulfilled. Therefore the free boson approximation breaks down at $T \gtrsim 0.3\Delta$. The non-self-consistent calculation improves the statistics beyond this point, but also breaks down once temperature reaches $T \gtrsim 0.6\Delta$. Fortunately, the self-consistent calculation stays very close to the exact result, even for temperatures far above the energy gap. For the narrow band the approximate statistics $n(T)_{\mathrm{app}}$ is indistinguishable from the exact curve.

Figure 3.10 shows the thermal occupation for the wide band $W = 4\Delta$ for the same temperature range as in the narrow band case. The thermal occupation does not grow as fast as for the narrow band due to the larger energy scale W. The free boson approximation holds up to $T \approx 0.4\Delta$ while the non-self-consistent calculation is correct up to $T \approx 0.8\Delta$. Again the self-consistent solution agrees excellently with the exact result, while the approximate statistics $n(T)_{\mathrm{app}}$ overestimates the occupation for temperatures above $T \approx 0.6\Delta$. For temperatures $T \gg \Delta + W$ (not shown) the approximate statistics and the exact curve merge again.

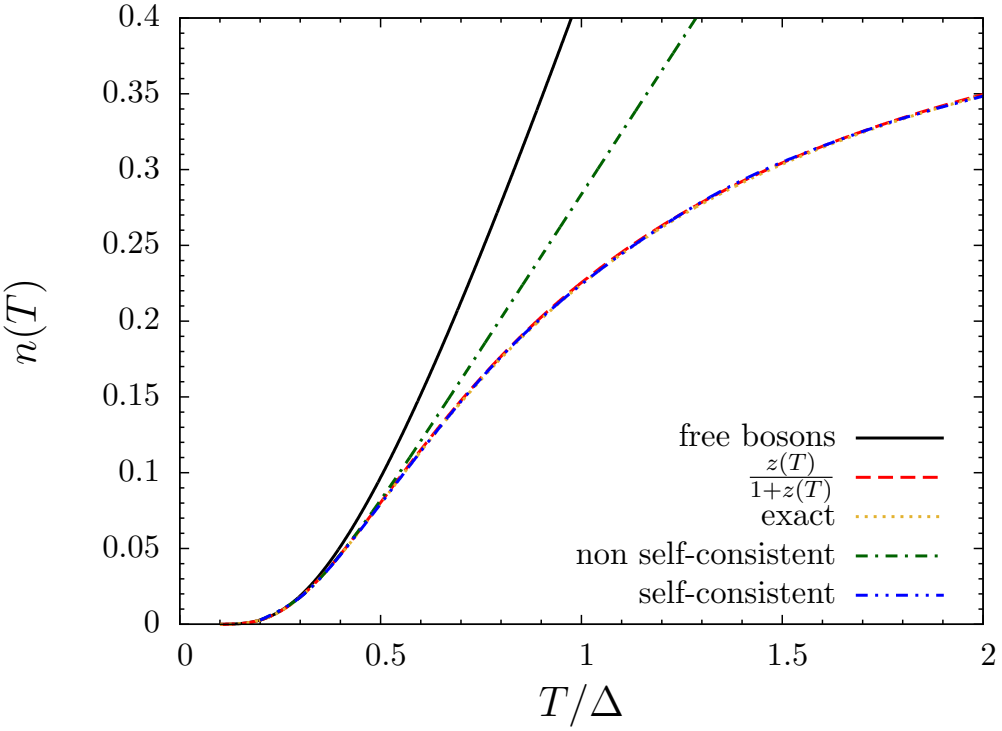

Figure 3.9: Temperature dependence of the occupation function for $W = 0.5\Delta$. Comparison between a simple bosonic approximation, the non-self-consistent solution, the self-consistent solution, the approximate statistics from Ref. [81], and the exact fermionic expression.

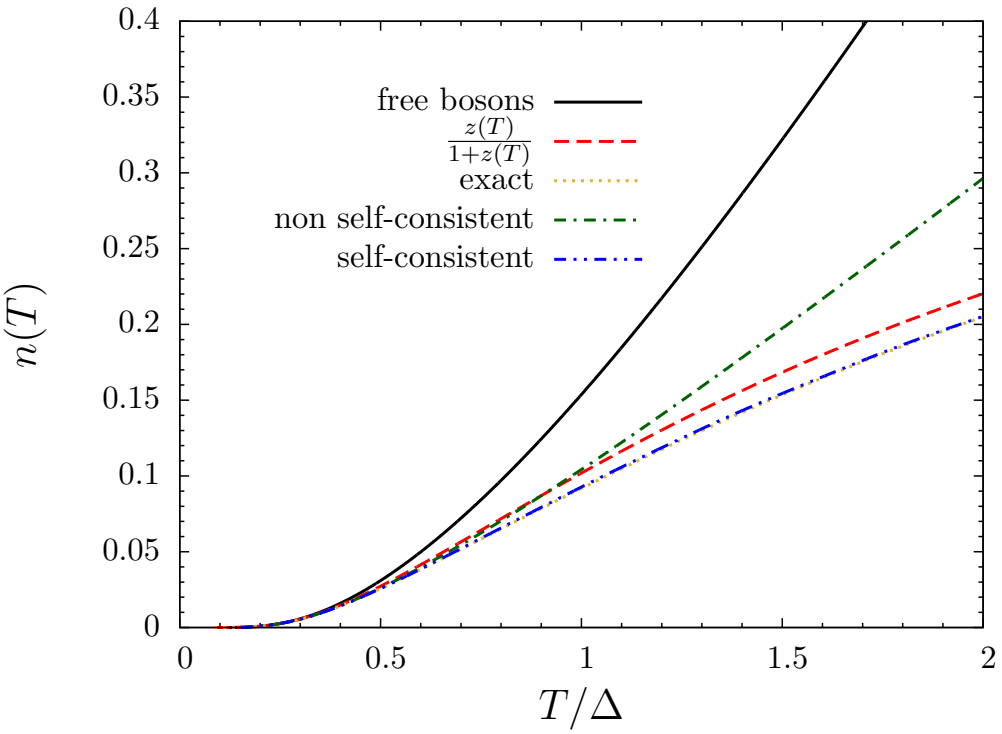

Figure 3.10: Temperature dependence of the occupation function for $W = 4\Delta$. Comparison between a simple bosonic approximation, the non-self-consistent solution, the self-consistent solution, the approximate statistics from Ref. [81], and the exact fermionic expression.

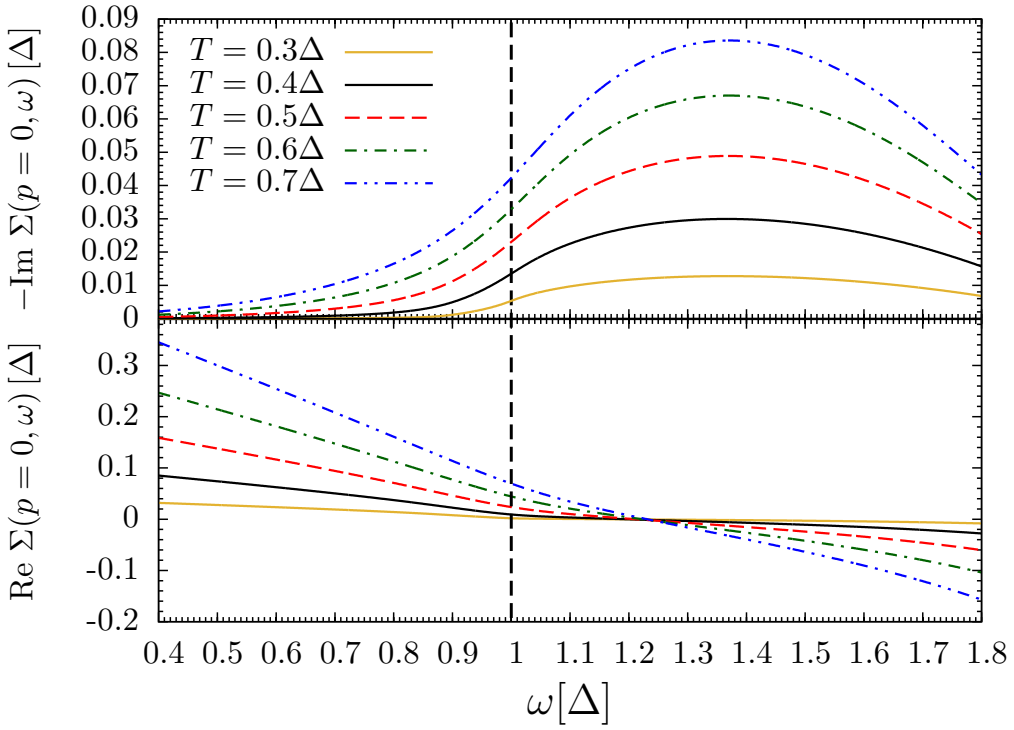

Figure 3.11: Real and imaginary part of the self-energy $\Sigma(p,\omega)$ at various temperatures for the gap mode at $p = 0$ and for $W = 0.5\Delta$. The vertical line indicates the energy of the $p = 0$ mode at zero temperature.

3.4.3 Details of the diagrammatic approach

In the previous subsection we benchmarked the diagrammatic approach by comparing it to the exact fermionic results. In the present subsection, we discuss the results of the diagrammatic expansion for various temperatures and band-widths in more detail. As before, we restrict ourselves to the self-consistent solutions.

Even though self-consistency improves the results, we still require that the temperature is not too high, so that higher order processes can be neglected. We stress that the single particle gap Δ is the most important energy scale, but also the band-width W at zero temperature plays an important role. Especially for the same temperature T in units of the gap Δ, the narrow band limit $W \lessapprox \Delta$ and the wide band limit $W \gtrapprox \Delta$ can differ significantly, because narrow bands generically allow for a much larger fraction of thermal excitations, i.e., a higher density of thermally excited hard-core bosons, than wide bands.

In Figs. 3.11 and 3.12 we investigate the real and the imaginary part of the self-energy for the gap mode and for the maximum mode, respectively, in case of the narrow band $W = 0.5\Delta$. The imaginary part is dominated by the two-particle continuum convoluted with the single particle Green function, see Eq. (2.36). Upon increasing temperature the imaginary part gains weight. We clearly see for $\omega = \omega(p)$, that the imaginary part is not well approximated by a constant but rather by a linear function, leading to an asymmetric line shape of the spectral function $A(p,\omega)$. While the gap mode shows a tail

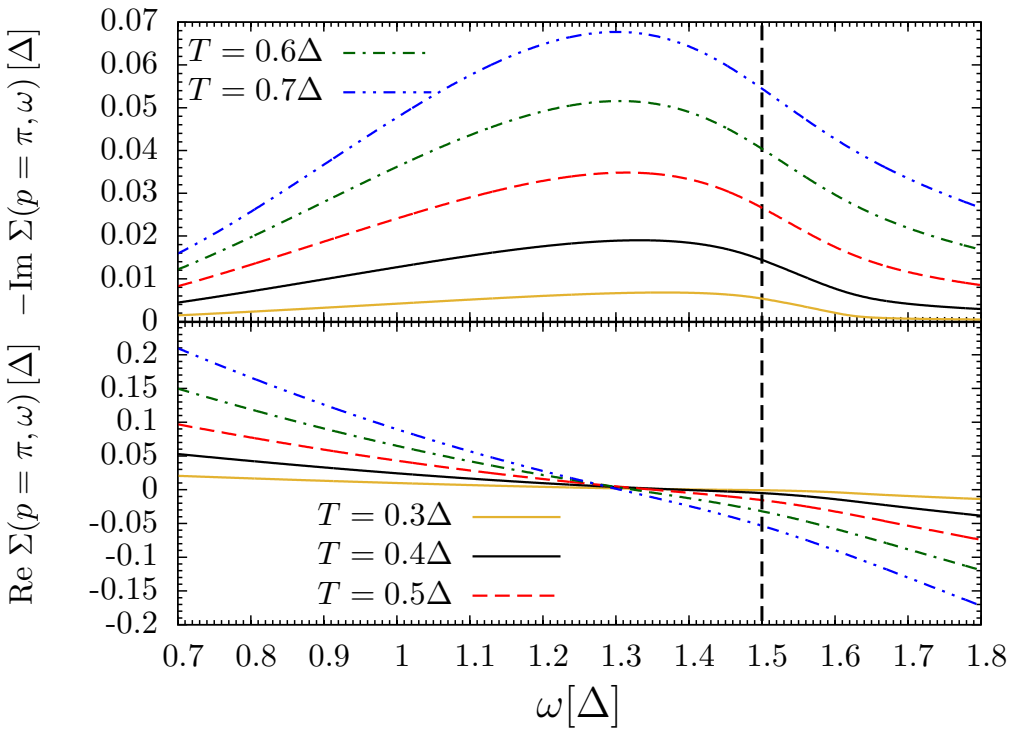

Figure 3.12: Real and imaginary part of the self-energy $\Sigma(p, \omega)$ at various temperatures for the maximum mode $p = \pi$ for $W = 0.5\Delta$. The vertical line indicates the energy of the $p = \pi$ mode at zero temperature.

towards higher energies due to the positive slope of the imaginary part of the self-energy, the maximum mode shows a tail towards lower energies, induced by the negative slope. The real part of the self-energy is dominated by the term $\propto \omega$ in Eq. (2.40a), for very high and very low energies. For $p = 0$ the real part is positive, indicating a shift of the peak position towards higher energies, while for $p = \pi$ the real part is negative, leading to a shift towards lower energies. With increasing temperatures the effect is amplified due to the increased scattering from thermal excitations.

3.4.4 Finite temperature peak broadening

At zero temperature the single-particle spectral function $A(p, \omega)$ is a δ-function in frequency, signaling stable quasi-particles and providing the dominant contributions to the DSF. Our approach includes this basic property, because the expression for the self-energy $\Sigma(p, \omega)$ in Eqs. (2.40a) and (2.40b) vanishes for $T \to 0$. Only because our numerical implementation to calculate $A(p, \omega)$ is restricted to a finite frequency and momentum resolution, we require that the temperature is not too low. Otherwise, we are not able to resolve the spectral function. Especially the self-consistent solutions require a finite broadening as initial input. This inital broadening does not matter at all once the computation is iterated for self-consistency and convergence is indeed reached. In our case, using up to 8 GB of memory to resolve the spectral function, we require that $T > 0.15\Delta$.

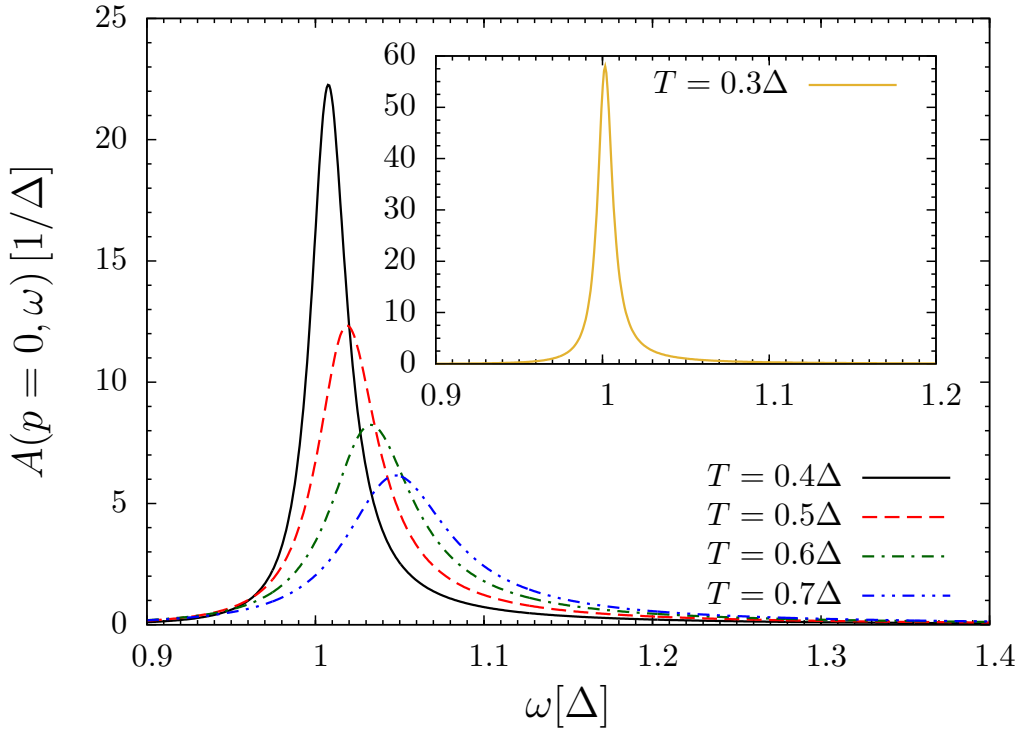

Figure 3.13: Spectral function $A(p,\omega)$ at various temperatures for the gap mode $p = 0$ for $W = 0.5\Delta$.

First, we consider the temperature dependence of the gap mode at momentum $p = 0$ for the narrow band case $W = 0.5\Delta$ calculated self-consistently in Fig. 3.13. For low temperatures the response is primarily of Lorentzian shape and centered at the zero temperature response $\omega = \Delta$. This changes distinctively at higher temperatures. Due to increased scattering with thermal excitations the height of the spectral function decreases. The decrease scales with $\exp(-\beta\Delta)$. The maximum of the response shifts towards higher energies and the peak broadens asymmetrically towards higher energies.

The degree of asymmetry is clearly visible in Fig. 3.14 where we compare the spectral function to a Lorentzian fit. While a pure Lorentzian shape provides evidence for incoherent scattering [29], i.e., an exponential decay in the time domain, asymmetric deviations imply non-trivial scattering. This observation agrees with recent theoretical as well as experimental studies [24, 25, 33, 34, 36–38, 40, 83, 84]. Second, we consider the temperature dependence of the maximum mode at momentum $p = \pi$ for the narrow band case $W = 0.5\Delta$ calculated self-consistently. This quantity is depicted in Fig. 3.15. Similar to the gap mode, the spectral function of the maximum mode has a Lorentzian shape and it is centered at the zero temperature position $\omega = \Delta + W$ for low temperatures. The peak broadens with rising temperature and becomes asymmetric. In contrast to the gap mode, the peak position of the maximum mode shifts towards lower energies. Concomitantly, the asymmetric line shape accumulates weight at lower energies.

An overview plot of the self-consistent spectral function $A(p,\omega)$ at fixed temperature $T = 0.8\Delta$ is given in Fig. 3.16. One clearly sees how the asymmetry slowly changes from the gap mode to the maximum mode in dependence of total momentum p.

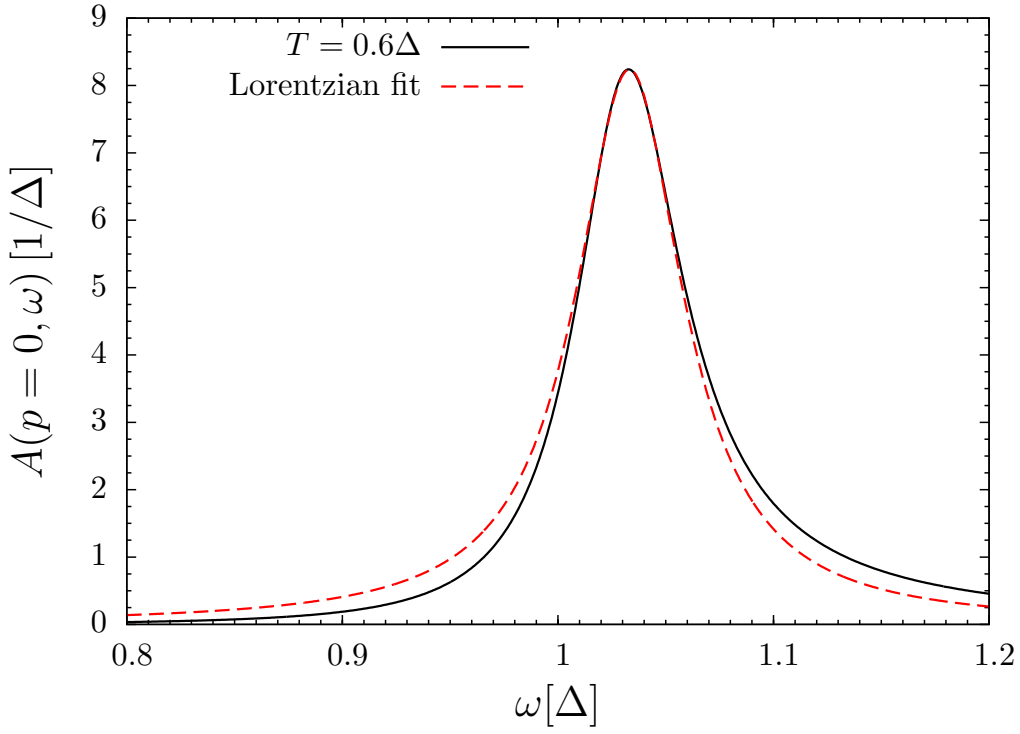

Figure 3.14: Comparison between Lorentzian line shape and asymmetric spectral function at $p = 0$ for $W = 0.5\Delta$.

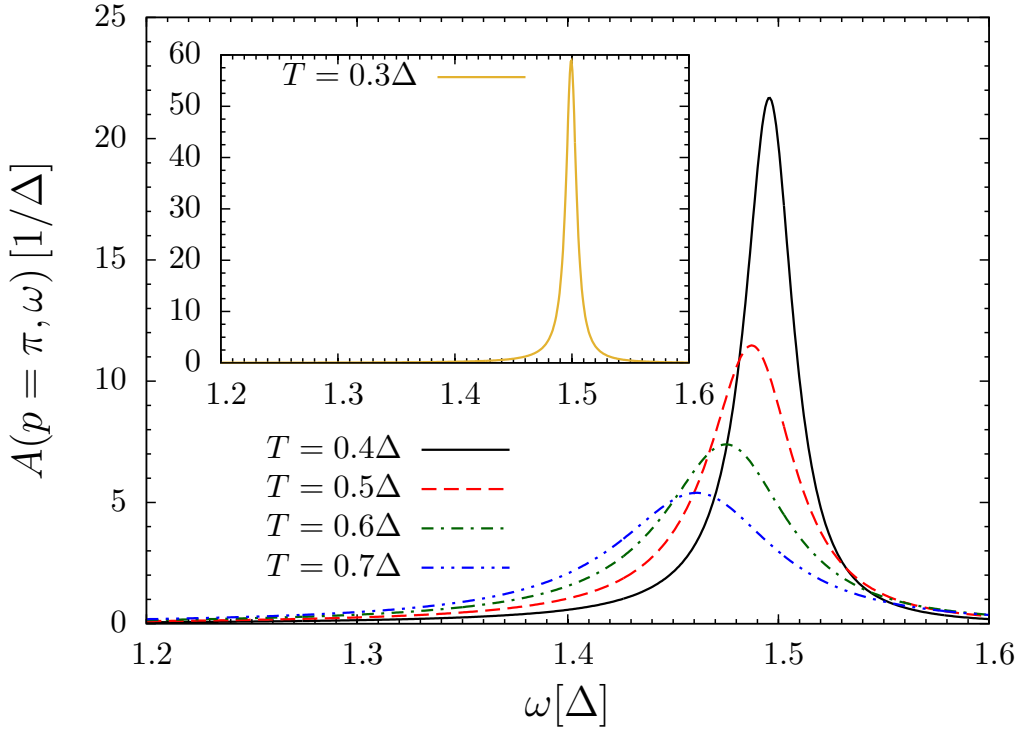

Figure 3.15: Spectral function $A(p, \omega)$ at various temperatures for the maximum mode $p = \pi$ for $W = 0.5\Delta$.

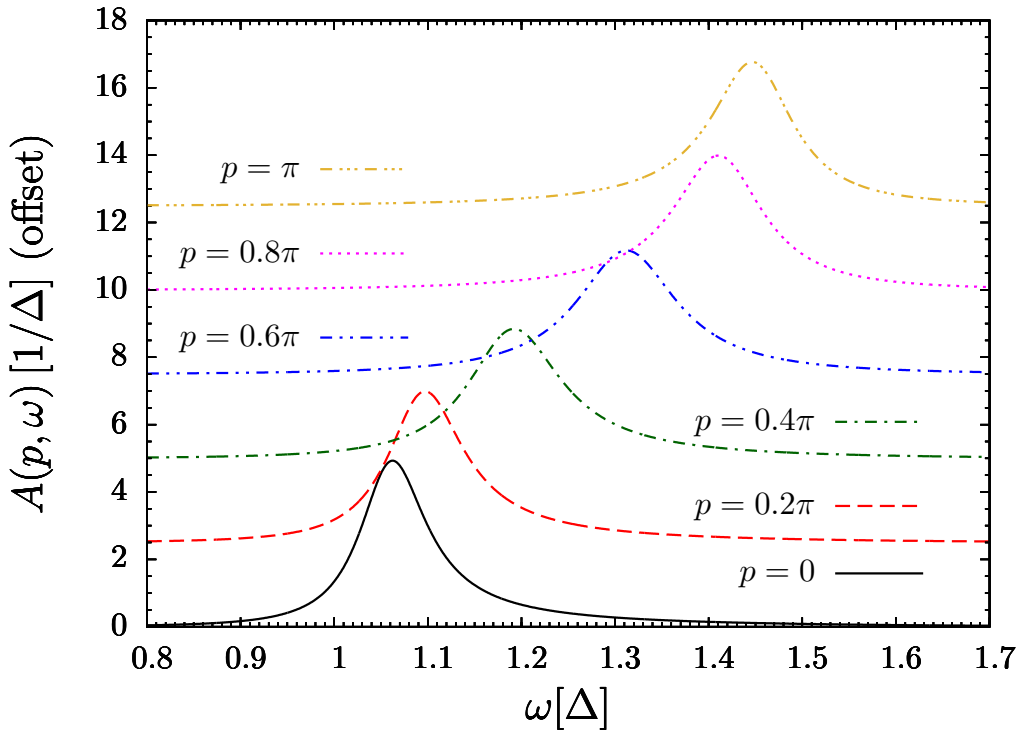

Figure 3.16: Spectral function for various momenta at fixed temperature $T = 0.8\Delta$ for $W = 0.5\Delta$. Note the offset of the y-axis.

Close to the center of the dispersion, the response remains symmetric and does not change its position with respect to the $T = 0$ response.

3.4.5 Band narrowing

The asymmetry and the shift of positions observed in the previous subsection indicates, that the total band-width of the system decreases upon rising temperature. We examine this feature in more detail in Figs. 3.17 and 3.18 for the narrow and the wide band case, respectively. The position of the maximum in the response is plotted as function of the total momentum p for various temperatures $T < \Delta$. While for low temperatures the maximum is located at the dispersion $\omega(p)$, the band is narrowing upon increasing temperature. This effect can be explained by the increased number of sites which are populated by thermal excitations, blocking the propagation of an inserted particle. Consequently, the energy gap is increased and the band-width is decreased. In the literature this is often called the temperature dependence of the gap [41] and of the dispersion, although the physical parameters Δ and W of the model do not change with temperature in the strict sense. In contrast to the narrow band case $W = 0.5\Delta$, the wide band case $W = 4\Delta$ indicates that the shift is significantly stronger for the gap mode than for the maximum mode.

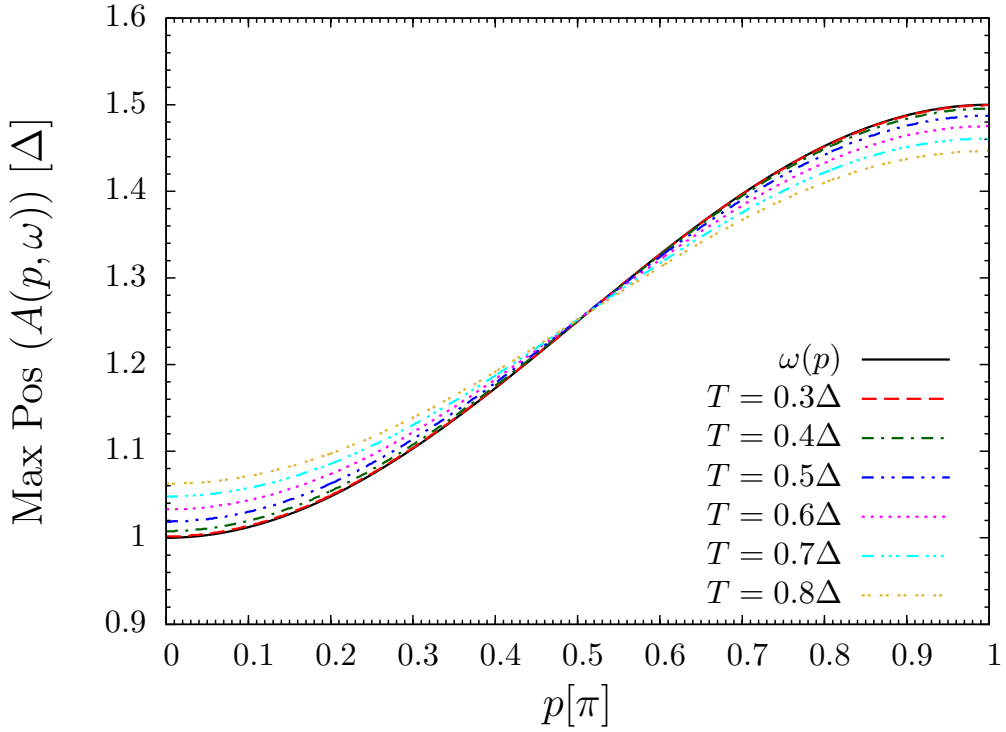

Figure 3.17: Dispersion determined from the position of the maximum of the spectral function for $W = 0.5\Delta$ for various temperatures.

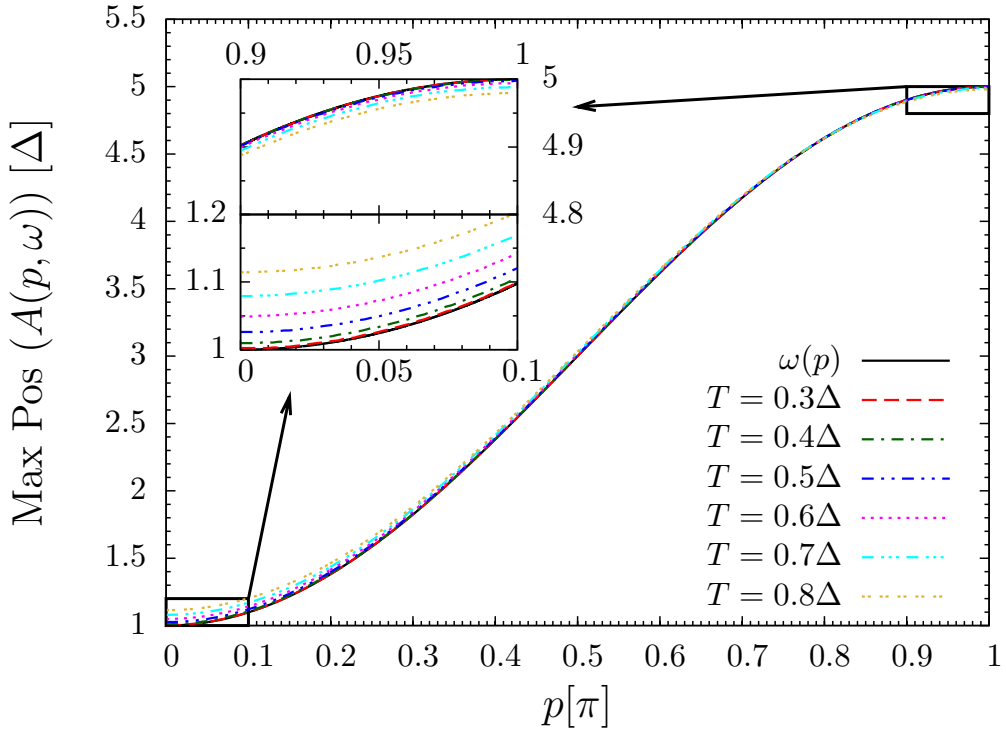

Figure 3.18: Dispersion determined from the position of the maximum of the spectral function for $W = 4\Delta$ for various temperatures. The inset shows a more detailed plot for the gap mode and for the maximum mode.

3.5 Conclusion

In this chapter, we benchmarked the diagrammatic Brückner approach to particle-conserving models and found it to be capable of dealing with thermal fluctuations in leading order in $\exp(-\beta\Delta)$.
For the benchmark, we studied the spectral properties of an exactly solvable gapped one-dimensional hard-core boson model with nearest neighbor hopping and no other interaction but the hard-core repulsion. We used diagrammatic perturbation theory to calculate the single-particle self-energy.
Our results show how the single-particle δ-peak in the spectral function broadens with increasing temperature and how band-width and momentum influence the spectral function. We used the mapping to interaction-free Jordan-Wigner fermions to obtain results which are numerically exact except for finite size and time effects. By this data we have gauged our diagrammatic approach and evaluated its limits. For low temperature very good agreement is reached. Both methods show that the shift of the peak position is a second order effect $\propto \exp(-2\beta\Delta)$ for the cosine band. In contrast, the width of the peak is a first order effect $\propto \exp(-\beta\Delta)$. Thus, it is captured very well by the diagrammatic approach for low enough temperatures.
With the help of the spectral function we also calculated the thermal occupation, ,i.e. the density of thermally excited bosons. The corresponding results of the self-consistent diagrammatic approach are in excellent agreement with the exact analytic expression available from the fermionic description, even for temperatures far above the gap Δ.
We found clear evidence that (i) the line shapes become asymmetric and that (ii) the band width of the overall dispersion narrows upon increasing temperature.
We conclude that the diagrammatic expansion is an efficient and universal method to calculate line shapes at not too high temperatures. The starting point are particle-conserving models with hard-core bosonic excitations.

4 Extensions of the Brückner approach

In this chapter the Brückner approach is extended to include Hamiltonians that are not particle conserving and obtain additional interactions. We will show, how the diagrammatic perturbation theory can be combined with effective models derived by continuous unitary transformations in section 4.1 and how additional interactions in the effective model can be included using a mean-field approximation in section 4.2. Next we will show how temperature dependent vertex corrections can be calculated in the context of diagrammatic perturbation theory and how this affects static quantities, such as the k-dependent static structure factor in section 4.3. In order to demonstrate the combination of the Brückner approach with effective models derived by CUTs, we will calculate the temperature dependent structure factor of the transverse field Ising model in section 4.4. Finally, in section 4.5, it is shown, how the Brückner approach can deal with elementary excitations that have internal degrees of freedom, such as the flavor of triplons in dimerized system.

All calculations will be given for the one dimensional case, but they can be extended to higher dimensions easily.

The introduction to the deepCUT approach and the effective model for the transverse field Ising model used in section 4.3 are results of my Master thesis and have been published in Physical Review B as a regular article [59] [1]. Parts of the section 4.5 have been published in Physical Review B as a regular article [85] [2]. The manuscript and the interpretation of the data contain contributions from Götz S. Uhrig and myself.

4.1 Effective models

The basis for the application of the Brückner approach is a model, that conserves the number of quasi-particle excitations in the system. A prerequisite for this property is an effective Hamiltonian, that has no operators in second quantization, that change the

[1] © 2013 American Physical Society.
[2] © 2015 American Physical Society.

total number of particles. The general form of such a Hamiltonian is given by

$$H_{\text{eff}} = E_0 + \sum_{i,d} \left(w_d b_i^\dagger b_{i+d} + \text{h.c.} \right) + \sum_{i,d_1,d_2,d_3} V_{d_1,d_2,d_3} b_i^\dagger b_{i+d_1}^\dagger b_{i+d_2} b_{i+d_3} + \ldots, \tag{4.1}$$

where the dots stand for possible higher particle-number interactions. Note, that the operator Q,

$$Q = \sum_i b_i^\dagger b_i \tag{4.2}$$

that counts the total number of excitations in the system is a conserved quantity,

$$[H_{\text{eff}}, Q] = 0. \tag{4.3}$$

One way to obtain such a Hamiltonian in second quantization are continuous unitary transformations (CUTs). In the following we will introduce the concept of CUT, followed by an explanation, on how to combine it with the diagrammatic Brückner approach.

4.1.1 Continuous unitary transformations

In general a Hamiltonian can be diagonalized by the use of an appropriate unitary transformation

$$H_{\text{diag}} = \underline{\underline{U}} H \underline{\underline{U}}^\dagger, \tag{4.4}$$

where $\underline{\underline{U}}$ is a unitary transformation and H is the Hamiltonian of the system.
However the complete diagonalization of a Hamiltonian is often a very hard problem, since it includes an infinite number of degrees of freedom in the thermodynamic limit. Hence one often tries to obtain only a block-diagonal structure of the Hamiltonian, so that the non-diagonal elements in the same block remain as the core problem.
A CUT is a renormalization scheme that is based on unitary transformations that are adjusted in a continuous fashion to yield such a desired block-diagonal Hamiltonian. By using a continuous transformation, the approach offers a systematic way to map the Hamiltonian onto a diagonal representation unitarily. The concept of CUTs was first introduced by Wegner [86] and independently by Głazek and Wilson [87, 88]. It was extended by Mielke [89], and independently by Knetter and Uhrig [90], to aim at the quasi-particle picture directly.
In this section we will focus mainly on those CUTs that yield a block-diagonal Hamiltonian in terms of quasi-particle blocks. Even in this case a variety of different manifestations of CUT exist. We refer the reader to Refs. [62–64, 86, 90, 91] for a more detailed introduction to this topic.
The key idea of CUT is to introduce a family of unitary transformations depending differentiable on a parameter $l \in \mathbb{R}^+$, which makes the Hamiltonian dependent on l

via

$$H(l) = \underline{\underline{U}}(l) H \underline{\underline{U}}^{\dagger}(l). \tag{4.5}$$

For $l \to \infty$ the effective Hamiltonian is obtained,

$$H_{\text{eff}} = \lim_{l \to \infty} H(l). \tag{4.6}$$

If the transformation is unitary, it is easy to show that the l-dependent Hamiltonian follows a first order differential equation, also called the flow equation

$$\partial_l H(l) = [\eta(l), H(l)] \tag{4.7}$$

with an anti-hermitian generator $\eta(l)$, which generates $U(l)$.
Observables O also need to be transformed to effective observables by the same unitary transformation. This results in the flow equation for observables

$$\partial_l O(l) = [\eta(l), O(l)] \tag{4.8}$$

which yields the effective observable O_{eff} for $l \to \infty$.
Naturally, the generator must depend on the Hamiltonian $H(l)$ to adjust the flow during the transformation (otherwise it could be trivially mapped to a static unitary transformation). The specific choice for η depends on the system and represents an active field of research.
In this thesis we will use the particle conserving (pc) generator. Using the eigenbasis of Q, the pc generator in matrix representation is given by

$$\eta_{\text{pc},ij}(l) = \text{sgn}(q_i - q_j) h_{ij}(l), \tag{4.9}$$

where q_i denotes the eigenvalues of the Operator Q. An equivalent description of the pc generator can be given by decomposing the Hamiltonian into parts that create, $H^+(l)$, conserve, $H^0(l)$, and annihilate, $H^-(l)$, quasi-particles,

$$H(l) = H^+(l) + H^0(l) + H^-(l). \tag{4.10}$$

Thus the quasi-particle conserving generator is simply given by

$$\eta_{\text{pc}} = H^+(l) - H^-(l). \tag{4.11}$$

In finite-dimensional systems, where a state of minimal energy exists, the convergence of the generator is proven [89,90]. Note, that the pc generator preserves the band diagonal structure defined by the operator Q
Upon commuting H with η, new types of terms, that were originally not part of the Hamiltonian, will arise. If the Hilbert space of the Hamiltonian has a finite dimension,

the operator space, acting on this Hilbert space, does so as well. In this case the self-consistent commutation in Eq. (4.7) will result in a closed set of differential equations. For problems with an infinite dimensional Hilbert space, e.g. systems in the thermodynamic limit, the situation changes. Here an infinite number of operators can appear, connecting several sites over large distances. In a numerical calculation we cannot treat an infinite number of operators, hence the operator basis has to be truncated to the physically most relevant operators.
A variety of truncation schemes are established in literature. In this thesis we use directly evaluated enhanced perturbative CUT (deepCUT) introduced in Ref. [63] to obtain an effective model. The idea of deepCUT is to truncate operators and contributions to the flow equation according to their effects in powers of a small expansion parameter x. Roughly speaking, the order n in x is the truncation criterion. More precisely, a certain contribution to the flow equation is kept if it affects the targeted quantities (e.g.: ground state energy, one-particle dispersion and two-particle interaction) in order $m \leq n$ in x. We refer the reader to Ref. [63] for details on the implementation of deepCUT.
Thus we write our initial Hamiltonian in the form

$$H = H_0 + xV \tag{4.12}$$

where H_0 describes the unperturbed Hamiltonian and V represents a perturbation. We expand the operators in the basis $\{A_i\}$, which is chosen such that the effective Hamiltonian can be computed exactly up to order n in the parameter x. Then the flowing Hamiltonian can be denoted as

$$H(l) = \sum_i h_i(l) A_i \tag{4.13}$$

where the prefactors $h_i(l)$ depend on the flow parameter l. For the generator we choose the same operator basis with the prefactors from the Hamiltonian

$$\eta(l) = \sum_i \eta_i(l) A_i = \sum_i h_i(l) \eta\left[A_i\right] \tag{4.14}$$

where $\eta\left[\cdot\right]$ is a superoperator applying the generator scheme. For the pc generator, $\eta\left[A_i\right] = A_i$ holds, if A_i creates more quasiparticles than it annihilates, $\eta\left[A_i\right] = -A_i$ holds, if A_i annihilates more quasiparticles than it creates, otherwise $\eta\left[A_i\right] = 0$, cf. Eq. (4.11).
With these definitions, we obtain the flow equations for the prefactors in the Hamiltonian

$$\partial_l h_i(l) = \sum_{j,k} D_{ijk} h_j(l) h_k(l). \tag{4.15}$$

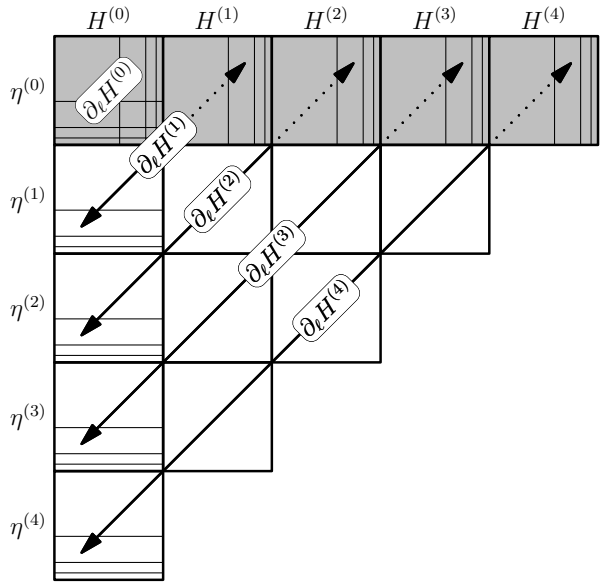

Figure 4.1: Illustration of the algorithm used to determine all contributions for a given maximum order, here 4, from Ref. [63]. The boxes represent the calculation of the commutator between the different orders of the generator $\eta^{(m)}$ and the Hamiltonian $H^{(n)}$ to obtain the contributions to the flow equation. The calculation for every order o is based on the previous orders and is achieved by calculating every commutator with $n + m = o$.

We call the prefactors $D_{ijk} \in \mathbb{C}$ the contributions to the flow equation. They are computed in a perturbative calculation up to order n by calculating the commutator in Eq. (4.7) and expanding the results in the chosen operator basis. Note, that the numerically evaluated flow equation also comprises powers in x beyond the order n [63].
An effective algorithm to determine all contributions D_{ijk} to the flow equation for a given order n is sketched in Fig. 4.1. Once the contributions are known, integrating the resulting differential equation is a standard numerical task. For $l \to \infty$ all prefactors $h_i(l)$ of operators A_i that violate particle number conservation vanish, whereas the remaining prefactors determine the ground state energy and the prefactors in the effective Hamiltonian in Eq. (4.1).

4.2 Mean-field approximation for additional interactions

Once we have obtained the effective model using CUT, we can use it as an input for the diagrammatic Brückner approach. The ground state energy E_0 determines the absolute energy scale of the system, but it is not directly measurable in experiment. The dispersion of the system is given by the Fourier transform of the hopping matrix elements w_d

$$\omega(k) = w_0 + 2 \sum_d w_d \cos(kd), \tag{4.16}$$

which enters into the single particle Green function

$$G_0(k, i\omega_k) = \frac{1}{i\omega_k - \omega(k)}. \tag{4.17}$$

In this way, quantum fluctuations, which lead to dispersive single particle bands are taken into account within the Brückner approach. In first order of $\exp(-\beta\Delta)$ also the additional two-particle interaction in Eq. (4.1) contributes to the single particle self-energy. Taking the full interaction into account in the Bethe-Salpeter equation is a complicated problem. We will tackle this issue later in chapter 7. In this section we will use a self-consistent mean-field approximation to include the effects of the additional interactions.
In its most general form, the additional interaction can be written as

$$H_V = \sum_{i,d_1,d_2,d_3} V_{d_1,d_2,d_3} b_i^\dagger b_{i+d_1}^\dagger b_{i+d_2} b_{i+d_3}. \tag{4.18}$$

Normal ordering this operator with respect to the thermal state gives

$$\begin{aligned} b_i^\dagger b_{i+d_1}^\dagger b_{i+d_2} b_{i+d_3} &=: b_i^\dagger b_{i+d_1}^\dagger b_{i+d_2} b_{i+d_3} : \\ &+ \langle b_i^\dagger b_{i+d_2}\rangle b_{i+d_1}^\dagger b_{i+d_3} + \langle b_i^\dagger b_{i+d_3}\rangle b_{i+d_1}^\dagger b_{i+d_2} \\ &+ \langle b_{i+d_1}^\dagger b_{i+d_2}\rangle b_i^\dagger b_{i+d_3} + \langle b_{i+d_1}^\dagger b_{i+d_3}\rangle b_i^\dagger b_{i+d_2} \\ &+ \text{ground state energy correction.} \end{aligned} \tag{4.19}$$

The ground state energy correction can be ignored, because it has no effect on the single particle properties. In the mean-field approximation the pure two-particle thermal fluctuations $: b_i^\dagger b_{i+d_1}^\dagger b_{i+d_2} b_{i+d_3} :$ are neglected, and only the single particle contributions are taken into account. The expectation values can be calculated in Fourier space

$$\langle b_j^\dagger b_{j+d}\rangle = \frac{1}{N}\sum_j \langle b_j^\dagger b_{j+d}\rangle = \frac{1}{N^2}\sum_{j,k,k'} \langle b_k^\dagger b_{k'}\rangle e^{ikj} e^{-ik'(j+d)} \tag{4.20a}$$

$$= \frac{1}{N}\sum_k \langle b_k^\dagger b_k\rangle e^{-ikd} =: h(d) \tag{4.20b}$$

For systems with an inversion symmetry in momentum space, i.e. $k \to -k$, the expectation value is purely real,

$$h(d) = \frac{1}{N}\sum_k \langle b_k^\dagger b_k\rangle \cos(kd). \tag{4.21}$$

Then we can rewrite the operators in the additional interaction

$$\begin{aligned} b_i^\dagger b_{i+d_1}^\dagger b_{i+d_2} b_{i+d_3} &\approx h(d_2) b_{i+d_1}^\dagger b_{i+d_3} + h(d_3) b_{i+d_1}^\dagger b_{i+d_2} \\ &+ h(d_2 - d_1) b_i^\dagger b_{i+d_3} + h(d_3 - d_1) b_i^\dagger b_{i+d_2} \end{aligned} \tag{4.22}$$

We Fourier transform the remaining operators into momentum space to obtain:

$$H_V \approx \sum_{k,d_1,d_2,d_3} \big(h(d_2)e^{ik(d_1-d_3)} + h(d_3)e^{ik(d_1-d_2)} + h(d_2-d_1)e^{-ikd_3} + h(d_3-d_1)e^{-ikd_2}\big)\, b_k^\dagger b_k \tag{4.23}$$

Assuming that the system has inversion symmetry and due to hermiticity we can take only the real part of the prefactors,

$$H_V \approx \sum_{k,d_1,d_2,d_3} V_{d_1,d_2,d_3} \left(h(d_2)\cos(k\,[d_1-d_3]) + h(d_3)\cos(k\,[d_1-d_2]) + h(d_2-d_1)\cos(kd_3) + h(d_3-d_1)\cos(kd_2)\right) b_k^\dagger b_k. \tag{4.24}$$

Now the additional interaction is purely bilinear and represents a correction to the dispersion at finite temperature,

$$\omega(k) \to \tilde{\omega}(k) = \omega(k) + \sum_{d_1,d_2,d_3} V_{d_1,d_2,d_3} \left(h(d_2)\cos(k\,[d_1-d_3]) + h(d_3)\cos(k\,[d_1-d_2]) + h(d_2-d_1)\cos(kd_3) + h(d_3-d_1)\cos(kd_2)\right). \tag{4.25}$$

As a result, the mean-field approximation only changes the real part of the self-energy and shifts the position of the peak. Since the imaginary part of the self-energy is frequency dependent, the approximation can also have a very small influence on the imaginary part and on the width of the peak. The expectation values can be calculated using the spectral function $A(k,\omega)$, see appendix C. Thus the mean-field approximation can be combined into the self-consistent calculation of the spectral function. Specifically, it is introduced in Eq. (2.41),

$$A(p,\omega) = \frac{-1}{\pi}\mathrm{Im}\, G(p,\omega) = \frac{1}{\pi}\frac{\mathrm{Im}\Sigma(\omega,p)}{\left(\omega - \tilde{\omega}(p) - \mathrm{Re}\Sigma(\omega,p)\right)^2 + \left(\mathrm{Im}\Sigma(\omega,p)\right)^2}. \tag{4.26}$$

Higher order interactions in (4.1), such as three-particle interactions, can be ignored, since they first show up in $\mathcal{O}\left(\exp(-2\beta\Delta)\right)$.

4.3 Vertex corrections

Besides fully dynamical quantities, such as the spectral function, also static properties can have a non-trivial dependence on temperature. In this section we want to concentrate on the temperature dependence of the static structure factor. The single particle static structure factor is given by the integral of the single particle dynamic structure factor

over frequency ω,

$$S^x(p) = \int_{-\infty}^{\infty} \mathrm{d}\omega S^x(p,\omega). \tag{4.27}$$

It represents the weight of the single particle mode, as function of momentum. For the simple nearest neighbor chain in chapter 3, the static structure factor was a constant as function of momentum, but clearly dependent on temperature as seen in Figs. 3.7 and 3.8.

To obtain the static structure factor at zero temperature, a renormalization method, such as a CUT, can be used. Within the framework of CUTs, observables, such as the magnetization, must be transformed to obtain effective observables valid in the effective model. For example the effective creation and annihilation operators can be determined by a CUT, see Eq. (4.8). Thus we replace,

$$b_j^\dagger \to b_{j,\mathrm{eff}}^\dagger = \sum_d W_d b_{j+d}^\dagger + \ldots, \tag{4.28}$$

where W_d denotes the strength of the effective creation operator at site $j+d$ and the dots imply higher particle number contributions. Due to quantum fluctuation the previously completely local operator $b_j^\dagger$ obtains a cloud of creation operators located at nearby sites, depending on the strength of the quantum fluctuations, c.f. Ref. [63]. The quantity of interest for the static structure factor is the Fourier transformed operator

$$b_q^\dagger = \frac{1}{\sqrt{N}} \sum_j e^{-iqj} b_j^\dagger \to b_{q,\mathrm{eff}}^\dagger = \frac{1}{\sqrt{N}} \sum_j e^{-iqj} b_{j,\mathrm{eff}}^\dagger \tag{4.29}$$

The terms consisting of single $b^\dagger$ operators are easy to transform

$$b_{q,\mathrm{eff}}^\dagger = \frac{1}{\sqrt{N}} \sum_j e^{-iqj} b_j^\dagger \left(W_0 + \sum_{d=1}^{\infty} 2W_d \cos(dq) + \ldots \right), \tag{4.30}$$

where we used inversion symmetry $W_d = W_{-d}$. At $T = 0$ only isolated creation operators contribute to the single particle static structure factor. However, at finite T also more complicated contributions must be taken into account.

Fortunately, if we are interested in single particle properties, only a certain kind of contributions matter in first order $\exp(-\beta\Delta)$,

$$b_{j,\mathrm{eff}}^\dagger = \sum_d W_d b_{j+d}^\dagger + \sum_{d_1,d_2,d_3} W_{d_1,d_2,d_3} b_{j+d_1}^\dagger b_{j+d_2}^\dagger b_{j+d_3} + \ldots. \tag{4.31}$$

Note, that the second term creates two particles and annihilates a single particle at the same time. We call this process a conditional excitation, because it can only occur at finite temperature, if the annihilated particle is a thermal fluctuation. The two created

particles count towards positive energies, whereas the annihilated particle frees energy from the system and thus counts towards negative energies, so that the total process contributes in the range of the single particle dispersion. For fixed total momentum p the process has two relative momenta as degrees of freedom, so that the total contribution forms a broad incoherent continuum. However, if one of the particles is far apart from the others, its dynamics is primarily that of a single particle, which results in a sharply peaked response in the spectral function. Due to momentum conservation, the position of the strong response coincides with the pure single particle spectral function. To obtain this important contribution to the spectral function, we apply a mean-field decoupling in the operators,

$$b^\dagger_{j+d_1} b^\dagger_{j+d_2} b_{j+d_3} \approx b^\dagger_{j+d_1} \left\langle b^\dagger_{j+d_2} b_{j+d_3} \right\rangle + b^\dagger_{j+d_2} \left\langle b^\dagger_{j+d_1} b_{j+d_3} \right\rangle . \tag{4.32}$$

So that the effective creation operator now reads

$$b^\dagger_{j,\mathrm{eff}} = \sum_d W_d b^\dagger_{j+d} + \sum_{d_1,d_2,d_3} W_{d_1,d_2,d_3} \left(b^\dagger_{j+d_1} \left\langle b^\dagger_{j+d_2} b_{j+d_3} \right\rangle + b^\dagger_{j+d_2} \left\langle b^\dagger_{j+d_1} b_{j+d_3} \right\rangle \right) + \dots . \tag{4.33}$$

We use the abbreviation $h(d)$ from Eq. (4.20) to lighten the notation. Calculating the new effective weight of the single particle creation at finite temperature yields

$$b^\dagger_{j,\mathrm{eff}} = \sum_d W_{d,\mathrm{eff}} b^\dagger_{j+d} \tag{4.34}$$

with

$$W_{d,\mathrm{eff}} = W_d + \sum_{d_2,d_3} W_{d,d_2,d_3} h(d_3 - d_2) + \sum_{d_1,d_3} W_{d_1,d,d_3} h(d_3 - d_1). \tag{4.35}$$

So that the effect of the conditional excitation is a renormalization of the creation and annihilation vertex.

4.4 Finite temperature dynamics in the transverse field Ising model

In order to examine the performance of the Brückner approach in combination with CUTs, we examine the transverse field Ising model (TFIM) in the strong field regime. The TFIM is a spin chain with Ising couplings in the x direction and a magnetic field

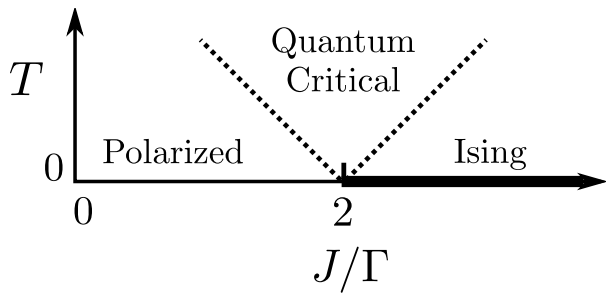

Figure 4.2: Phase diagram of the TFIM as function of the Ising coupling over the magnetic field strength J/Γ and temperature T.

in z direction. The Hamiltonian of the TFIM reads

$$H_{\mathrm{TFIM}} = \Gamma \sum_i S_i^z - J \sum_i S_i^x S_{i+1}^x, \tag{4.36a}$$

$$\Gamma > 0, \tag{4.36b}$$

where Γ is the magnetic field and J the strength of the local Ising coupling. Starting from the strong field limit, i.e. $J = 0$, the system exhibits a quantum phase transition upon increasing J from a polarized phase into a two-fold degenerate Ising phase at $J = 2\Gamma$. The phase diagram as function of Ising coupling J and temperature T is shown in Fig. 4.2. Note, that the Ising phase is only stable at exactly zero temperature, since even very small thermal fluctuations in the Ising phase will destroy the long range order. At finite temperature there exists a quantum critical region on top of the quantum phase transition. It is signalled by universal correlation functions that can be obtained from continuum field theory. In the strong field limit, the ground state of the system is adiabatically connected to the fully polarized state and the elementary excitations are spin flips. In the Ising phase, the ground state is a twofold degenerate ferromagnetic state, with domain wall excitations. For a detailed overview on the physics of the TFIM we refer the reader to Refs. [19, 60].

For the strong field limit, it was shown in Ref. [59] that the Hamiltonian of the TFIM can be mapped by CUTs onto an effective Hamiltonian

$$H_{\mathrm{TFIM,eff}} = t_0 T_0 + \sum_n t_n^{+-} \left(T_n^{+-} + \mathrm{h.c.} \right) \tag{4.37}$$

where the T_n operators are string operators given by

$$T_n^{\phi\epsilon} := \sum_j \sigma_j^\phi \left(\prod_{k=j+1}^{j+n-1} \sigma_k^z \right) \sigma_{j+n}^\epsilon = \sum_j \sigma_j^\phi \sigma_{j+1}^z \sigma_{j+2}^z \cdots \sigma_{j+n-1}^z \sigma_{j+n}^\epsilon, \tag{4.38a}$$

$$\{\phi, \epsilon\} \in \{+, -\} \quad , \quad n \in \mathbb{N}^+, \tag{4.38b}$$

and T_0 is given by

$$T_0 := \sum_j \sigma_j^z. \tag{4.39}$$

The real parameters t_0 and t_n^{+-} of the Hamiltonian are obtained by a CUT and depend merely on Γ and J. Since all operators T_n are particle conserving, the ground state $|g\rangle$ of the effective Hamiltonian is given by the fully polarized state

$$|g\rangle = |\cdots\downarrow_{j-1}\downarrow_j\downarrow_{j+1}\cdots\rangle\,. \tag{4.40}$$

We identify the S^+ and S^- operators with the particle creation and annihilation operators $b^\dagger$ and b respectively and we replace

$$\sigma_j^z = 2b_j^\dagger b_j - 1. \tag{4.41}$$

Hence we can interpret the ground state as the vacuum of all excitations $|0\rangle$. The single particle properties are determined from the string operators T_n, with all intermediate σ^z's replaced by -1. The first term including also two particle interactions can be found for $n = 2$,

$$\sigma_j^+\sigma_{j+1}^z\sigma_{j+2}^- = b_j^\dagger\left(2b_{j+1}^\dagger b_{j+1} - 1\right)b_{j+2}. \tag{4.42}$$

As discussed above, we apply a mean-field decoupling on the two-particle interaction

$$\begin{aligned} b_j^\dagger b_{j+1}^\dagger b_{j+1} b_{j+2} \approx\ & \langle b_j^\dagger b_{j+1}\rangle b_{j+1}^\dagger b_{j+2} + \langle b_j^\dagger b_{j+2}\rangle b_{j+1}^\dagger b_{j+1} \\ & + \langle b_{j+1}^\dagger b_{j+1}\rangle b_j^\dagger b_{j+2} + \langle b_{j+1}^\dagger b_{j+2}\rangle b_j^\dagger b_{j+1} \\ & + \text{ground state energy correction} \end{aligned} \tag{4.43}$$

This can be trivially generalized for all $n > 2$, see appendix D. The final expression for the correction to the dispersion reads

$$\begin{aligned} \tilde{\omega}(q) = \omega(q) + \sum_{d_2=2}^{\infty} 4t_{d_2}^{+-}(-1)^{d_2} \sum_{d_1=1}^{d_2-1} \big(&h(d_1)\cos([d_2-d_1]q) + h(d_2) \\ &+ h(0)\cos(d_2 q) + h(d_2-d_1)\cos(d_1 q)\big)\,. \end{aligned} \tag{4.44}$$

In the following we want to examine the temperature dependence of the static structure factor. In the original basis the dynamic structure factor reads,

$$S^x(\omega, Q) = \frac{1}{N}\sum_{l,l'} e^{-iQ(l-l')}\langle S_l^x S_{l'}^x\rangle, \tag{4.45}$$

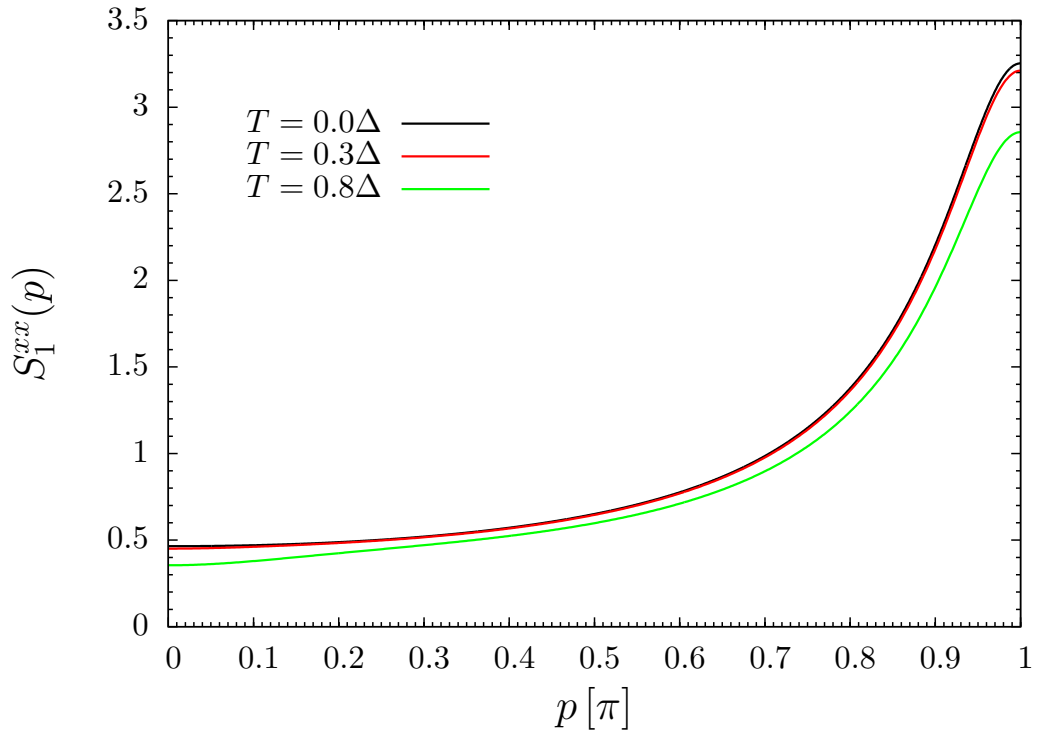

Figure 4.3: Static structure factor of the TFIM as function of momentum p. The parameters are given by $J = 1.5\Gamma$ for different temperatures.

where all spin operators have to be replaced by the correspond effective operators in the diagonal basis. Since the single S^+ operator is not part of the string operator basis, its transformation under the CUT is much more complicated [59]. We refer the reader to appendix E for a detailed calculation on the vertex corrections at finite temperature.
Using the effective model and observables from the CUT and the Brückner approach to obtain the spectral function at finite temperature, we can compute the temperature dependence of the static structure factor. The results for $J = 1.5\Gamma$ are shown in Fig. 4.3 for different temperatures measured in units of the single particle gap Δ. The static structure factor has a strong peak at $p = \pi$, indicating that the gap mode has the most important contribution to the dynamic structure factor. Note however, that the total weight, i.e. the integral of the structure factor over frequency and momentum, of the single particle contribution vanishes for $J \to 2\Gamma$, where the quantum phase transition between the ordered and disordered phase is located. As temperature is increased, the momentum dependence roughly stays the same, but the total weight is decreased further. This shows, that the total single particle spectral weight vanishes faster at finite temperature due to thermal fluctuations. This observation is in accordance with the quantum critical region close to the phase transition at $J = 2\Gamma$, where the dynamics is dominated by universal correlations.

4.5 Multi-flavor systems

In this section we extend the Brückner approach to systems with multiple flavors, i.e., the hard-core bosons have internal degrees of freedom. But each site can still only be occupied by a single boson. This situation is relevant wherever the local site is represented by a more complex quantum system with a Hilbert space dimension larger than two. Furthermore, we study to which extent the approach works as well as it does in the single flavor case.
A generic example for multi-flavor problems are systems built from coupled dimers, each consisting of two spins $S = 1/2$. In these systems the elementary excitations are mobile $S = 1$ triplets, called triplons to distinguish them from magnons in ordered magnets [92]. For full SU(2) symmetry the triplons are threefold degenerate, i.e., they are hardcore bosons with three flavors.

4.5.1 Extension of the Brückner approach to multi-flavor hard-core bosons

In case of multiple flavors the Hamiltonian of conserved hardcore bosons reads

$$H_0 = E_0 + \sum_{i,d,\alpha} \left(w_d^\alpha b_{i,\alpha}^\dagger b_{i+d,\alpha} + \text{h.c.} \right) + \sum_{\substack{i,\, d_1,\, d_2,\, d_3 \\ \alpha,\, \phi,\, \gamma,\, \xi}} V_{d_1,d_2,d_3}^{\alpha,\phi,\gamma,\xi} b_{i,\alpha}^\dagger b_{i+d_1,\phi}^\dagger b_{i+d_2,\gamma} b_{i+d_3,\xi} + \ldots , \tag{4.46}$$

where the dots stand for possible higher particle-number interactions. Here E_0 denotes the ground state energy, $\{i, d, d_1, d_2, d_3\}$ denote site indices which do not need to be restricted to one dimension, $\{\alpha, \phi, \gamma, \xi\}$ denote flavor indices, w_d^α are hopping matrix elements, $V_{d_1,d_2,d_3}^{\alpha,\phi,\gamma,\xi}$ are interaction vertices and $b_{i,\alpha}^\dagger, b_{i,\alpha}$ denote hardcore bosonic creation and annihilation operators. The hopping matrix elements must fulfill the hardcore constraint, i.e., $d \neq 0, d_1 \neq 0, d_2 \neq d_3$.
As before, the Hamiltonian does not include terms that change the number of particles. Hence Eq. (4.46) is already an effective model, derived for example from a CUT. Note, that the bilinear part is diagonal in the flavor index. If this is not the case for an effective model, a diagonalization on the level of the flavor indices is required, e.g. by introducing a new set of creation and annihilation operators, that consist of the old creation and annihilation operators respectively.
The hardcore operators in second quantization fulfill the algebra,

$$\left[b_{i,\alpha}, b_{j,\phi}^\dagger \right] = \delta_{ij} \left(\delta_{\alpha\phi} \left(1 - \sum_\gamma b_{i,\gamma}^\dagger b_{i,\gamma} \right) - b_{i,\phi}^\dagger b_{i,\alpha} \right) . \tag{4.47}$$

Transforming the hardcore commutator into Fourier space yields

$$\left[b_{k,\alpha}, b^\dagger_{k',\phi}\right] = \frac{1}{N}\sum_q \left(\delta_{\alpha,\phi}\left(1 - \sum_\gamma b^\dagger_{k'+q,\gamma} b_{k+q,\gamma}\right) - b^\dagger_{k'+q,\phi} b_{k+q,\alpha}\right). \tag{4.48}$$

The single-particle spectral function now depends on an additional index α, which describes the propagation of a single particle with flavor α

$$A^\alpha(p,\omega) = \frac{-1}{\pi} \lim_{i\omega_\nu \to \omega + i0^+} \mathrm{Im} \int_0^\beta \mathrm{d}\tau e^{i\omega_\nu \tau} \frac{1}{\sqrt{N}} \sum_j e^{-ipj} G^\alpha(j,\tau),$$

where $G^\alpha(j,\tau)$ is the single-particle Green function

$$G^\alpha(j,\tau) = -\left\langle T\left\{b^\dagger_{j,\alpha}(-i\tau) b_{0,\alpha}(0)\right\}\right\rangle. \tag{4.49}$$

Sum rules are also affected by multiple flavors. The sum rule for the spectral function now reads,

$$\int_{-\infty}^{\infty} A^\alpha(p,\omega)\mathrm{d}\omega = 1 - (1 + N_\mathrm{f}) n(T), \tag{4.50}$$

where N_f denotes the number of different flavors, e.g., $N_\mathrm{f} = 3$ in the triplon case.
The thermal occupation $n(T) = \frac{1}{N}\sum_q \langle b^\dagger_{q,\alpha} b_{q,\alpha}\rangle$ is a function of temperature and independent of α if the different flavors are degenerate. At zero temperature, the thermal occupation vanishes and the standard boson sum rule is recovered. At infinite temperature, each state has the same probability to be occupied, hence $n(T) = 1/(1+N_\mathrm{f})$ holds. As a consequence, the integration of the spectral function over frequency vanishes. In between, the thermal occupation is a non-trivial quantity.
As in the single flavor case we replace the initial Hamiltonian H_0 in Eq. (4.46) by

$$H = H_0 + H_U \tag{4.51a}$$

$$H_U = \lim_{U\to\infty} \frac{U}{2} \sum_i \sum_{\alpha,\phi} b^\dagger_{i,\alpha} b^\dagger_{i,\phi} b_{i,\phi} b_{i,\alpha}, \tag{4.51b}$$

where U is the strength of the auxiliary local repulsion. The main difference to the Hamiltonian in Eq. (2.12) is that different flavors repel each other on the same site as well.
On the diagrammatic level, the main diagrams that change due to multiple flavors, are the Hartree-like diagrams. Since the Fock-like diagrams require, that all propagators are of the same flavor. In the Hartree-like diagrams, the propagators forming the loop can have an arbitrary flavor, which must be summed over.
On the level of the scattering amplitude however, two indices must be taken into ac-

count,

$$\Gamma^{\alpha,\phi}(P) = \frac{\frac{U}{N\beta}}{1 + \frac{U}{N\beta}\sum_{Q} G^{\alpha}(P+Q)G^{\phi}(-Q)}. \tag{4.52}$$

The same applies to the spectral functions $\rho_p(x)$ and $\bar{\rho}_p(x)$ introduced previously. Evaluating the self-energy diagrams leads to

$$\Sigma^{\alpha}(P) = \frac{1}{N}\sum_{\phi}\sum_{K}(1+\delta_{\alpha,\phi})G^{\phi}(K)\Gamma^{\alpha,\phi}(P+K), \tag{4.53}$$

Note, that in the expression $(1+\delta_{\alpha,\phi})$, the first term comes from the Hartree-like diagram whereas the term proportional to $\delta_{\alpha,\phi}$ stems from the Fock-like diagram. If the flavors are degenerate, i.e., the propagator $G^{\alpha}(P) = G^{\phi}(P) = G(P)$ does not depend on the index α, one can simply replace the sum over the flavor index ϕ in (4.53) by a factor

$$\Sigma^{\alpha}(P) = \frac{1+N_{\mathrm{f}}}{N}\sum_{K} G^{\alpha}(K)\Gamma^{\alpha,\alpha}(P+K). \tag{4.54}$$

We conclude, that in case of degenerate multi-flavors the only correction to the self-energy is given by the factor $1 + N_{\mathrm{f}}$, increasing the decay rate in comparison to the single flavor case.

4.5.2 Multi-flavor nearest neighbor hard-core chain

In order to benchmark the results of the multi-flavor Brückner approach we use a linear chain of bosons with nearest neighbor hopping without any additional interactions again.

$$H = \sum_{i=1,\alpha}^{N}\left(\Delta + \frac{W}{2}\right) b_{i,\alpha}^{\dagger} b_{i,\alpha} - \sum_{i=1,\alpha}^{N-1}\frac{W}{4}\left(b_{i,\alpha}^{\dagger} b_{i+1,\alpha} + \mathrm{h.c.}\right). \tag{4.55}$$

Note that this model is the extension of the benchmark model in the single flavor case in Eq. (3.1) to multiple flavors. The energy gap is given by $\Delta > 0$ while $W > 0$ is the band width of the dispersion

$$\omega(k) = \Delta + \frac{W}{2}\left[1 - \cos(k)\right]. \tag{4.56}$$

We assume open boundary conditions in the following. The momentum is given by k and the minimum Δ of the dispersion is found at $k = 0$. The ground state of the system is given by the vacuum state.
Since we only allow nearest neighbor hopping, the bosons cannot skip over each other. This implies that a given sequence of the flavors along the chain is conserved in the dynamics induced by H in (4.55). Thus the flavor degree of freedom and the hopping

dynamics can be considered to be completely decoupled for a fixed number of bosons. The flavor degree adds a certain degree of entropy for a given number B of bosons. The hopping of the hardcore bosons acts as if all bosons have the same color. Hence we neglect the flavor index for now and focus on the dynamics of the bosons.
To calculate the thermodynamics of the flavorless hardcore bosons we apply a Jordan-Wigner transformation

$$\begin{aligned} c_j &= \exp(\pi i \sum_{i<j} b_i^\dagger b_i) b_j & c_j^\dagger &= \exp(-\pi i \sum_{i<j} b_i^\dagger b_i) b_j^\dagger \\ b_j &= \exp(-\pi i \sum_{i<j} c_i^\dagger c_i) c_j & b_j^\dagger &= \exp(\pi i \sum_{i<j} c_i^\dagger c_i) c_j^\dagger \end{aligned} \tag{4.57}$$

so that we obtain a fermionic chain model. Since only nearest neighbor hopping is allowed the Hamiltonian remains bilinear if expressed in fermions. The grand canonical partition function of these fermions is simple and given by

$$Z_g(\beta, \mu_0) = \mathrm{Tr}\left[\exp\left(-\beta H_0 + \beta\mu_0 \hat{n}\right)\right] \tag{4.58}$$

where $\hat{n} = \sum_j \hat{n}_j$ counts the number of fermions and $\langle \hat{n} \rangle = B$ is the expectation value for the number of thermally excited fermions in the chain. This is the total number of thermally excited bosons irrespective of their flavor. The chemical potential is given by μ_0. The Hamiltonian H_0 in terms of fermions is given by

$$H_0 = \sum_k c_k^\dagger c_k \omega(k), \tag{4.59}$$

where the Fourier transformation to momentum space has already been carried out to diagonalize the Hamiltonian. The grand canonical partition function in the eigenbasis of the fermions reads

$$Z_g(\beta, \mu_0) = \prod_k \left(1 + \exp\left(-\beta\left[\omega(k) - \mu_0\right]\right)\right) \tag{4.60}$$

implying the grand canonical potential

$$J_0(\beta, \mu_0) = \frac{-1}{\beta} \ln Z_g(\beta, \mu_0) \tag{4.61a}$$

$$= \frac{-1}{\beta} \sum_k \ln\left[1 + \exp\left(-\beta\omega(k)\right) \exp\left(\beta\mu_0\right)\right]. \tag{4.61b}$$

In the grand canonical ensemble, the particle number B is no canonic thermodynamic variable so that we cannot simply add the effect of different flavors. Hence we perform

a Legendre transformation to the free energy

$$F_0(\beta, B) = J + \mu_0 B \tag{4.62a}$$

$$\mathrm{d}F_0 = -S\mathrm{d}T + \mu_0 \mathrm{d}B. \tag{4.62b}$$

which reads

$$F_0(\beta, B) = \frac{-1}{\beta} \sum_k \ln\left[1 + \exp\left(-\beta\omega(k)\right) \exp\left(\beta\mu_0(B)\right)\right] + \mu_0(B)B. \tag{4.63}$$

At fixed B, the effect of the different flavors can be accounted for. The additional degree of freedom leads to an entropy increase and hence to a decrease in the free energy

$$F = F_0 - TS_{\text{flavor}} \tag{4.64a}$$

$$= F_0 - \frac{1}{\beta} \ln\left(N_{\text{f}}^B\right) \tag{4.64b}$$

where the flavor entropy $S_{\text{flavor}} = \ln\left(N_{\text{f}}^B\right)$ is determined by the number of flavors N_{f} and the number of thermal excitations B. The free energy F takes the effect of different flavors into account.
In a next step, we calculate the modified chemical potential

$$\mu = \partial_B F(\beta, B) \tag{4.65a}$$

$$= \mu_0 - \underbrace{\frac{1}{\beta} \ln\left(N_{\text{f}}\right)}_{\mu_F(\beta)}. \tag{4.65b}$$

The effect of different flavors is seen in the decrease of the effective chemical potential μ. A short calculation provides us the modified grand canonical potential $J = F - \mu B$ from which we obtain the thermal occupation

$$n_{\text{exact}}(T) = \frac{B(T)}{N N_{\text{f}}} \tag{4.66a}$$

$$= \frac{1}{N} \sum_k \left[\exp\left(\beta\omega(k)\right) + N_{\text{f}}\right]^{-1}. \tag{4.66b}$$

This result shows the correct behaviour for $T = 0 \Rightarrow n(T) = 0$ and for $T \to \infty \Rightarrow n(T) = 1/(1 + N_{\text{f}})$. For $N_{\text{f}} = 1$ the Fermi-function is recovered as it has to be.
We stress, that the mapping to free fermions by the Jordan-Wigner transformation leads to a separation of the flavor and the particle dynamics only for a fixed number of particles. If we consider dynamic correlation functions which involve changes of the number of bosons we do not know of a mapping to a solvable model which makes these correlations tractable.

4.5.3 Evaluation of the multi-flavor equations

In this subsection we discuss the results of the Brückner approach in the multi-flavor case. We focus on the changes upon passing from $N_\mathrm{f} = 1$ to $N_\mathrm{f} = 2$ and $N_\mathrm{f} = 3$. Especially the case $N_\mathrm{f} = 3$ is relevant because it describes triplon excitations in dimerized spin systems. We will evaluate sum rules and the thermal occupation in detail to assess the validity of the Brückner approach on the level of ladder diagrams at finite temperature.

All results are obtained for the nearest neighbor model in Eq. (4.55) without any additional interactions besides the hardcore constraint. We primarily show results for $W/\Delta = 0.5$, i.e., for a narrow band. For comparison, we will also show the thermal occupation function in a wide-band case, $W/\Delta = 4$.

First, we study the thermal occupation which can be computed from the spectral function by

$$n(T) = \frac{1}{2\pi} \int_0^{2\pi} \langle b^\dagger_{k,\alpha} b_{k,\alpha} \rangle \mathrm{d}k = \int_0^{2\pi} \int_{-\infty}^{\infty} \frac{A^\alpha(k,\omega)}{e^{\beta\omega} - 1} \mathrm{d}\omega \mathrm{d}k. \tag{4.67}$$

The thermal occupation is independent of the index α because the bosons of different flavor are degenerate. Figs. 4.4 and 4.5 depict the results for different numbers of flavors obtained by the Brückner approach and compare them to the exact expression (4.66b).

Since our approach is based on a low-temperature approximation in the expansion parameter $\exp(-\beta\Delta)$, we expect deviations to occur if the temperature approaches the value of the energy gap Δ. As seen in chapter 3, the $N_\mathrm{f} = 1$ thermal occupation is approximated very well even at elevated temperatures [61] and even for a vanishing gap [93], only the relative error diverges for $\Delta \to 0$. This holds for $n(T)$; the deviations in the spectral function $A(p,\omega)$ are larger, see section 3.4.

As expected, the diagrammatic and the exact results in Figs. 4.4 and 4.5 agree exellently for small temperatures $T \lesssim 0.3\Delta$. For large temperatures $T \to \infty$ the exact curves yield the value $n(T \to \infty) = 1/(1+N_\mathrm{f})$ corresponding to the value in isolated dimers where all states are equally probable. In contrast to the $N_\mathrm{f} = 1$ case, discernible deviations occur between the approximate and the exact curves for $N_\mathrm{f} > 1$ upon increasing temperature. The Brückner approach on the level of ladder diagrams for $N_\mathrm{f} > 1$ tends to underestimate the thermal occupation at higher temperatures. But we emphasize that for low temperatures the approach works as expected because it is exact in order $\exp(-\beta\Delta)$, see below.

There is also a significant difference between the performance of the ladder approximation for a narrow and for a wide band. At given gap and temperature the relative deviations are significantly smaller for wider bands. In the $W = 4\Delta$ case, the diagrammatic curves stay close to the exact curves even for $T > 0.6\Delta$.

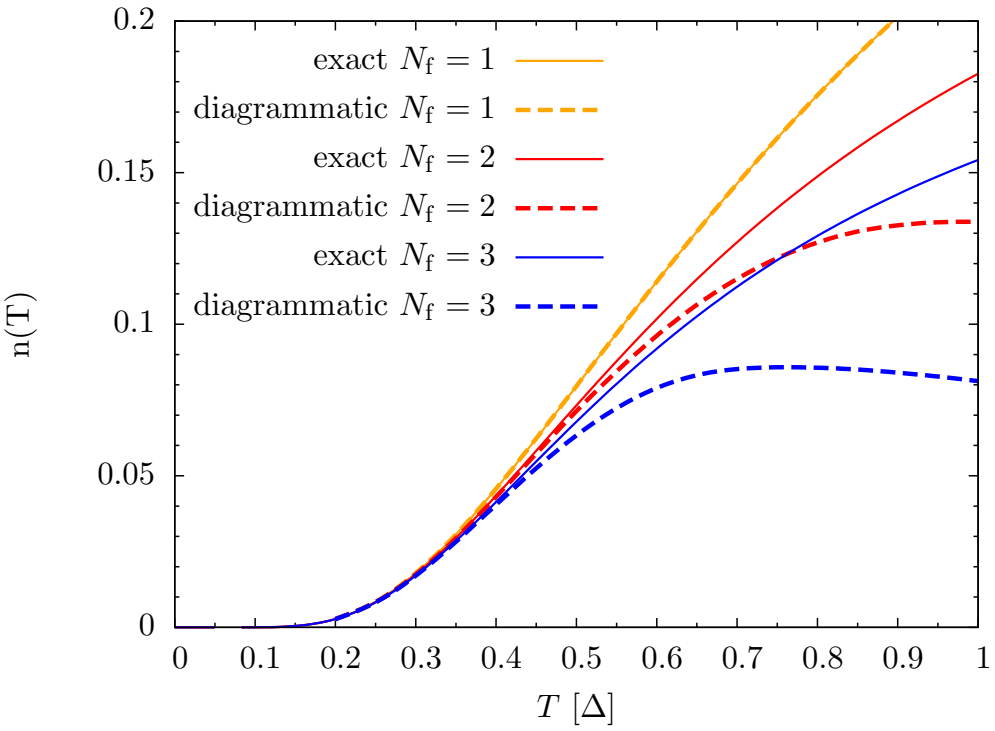

Figure 4.4: Thermal occupation $n(T)$ in the narrow-band case $W = 0.5\Delta$ for various numbers of flavors N_f as function of temperature. Comparison between the exact curves (solid lines) and the diagrammatic results (dashed lines).

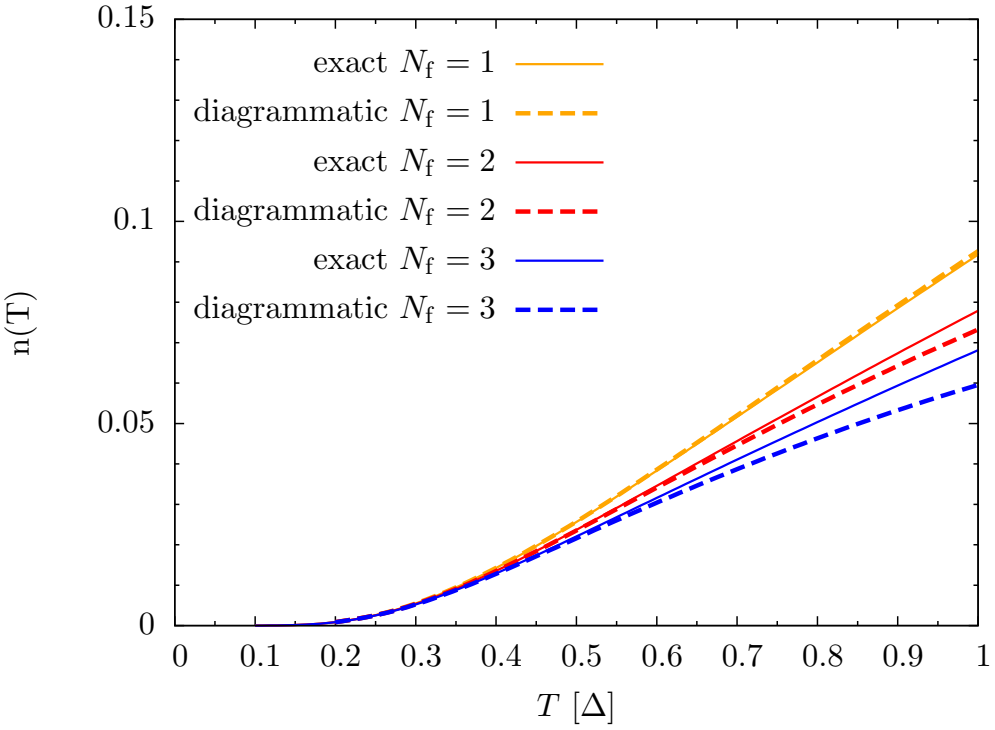

Figure 4.5: Thermal occupation $n(T)$ in the wide-band case $W = 4\Delta$ for various numbers of flavors N_f as function of temperature. Comparison between the exact curves (solid lines) and the diagrammatic results (dashed lines).

In contrast, for $W = 0.5\Delta$, $N_\mathrm{f} = 3$, and $T > 0.75\Delta$ the approximate thermal occupation even shows an unphysical non-monotonic behavior as function of T.
The difference between the two cases can be explained by the different total occupations at the same temperature. For a wide band the fraction of the Brillouin zone with low-lying excitations in the range of T is smaller than for a narrow band so that the total number of thermally excited particles is significantly lower. For this reason, the scattering processes not covered by the ladder diagrams are less important.
This observation implies an important message also for the applicability of the ladder approximation in higher dimensions. There, the fraction of the Brillouin zone at low energies for a given gap is smaller than in one dimension: Assume the gap to occur at $\vec{k} = \vec{0}$ then all components of $\vec{k}$ must be small for the total energy to be small. For a given set of parameters, temperature T, gap Δ, and band width W, one may roughly estimate that the thermal occupation in d dimensions $n_d(T)$ scales like $n_1(T)^d$. Thus we expect that for given parameters the approximation on the level of ladder diagrams is significantly more accurate in higher dimensions.
Next, we will investigate the deviations in one dimension in more detail. Especially, we focus on the quantities that have already been investigated in the single flavor case in chapter 3 and compare them to the multi-flavor case. To this end, we study the sum rule of the spectral function $A(p, \omega)$. In Eq. (4.50) we saw already that the integration of $A(p, \omega)$ over frequency ω is connected to the thermal occupation. Therefore we define the expression

$$R[n(T)] := \int_{-\infty}^{\infty} A^\alpha(x)\mathrm{d}x + (1 + N_\mathrm{f})n(T), \tag{4.68}$$

which should be equal to unity for the exact spectral function. For brevity, we have introduced $A(x) = \frac{1}{N}\sum_p A^\alpha(p, x)$, i.e., the spectral function averaged over momentum p.
The sum rule (4.50) states, that the integral over the momentum dependent spectral function $A(p, \omega)$ is momentum independent. Any approximation to calculate the spectral function is prone to spoil this feature. But in our numerical data we observe that the Brückner approach conserves the exact p-independence within numerical accuracy for all numbers of flavors N_f completely. Thus, there is no need to discuss a momentum dependence of the sum rule. It is sufficient to analyse the quantity $R[n(T)]$.
We plot $R[n(T)]$ as function of temperature in Fig. 4.6. Since for $N_\mathrm{f} > 1$ the thermal occupation $n(T)$ obtained from the spectral function differs from the exact expression in Eq. (4.66b) we depict results for (4.68) for both occupation functions, the one determined diagrammatically and the exact one.

For $N_\mathrm{f} = 1$ the sum rule is fulfilled within numerical accuracy even for temperatures close to the gap Δ. This changes for higher flavor numbers $N_\mathrm{f} > 1$. At low temperatures, the sum rule is well fulfilled because by construction the approach is exact in order $\exp(-\beta\Delta)$. But deviations become discernible at higher temperatures.

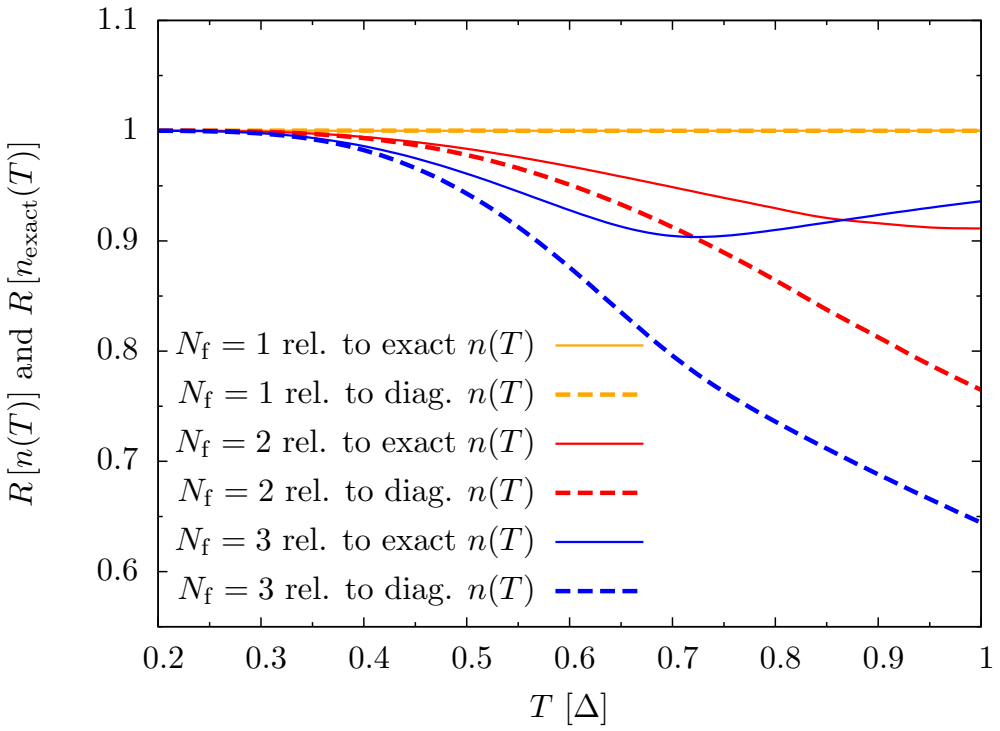

Figure 4.6: The sum rule $R[n(T)]$ from Eq. (4.68) for various numbers of flavors N_f as function of temperature. The bandwidth is fixed to $W = 0.5\Delta$. We compare the quantity $R[n(T)]$ using the diagrammatic $n(T)$ obtained from Eq. (4.67) and $R[n_{\mathrm{exact}}(T)]$ using the exact result from Eq. (4.66b).

Some spectral weight seems to be missing in the approximate Brückner approach. Note, that the sum rule turns out to be better fulfilled using the exact $n_{\mathrm{exact}}(T)$ than using the diagrammatically obtained $n(T)$. Comparing the case $N_\mathrm{f} = 2$ and $N_\mathrm{f} = 3$, one realizes that the relative deviation increases upon increasing the number of flavors.
For a quantitative analysis of the deviations for $N_\mathrm{f} > 1$, Fig. 4.7 depicts the logarithmic deviation $\ln|1 - R[n(T)]|$ of the sum rule in Fig. 4.6 as function of inverse temperature $\beta\Delta$. We use the diagrammatically obtained occupation function $n(T)$ from Eq. (4.67). For low temperatures $T \lesssim 0.3\Delta$, i.e., high inverse temperature $\beta\Delta \gtrsim 3.3$, the deviations are smaller than the numerical accuracy of the data.

Upon increasing temperature the logarithmic deviation scales linearly with inverse temperature indicating an exponential dependence on inverse temperature. We fitted the functions $A\exp(-\beta\Delta)$ and $B\exp(-2\beta\Delta)$ to the data in the low temperature regime $\beta\Delta > 3$. From these fits it is evident, that the deviation indeed scales with $\exp(-2\beta\Delta)$. This is in accord with the construction of the approximation, which was designed to be exact in linear order in $\exp(-\beta\Delta)$. Thus in the next order, i.e. $\propto \exp(-2\beta\Delta)$, deviations cannot be excluded. The analysis provided underpins the correct reasoning in the choice of diagrams and in the implementation of the numerical calculations.
In Fig. 4.8, we additionally show the logarithmic deviation of the sum rule using the exact occupation function $n(T)$ from Eq. (4.66b). Again, the deviation scales as $\exp(-2\beta\Delta)$ indicating that the integral over the spectral function is only correct in first order.

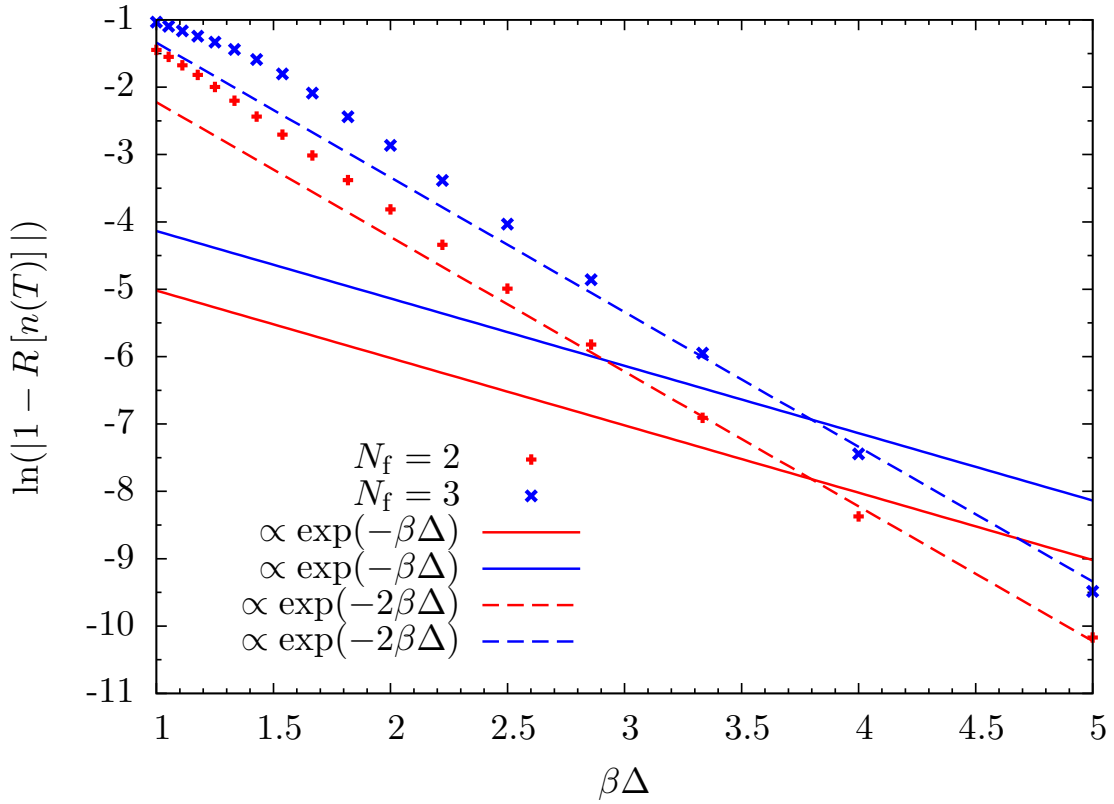

Figure 4.7: Quantitative analysis of the deviation in the calculations of the sum rule for $N_\mathrm{f} > 1$ in Fig. 4.6 as function of inverse temperature $\beta\Delta$. The bandwidth is fixed to $W = 0.5\Delta$. The y-axis shows the logarithmic deviation of the sum rule from 1 using the diagrammatic thermal occupation $n(T)$ from Eq. (4.67). Straight lines indicate exponential dependence of the inverse temperature as expected. The slope indicates the prefactor in the argument of the exponential.

Next, we compare the thermal occupation obtained from the ladder approximation in Eq. (4.67) to the exact expression from Eq. (4.66b) in Fig. 4.9. We show the logarithmic difference of the two expressions as function of the inverse temperature. Surprisingly, the difference scales like $\exp(-3\beta\Delta)$. This indicates a result better than one could expect naively from the construction of the ladder approximation.
We attribute this better-than-expected agreement to the additional averaging of the spectral function over the Bose function in Eq. (4.67). This appears to correct the second order deviation $\exp(-2\beta\Delta)$. We refer the reader to the analogy in leading order: The zero-temperature spectral function corresponds to the zeroth order $\exp(-0\beta\Delta)$ and leads via the Bose function to the correct result for the thermal occupation in first order $\exp(-\beta\Delta)$. Thus one can expect that the spectral function in first order implies the correct thermal occupation in second order.

4.5.4 Analysis at finite U

In the previous subsection, we saw that for $N_\mathrm{f} = 1$ the sum rule is conserved within numerical accuracy and that the thermal occupation is approximated very well by the

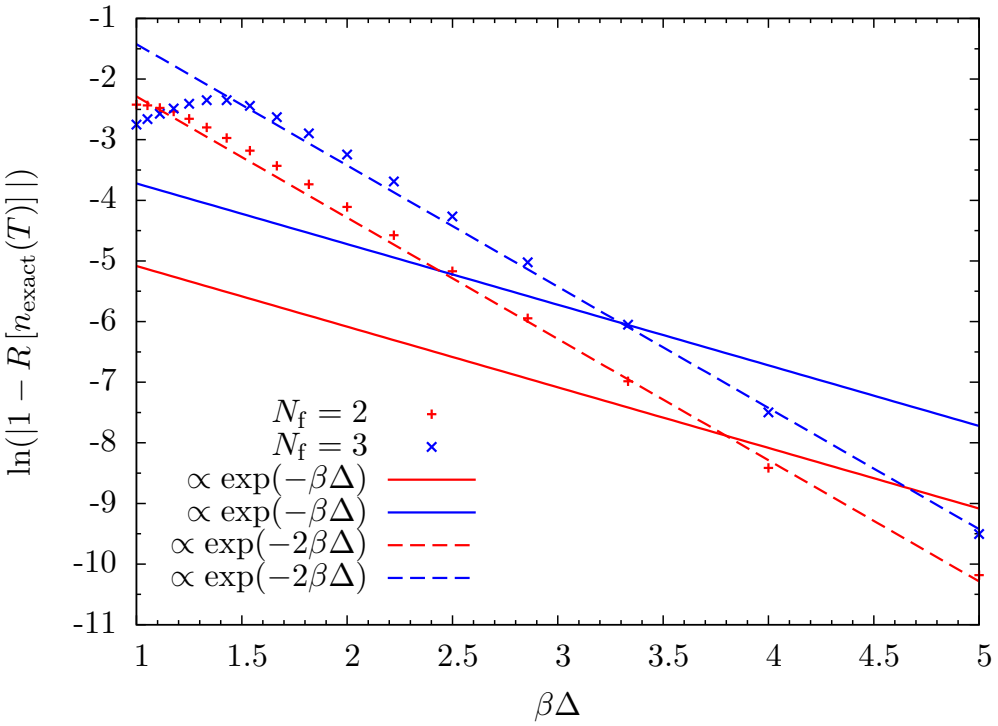

Figure 4.8: Quantitative analysis of the deviation in the calculations of the sum rule for $N_\mathrm{f} > 1$ in Fig. 4.6 as function of inverse temperature $\beta\Delta$. The bandwidth is fixed to $W = 0.5\Delta$. The y-axis shows the logarithmic deviation of the sum rule from 1 using the exact thermal occupation $n_{\mathrm{exact}}(T)$ from Eq. (4.66b), otherwise as Fig. 4.7.

Brückner approach based on ladder diagrams. In contrast, the multi-flavor case represents a less powerful approximation. But we verified, that the occurring deviations are consistent with the systematic construction of the approximation as an expansion in powers of $\exp(-\beta\Delta)$. At low temperatures, the approach works as expected.

Still, these findings are puzzling in view of the concept of conserving approximations introduced by Baym and Kadanoff [79,80] for normal bosons and fermions. If the choice of diagrams yields a conserving approximation for $N_\mathrm{f} = 1$, it is unexpected that this is no longer the case for $N_\mathrm{f} > 1$. We stated, however, already above that the case of hardcore bosons is more subtle anyway. To our knowledge, there is no general argument to prove that a set of diagrams yielding a conserving approximation for normal bosons also implies a conserving approximation for hardcore bosons due to the non-trivial sequence of integration over all frequencies and the limit $U \to \infty$.

The fundamental question is, whether the concept of conserving approximations is generally transferable from normal bosons to hardcore bosons, i.e., independent of the flavor number N_f. To understand this issue better, and to verify that our choice of diagrams provides a conserving approximation for normal bosons, we analyze the approximation of ladder diagrams for finite repulsion U. In this case, the considered particles are normal strongly interacting bosons. Here the Baym-Kadanoff concept of conserving approximations is applicable.

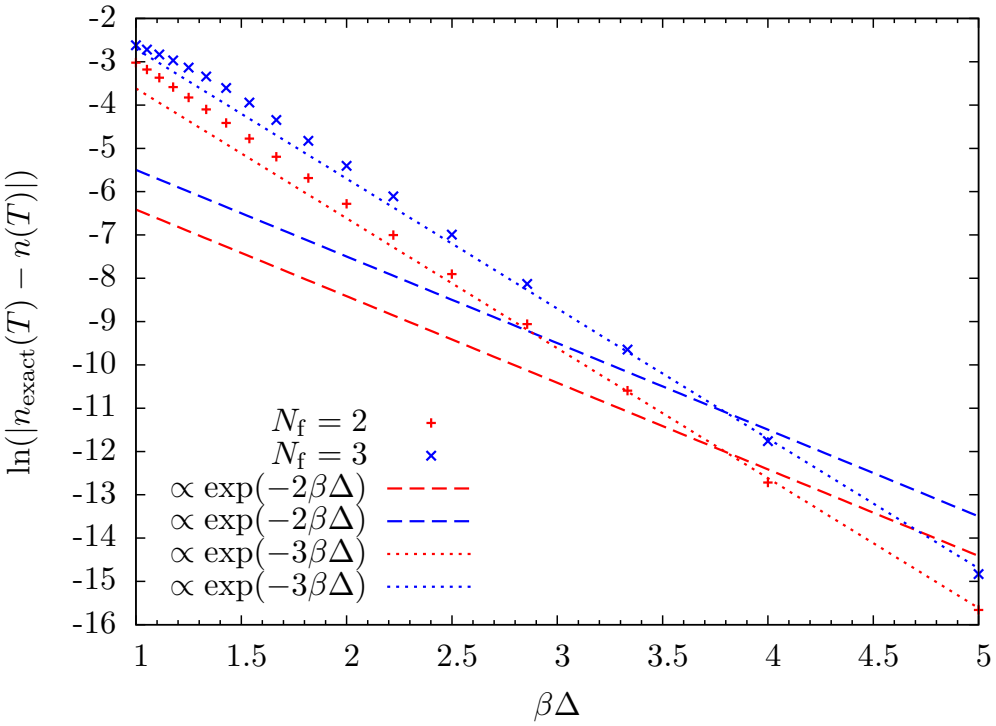

Figure 4.9: Quantitative analysis of the deviations in the calculations of the thermal occupation in Fig. 4.4 as function of inverse temperature $\beta\Delta$ for $N_{\mathrm{f}} > 1$. The bandwidth is fixed to $W = 0.5\Delta$. The y-axis displays the difference between $n_{\mathrm{exact}}(T)$ from Eq. (4.66b) and the diagrammatic $n(T)$ from Eq. (4.67). Unexpectedly, one finds that the deviations scale proportional to $\exp(-3\beta\Delta)$.

We study how the sum rules behave in this case and upon the limit $U \to \infty$. In Figs. 4.10 and 4.11, we compare the spectral line of the scattered bosons for $U = \infty$ with results for $U = 5\Delta$, $U = 10\Delta$ and $U = 20\Delta$. For low temperatures, already the case $U = 5\Delta$ approximates the $U = \infty$ result quite well. Upon increasing temperature larger deviations occur. But clearly, the data for finite values of U slowly converge towards to the results at $U = \infty$.

For bosons with finite on-site interaction the sum rule is constant for all temperatures

$$\int_{-\infty}^{\infty} A^{\alpha}_{\mathrm{Bosonic}}(p, \omega)\mathrm{d}\omega = 1. \tag{4.69}$$

We carefully checked, that the approximation based on ladder diagrams indeed fulfills this sum rule independently of the number of flavors N_{f} and of the temperatures T within numerical accuracy. Since the spectral lines at finite U converge to the result at $U = \infty$ on increasing U, there must be additional weight somewhere in the spectral function to explain the difference to the spectral weight in the $U = \infty$ case.

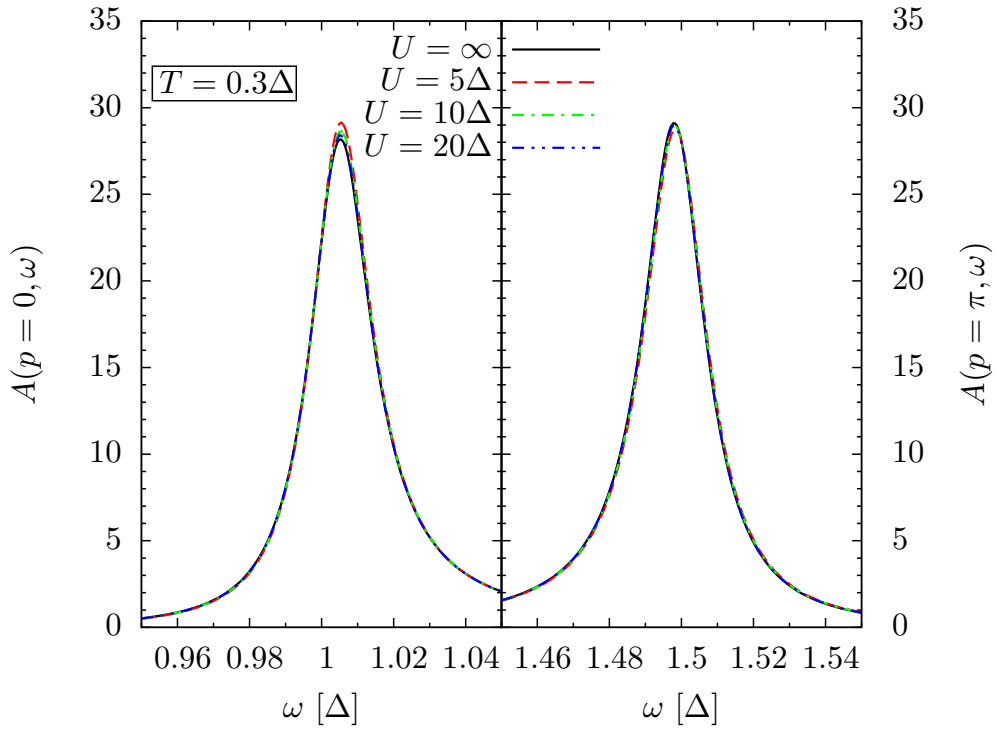

Figure 4.10: Comparison of the spectral lines $A(p, \omega)$ at the gap mode $p = 0$ and at the maximum mode $p = \pi$ for various values of the on-site repulsion U. The temperature is fixed to $T = 0.3\Delta$ and the number of flavors is $N_\mathrm{f} = 3$.

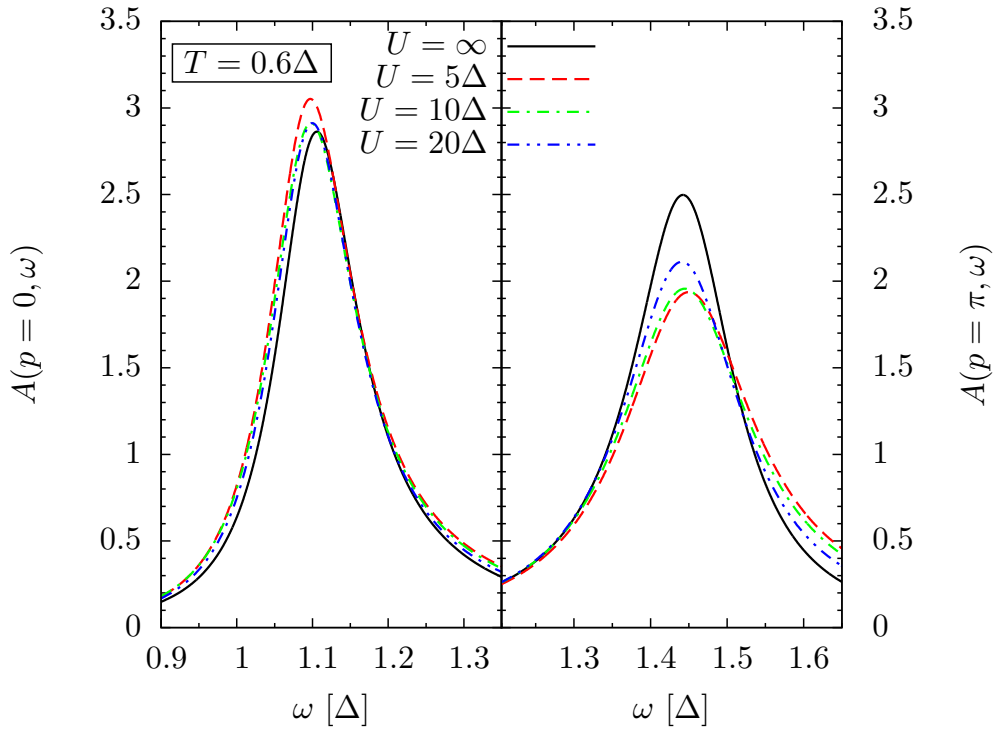

Figure 4.11: Comparison of the spectral lines $A(p, \omega)$ at the gap mode $p = 0$ and at the maximum mode $p = \pi$ for various values of the on-site repulsion U. The temperature is fixed to $T = 0.6\Delta$ and the number of flavors is $N_\mathrm{f} = 3$.

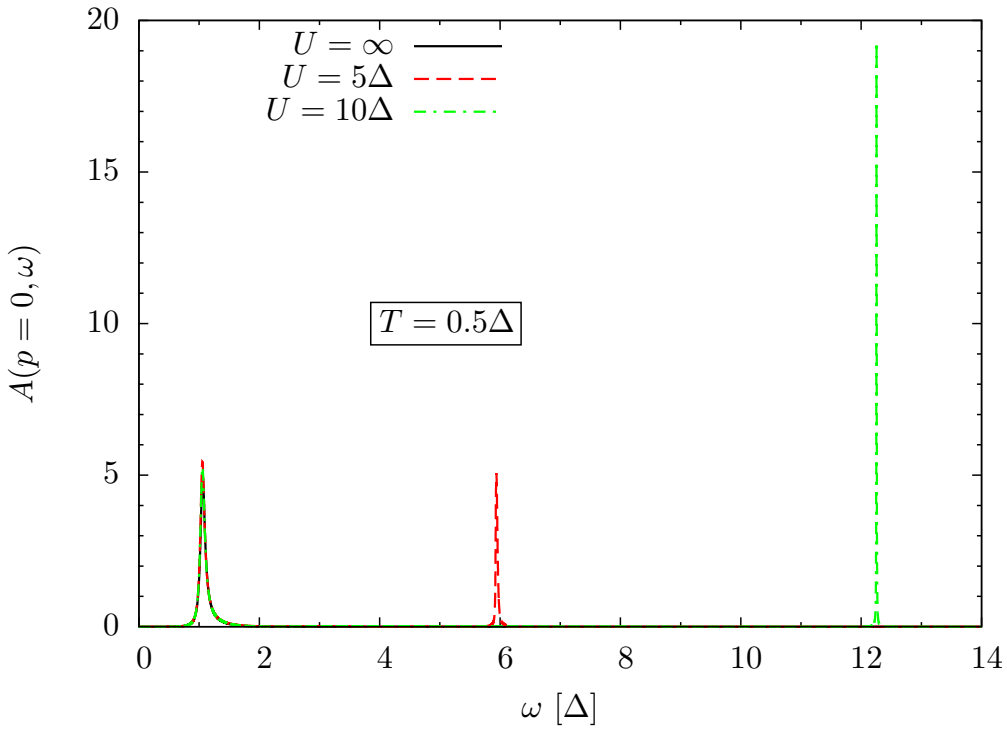

Figure 4.12: Full frequency range comparison of the spectral function $A(p, \omega)$ of the gap mode $p = 0$ for various values of the on-site repulsion U. The temperature is fixed to $T = 0.5\Delta$ and the number of flavors is $N_\mathrm{f} = 3$. At negative frequencies there is only negligible weight for the considered parameters.

We find the additional weight at energies in the range $\omega \approx U$. Figure 4.12 displays the spectral function $A(p, \omega)$ over the whole energy range. For finite U, the additional weight at high energies can be explained by the formation of an anti-bound state of two bosons which repel each other on the same site. The signature of this anti-bound state is found in the spectral function of the scattering amplitude resulting from the Bethe-Salpeter equation (not shown). Clearly, the Bethe-Salpeter equation describes the repeated scattering of two propagating particles. The energy of the anti-bound state is of the order of the repulsion U.
The additional convolution with the third propagator only broadens the line by about the band width W. This is what is seen in Fig. 4.12 at high energies. Take note, that the position of this high-energy feature scales with U. It is this feature, which contains the missing spectral weight for the total sum rule of the single-particle spectral function of normal bosons.

The first key observation for general N_f in the data above is the confirmation that the two limits $U \to \infty$ of the Brückner approach and $\omega \to \infty$ in the integration over the frequencies do not commute. The properties of the hardcore bosons are retrieved, if the limit of infinite repulsion is performed first.
For the finite U case, the ladder diagrams represent a conserving approximation independent of N_f. In the infinite U case, the approximation appears to be a conserving approximation only in the single-flavor case $N_\mathrm{f} = 1$, but not for $N_\mathrm{f} > 1$.

We stress that this does not contradict the results by Baym and Kadanoff, because they formulated conserving approximations for normal bosonic systems with arbitrary, but finite interactions [66]. They also discussed that infinite interactions can be treated by the ladder diagrams, which they call T-matrix approximation in Ref. [66], but did not consider the subtleties of the sequence of limits, i.e., they did not elucidate whether this approximation is conserving for infinite interactions. The single flavor case suggested that the Baym-Kadanoff construction also yields conserving approximations for hard-core bosons. But our calculations for the $N_\mathrm{f} > 1$ falsify this hypothesis. From this observation we deduce that the concept of conserving approximations in the sense of Baym and Kadanoff cannot be carried over to hardcore bosons in general.

5 Thermal dynamics in $BaCu_2V_2O_8$

In this chapter we use the diagrammatic Brückner approach to calculate the finite temperature dynamics in the quantum magnet $BaCu_2V_2O_8$. This renders the opportunity to describe new experimental data and provides a first testing ground for the application of the approach with quantitative predictive power. The chapter is set up as follows: First we will give a short introduction to the material in section 5.1. An effective Hamiltonian will be derived in section 5.2. In section 5.3 the main results are presented, showing that $BaCu_2V_2O_8$ displays asymmetrical line shape broadening at finite temperature. Finally we conclude in section 5.4.

Parts of this chapter have been published in Physical Review B as a Rapid Communication [32] [1]. The manuscript and the interpretation of the data contain contributions from many authors including myself. The results from inelastic neutron scattering were obtained from Ekaterina S. Klyushina and Bella Lake. The fit analysis was also done by Ekaterina S. Klyushina. Alexander C. Tiegel, Salvatore R. Manmana and Andreas Honecker provided the density matrix renormalization group calculations. Additionally I provided the data for the theoretical results of the Brückner approach.

5.1 Structure of $BaCu_2V_2O_8$

The compound $BaCu_2V_2O_8$ is a crystal with tetragonal structure of space group $I\bar{4}2d$ (lattice parameters $a = b = 12.744$Å, $c = 8.148$Å). The magnetic properties of the material originates from the Cu^{2+} ions with spin $S = 1/2$. They are coordinated by O^{2-} ions in square-planar geometry, forming edge-sharing pairs of CuO_4 plaquettes which rotate around the c-axis [94]. The geometry of the crystal is depicted in Fig. 5.1. The interaction between the spins of the copper ions is induced by superexchange interactions through the non-magnetic atoms. Experimental measurements of constant-field magnetic susceptibility χ_{DC} [94,97–99], specific heat [94] and ^{51}V nuclear magnetic resonance [99, 100] showed, that the ground state of the system has no magnetization, implying a strong antiferromagnetic coupling, leading to the formation of Cu^{2+} dimers with a spin-singlet ground state.
Until recently, the exact path and strength of the magnetic interaction in the material was a matter of debate in the literature.

[1]

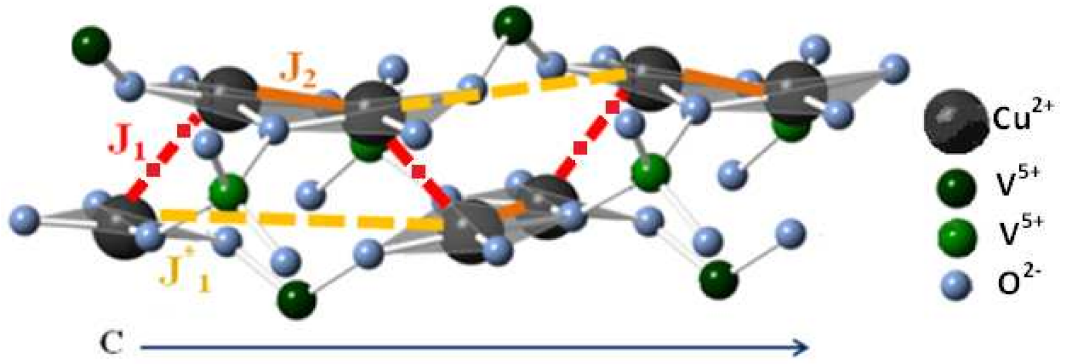

Figure 5.1: Structure of $BaCu_2V_2O_8$ with omitted Ba^{2+} ions. The two proposed models for the dominant magnetic interactions are: (i) two independent linear chains with exchange path J_1^* and J_2, (ii) single screw chain with exchange path J_1 and J_2. Figure taken from Ref. [32].

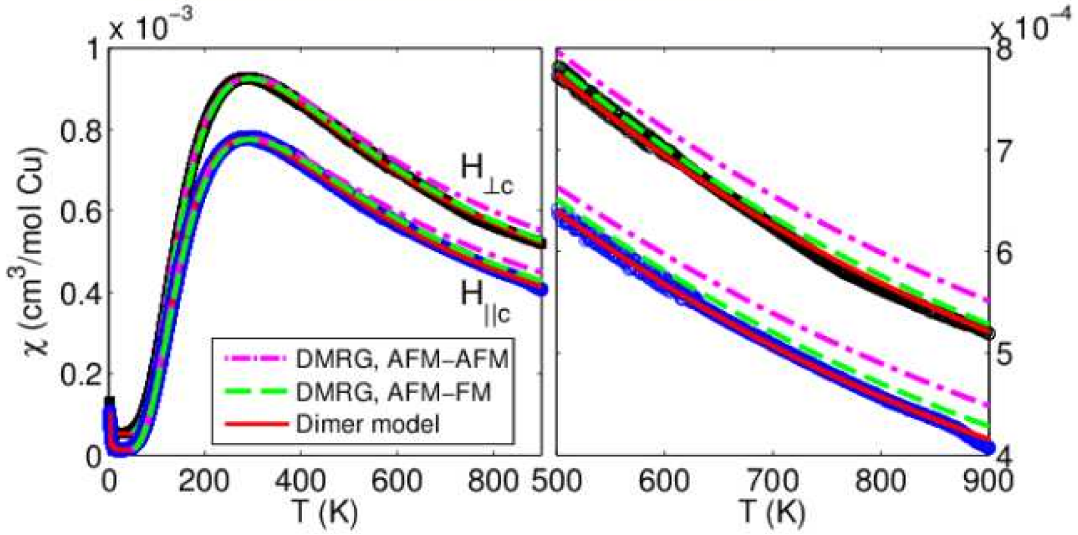

Figure 5.2: Measurement of the static magnetic susceptibility of $BaCu_2V_2O_8$ for a 1 T magnetic field applied parallel $H_{||_c}$ and perpendicular $H_{\perp_c}$ to the c-axis. Comparison with density matrix renormalization group (DMRG) calculations assuming an AFM and FM interdimer coupling. The exchange constants for the DMRG calculation are extracted from the INS measurements. The solid line is the coupled dimer model [95, 96] where the g-factors and exchange constants were fitted. Figure taken from Ref. [32].

Two models have been proposed, both shown in Fig. 5.1: (i) the main exchange path consists of superexchange path J_2 (Cu-O-Cu) and super-superexchange path J_1^* (Cu-O-V-O-Cu), leading to two straight, independent, dimerized chains along the c-axis, (ii) the main exchange path includes J_2 and super-superexchange path J_1, leading to a single screw chain with a periodicity (up to the winding symmetry) which is half of the c lattice parameter. Both models assume, that the intradimer interaction is AFM and given by J_1^* and J_1 respectively. Whereas the interdimer interaction was assumed to be AFM with a strength between 0 % and 20 % of the intradimer coupling [94, 97–100]. However a possible ferromagnetic interaction between the dimers was neglected in the assumptions.

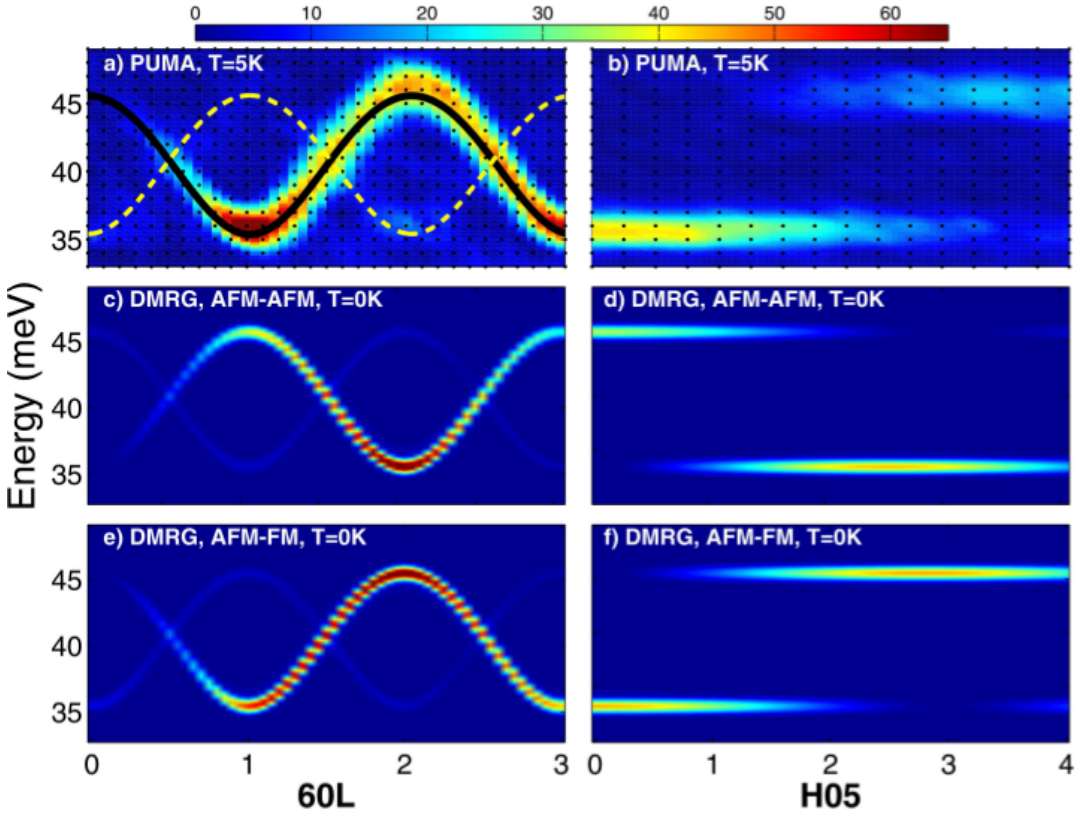

Figure 5.3: Top panel: Background-subtracted INS data for the single triplon excitation at base temperature. The left side shows measurements along the dispersive c-axis, the right side is along the non-dispersive a-axis. The dashed and solid lines show the one-triplon dispersion to fifth order for the J_{intra}-J_{inter} model with AFM-AFM ($J_{\text{intra}} = 40.75$ meV, $J_{\text{inter}} = 9.16$ meV) and AFM-FM ($J_{\text{intra}} = 40.92$ meV, $J_{\text{inter}} = -11.97$ meV) interactions, respectively. Middle and bottom panel: The corresponding DMRG results for the dynamic structure factor for the J_{intra}-J_{inter} model. Figure taken from Ref. [32].

In Ref. [32] static magnetic susceptibility measurements are combined with inelastic neutron scattering and MPS/DMRG calculations to determine the interaction strength as well as the possible exchange path rigorously. Fig. 5.2 shows the measurements of the static magnetic susceptibility of $BaCu_2V_2O_8$ compared with two DMRG calculations assuming an AFM and FM interdimer coupling, and a simple coupled dimer model calculation. The values for the interaction strength used in the DMRG calculations have been obtained from fits to the single triplon dispersion, see below. For the static magnetic susceptibility the FM interdimer coupling shows a better agreement, especially at higher temperatures $T > 500$K.

The assumption of a FM interdimer interaction is supported by INS measurements of the single particle sector, shown in Fig. 5.3. The AFM-FM model provides the best match with the intensity pattern of the experiment. From the INS results it is also possible to determine the periodicity of the mode, which is half of the lattice parameter c. This confirms the screw chain arrangement of the interactions, because for a straight chain the periodicity should be c. Note, that a weaker mode appears as well due to the screw chain geometry of the compound. Although this analysis shows, that the exchange path

is given by J_1 and J_2, it is not possible to determine, which of the two couplings is the intra-dimer and which is the inter-dimer coupling. Due to the fact, that band structure calculations predicts, that the super-superexchange path J_1 provides the strongest AFM interaction [98], it is most likely that $J_1 = J_{\text{intra}}$ and $J_2 = J_{\text{inter}}$ holds.

5.2 Effective model

Using the exchange couplings determined in the previous section, the magnetic properties of $BaCu_2V_2O_8$ are described by the $S = 1/2$ alternating Heisenberg chain with exchange couplings given by $J_{\text{intra}} = 40.92$ meV and $J_{\text{inter}} = -11.97$ meV. Although the screw-geometry has an influence on the static properties of the material, such as the static structure factor, dynamic properties can be described by a pure 1D Hamiltonian

$$H = \sum_i J_{\text{intra}}\, \vec{S}_{i,1} \cdot \vec{S}_{i,2} + J_{\text{inter}}\, \vec{S}_{i,2} \cdot \vec{S}_{i+1,1}, \tag{5.1}$$

where the indices i denotes dimers on an infinite, one-dimensional lattice and the indices $1, 2$ refer to the first and second spin of the dimer respectively.
To apply the diagrammatic Brückner appraoch, we derive an effective model, which conserves the number of quasi-particles in the system, using the deepCUT method introduced in section 4.1. The effective Hamiltonian is written in terms of triplon operators acting on the ground state, i.e. the vacuum of excitations [51].
To that end, we introduce the basis states for single dimers. First, the singlet state is given by

$$|0\rangle = |s\rangle = \frac{1}{\sqrt{2}} \left(|{\uparrow\downarrow}\rangle - |{\downarrow\uparrow}\rangle \right), \tag{5.2}$$

which is identified as the vacuum of triplon excitations. The three triplet states are defined by

$$t_x^\dagger |0\rangle = |x\rangle = \frac{-1}{\sqrt{2}} \left(|{\uparrow\uparrow}\rangle - |{\downarrow\downarrow}\rangle \right), \tag{5.3a}$$

$$t_y^\dagger |0\rangle = |y\rangle = \frac{i}{\sqrt{2}} \left(|{\uparrow\uparrow}\rangle + |{\downarrow\downarrow}\rangle \right), \tag{5.3b}$$

$$t_z^\dagger |0\rangle = |z\rangle = \frac{1}{\sqrt{2}} \left(|{\uparrow\downarrow}\rangle + |{\downarrow\uparrow}\rangle \right). \tag{5.3c}$$

The triplet states represent hardcore bosons because on a single dimer only one excitation is allowed at maximum. The hardcore algebra for the creation and annihilation operators on the whole lattice is given by

$$\left[t_{i,\alpha}, t_{j,\phi}^\dagger \right] = \delta_{ij} \left(\delta_{\alpha\phi} \left(1 - \sum_\gamma t_{i,\gamma}^\dagger t_{i,\gamma} \right) - t_{i,\phi}^\dagger t_{i,\alpha} \right), \tag{5.4}$$

where $\alpha, \phi \in \{x, y, z\}$ denote the three possible flavors of the excited triplons. Then we can rewrite all possible Heisenberg exchange interactions between two spin-1/2 of the dimers using the triplon algebra

$$\vec{S}_{i,1} \cdot \vec{S}_{i,2} = -\frac{3}{4} + \sum_{\alpha} t^{\dagger}_{i,\alpha} t_{i,\alpha}, \tag{5.5a}$$

$$4\vec{S}_{i,1} \cdot \vec{S}_{j,1} = T_2(i,j) + T_{3+}(i,j) + T_4(i,j), \tag{5.5b}$$

$$4\vec{S}_{i,2} \cdot \vec{S}_{j,2} = T_2(i,j) - T_{3+}(i,j) + T_4(i,j), \tag{5.5c}$$

$$4\vec{S}_{i,1} \cdot \vec{S}_{j,2} = -T_2(i,j) + T_{3-}(i,j) + T_4(i,j), \tag{5.5d}$$

$$4\vec{S}_{i,2} \cdot \vec{S}_{j,1} = -T_2(i,j) - T_{3-}(i,j) + T_4(i,j), \tag{5.5e}$$

where

$$T_2(i,j) = \sum_{\alpha} \left(t^{\dagger}_{i,\alpha} t_{j,\alpha} + t^{\dagger}_{i,\alpha} t^{\dagger}_{j,\alpha} \right) + \text{h.c.}, \tag{5.6a}$$

$$T_{3\pm}(i,j) = \sum_{\alpha\phi\gamma} i\epsilon_{\alpha\phi\gamma} \left(t^{\dagger}_{i,\alpha} t^{\dagger}_{j,\phi} t_{j,\gamma} \pm t^{\dagger}_{j,\alpha} t^{\dagger}_{i,\phi} t_{i,\gamma} \right) + \text{h.c.}, \tag{5.6b}$$

$$T_4(i,j) = \sum_{\alpha \neq \phi} t^{\dagger}_{i,\alpha} t_{i,\phi} t^{\dagger}_{j,\phi} t_{j,\alpha} - t^{\dagger}_{i,\alpha} t_{i,\phi} t^{\dagger}_{j,\alpha} t_{j,\phi} \tag{5.6c}$$

The perturbation parameter for the deepCUT approach is given by $x = J_{\text{inter}}/J_{\text{intra}}$. Up to first order the effective Hamiltonian in terms of triplon operators is given by

$$\frac{H_{\text{eff}}}{J_{\text{intra}}} = E_0 + \sum_i \sum_{\alpha} t^{\dagger}_{i,\alpha} t_{i,\alpha} - \frac{x}{4} \sum_i \sum_{\alpha} \left(t^{\dagger}_{i,\alpha} t_{i+1,\alpha} + \text{h.c.} \right) \tag{5.7a}$$

$$+ \frac{x}{4} \sum_i \sum_{\alpha \neq \phi} t^{\dagger}_{i,\alpha} t_{i,\phi} t^{\dagger}_{i+1,\phi} t_{i+1,\alpha} - t^{\dagger}_{i,\alpha} t_{i,\phi} t^{\dagger}_{i+1,\alpha} t_{i+1,\phi} + \mathcal{O}(x^2). \tag{5.7b}$$

where E_0 is the ground state energy. Since $x \approx -0.3$ in the case of $BaCu_2V_2O_8$, an order 6 calculation for the deepCUT is sufficient to capture all quantum fluctuations at zero temperature quantitatively, i.e., H_{eff} is known up to all terms in order x^6.

5.3 Dynamical correlations in $BaCu_2V_2O_8$

Since $BaCu_2V_2O_8$ is an excellent example of a quantum magnet with flavored excitations above an energy gap, it provides an ideal testbed to compare the theoretical prediction of the diagrammatic Brückner approach with experimental data, as well as predictions from DMRG. On top, the material provides a rare AFM-FM coupling, which was so far not examined in literature with regard to coherent dynamics at finite temperature.
We apply the Brückner approach on top of the effective Hamiltonian in Eq. (5.7), with the parameters from section 5.1. Since the effective Hamiltonian includes also other two-particle interactions, besides the hard-core constraint, we apply a self-consistent

mean-field approximation to account for the effects of the additional interaction on the level of the real part of the self-energy, see also section 4.2. Hence we decouple all quartic interactions other than the infinite local repulsion in the effective Hamiltonian according to

$$\begin{aligned} t^\dagger_{i,\alpha} t^\dagger_{i+d_1,\phi} t_{i+d_2,\gamma} t_{i+d_3,\xi} \approx & \left\langle t^\dagger_{i,\alpha} t_{i+d_2,\gamma} \right\rangle t^\dagger_{i+d_1,\phi} t_{i+d_3,\xi} + \left\langle t^\dagger_{i,\alpha} t_{i+d_3,\xi} \right\rangle t^\dagger_{i+d_1,\phi} t_{i+d_2,\gamma} \\ & + \left\langle t^\dagger_{i+d_1,\phi} t_{i+d_2,\gamma} \right\rangle t^\dagger_{i,\alpha} t_{i+d_3,\xi} + \left\langle t^\dagger_{i+d_1,\phi} t_{i+d_3,\xi} \right\rangle t^\dagger_{i,\alpha} t_{i+d_2,\gamma} + \text{const.} \end{aligned} \tag{5.8}$$

The screw chain geometry is not taken into account, since we are only interested in the temperature dependence of the gap mode at fixed momentum $p = 0$. The main effect of the screw is the appearance of a second, much weaker mode in frequency space, clearly separated from the gap mode. We also the neglect vertex corrections discussed in section 4.3 because their effects are negligibly small in the parameter regime investigated.
The quantity of interest is the dynamic structure factor which is related to the spectral function by means of the fluctuation-dissipation theorem in Eq. (2.4). To compare the diagrammatic results with the experimental data, the finite resolution of the experiment must be taken into account. The resolution is modelled with the function

$$R(\omega) = \frac{\exp\left(\frac{-(\omega-\omega_0)^2}{2\left(\frac{W_G}{2\sqrt{2\ln(2)}}+\gamma(\omega-\omega_0)\right)^2}\right)}{\sqrt{2\pi}\left(\frac{W_G}{2\sqrt{2\ln(2)}}+\gamma(\omega-\omega_0)\right)}. \tag{5.9}$$

Here ω_0 denotes the peak position and W_G is the width of the peak at half hight. The parameter γ produces an intrinsic asymmetry in the resolution function; it has been included to except the possibility, that the asymmetry observed in the intensity at higher temperature is an effect of the experimental equipment. The parameters are determined at base temperature ($T \approx 3.5$ K), which is small, compared to the energy gap $\Delta \approx 35\text{meV} \approx 412\text{K} \cdot k_\text{b}$. For finite temperature the resolution function is then convolved with the results of the diagrammatic Brückner approach, to make theory and experiment comparable.

A set of high resolution energy scans at the gap mode was measured in INS at six different temperatures from 3.5K up to 200K. The background subtracted data are shown in Fig. 5.4 in panel a)-f). The results of the Brückner approach are labelled "DBA-CUT", which stands for diagrammatic Brückner approach in combination with continuous unitary transformations. Panel a) shows the INS spectrum at the lowest temperature, which realizes the zero temperature limit effectively. The resolution function is shown as a red curve and the DMRG data are shown as blue curves. By definition, the Brückner approach has a sharp delta function at $T = 0$, hence the results at base temperature are identical to the resolution function, after the convolution.

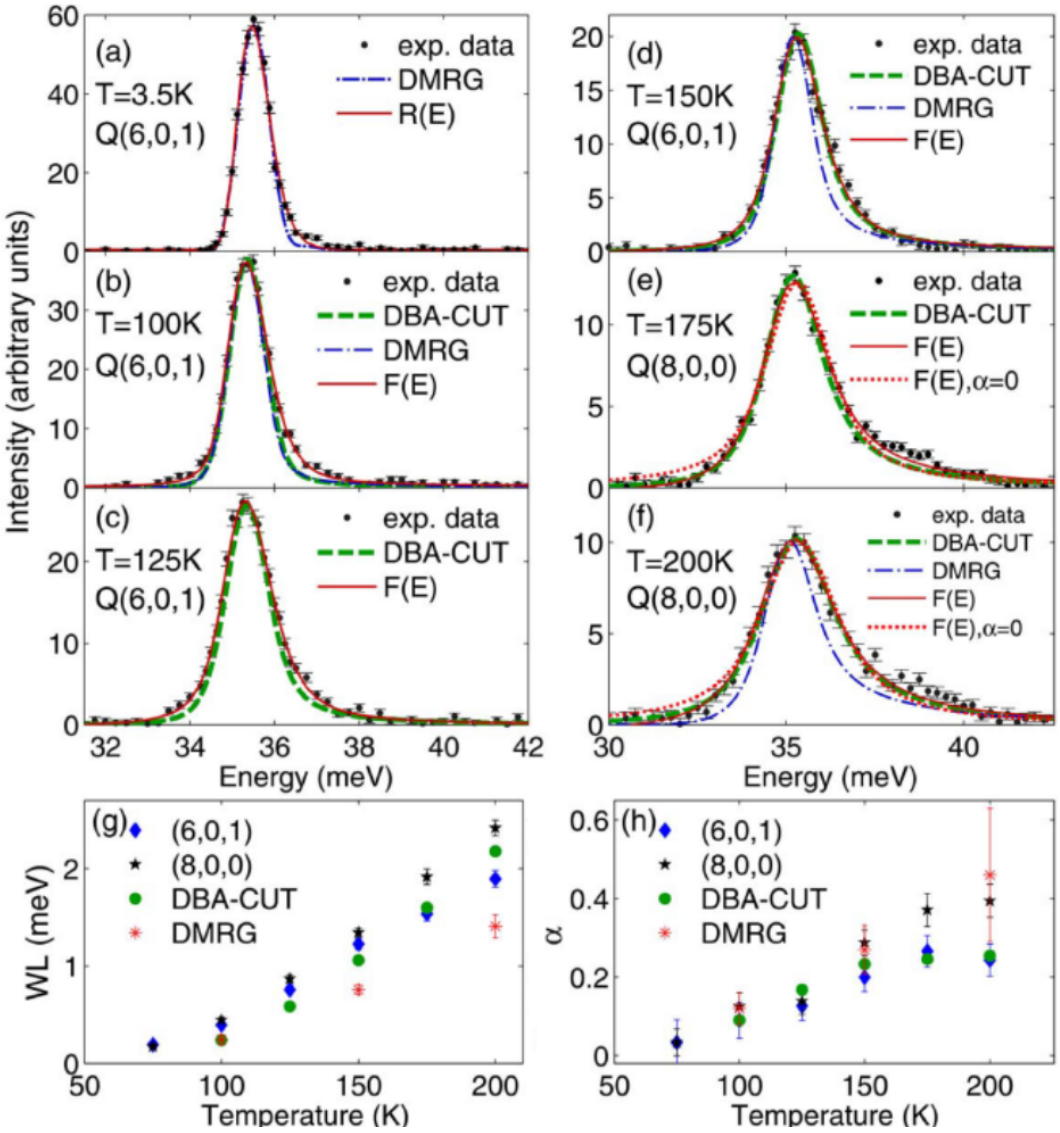

Figure 5.4: a)-f) INS spectrum of the single particle response at the gap modes (6,0,1) and (8,0,0) measured at different temperatures. Comparison to fits with Eq. (5.11) (red) and theoretical data from DMRG (blue) and DBA-CUT (green). g) Fitted linewidth as function of temperature, with comparison between experimental and theoretical data. h) Fitted asymmetry of the peak as function of temperature, with comparison between experimental and theoretical data. Figure taken from Ref. [32].

Upon increasing temperature, the peak width increases and develops an asymmetric tail towards higher energies. This asymmetric tail cannot be explained by a simple Lorentzian broadening, but it is the result of non-trivial scattering processes at finite temperature.

The specific shape of the peak is well reproduced by the diagrammatic Brückner approach and describes the experimental data quantitatively, up to high temperatures.

For higher temperature the results from the Brückner approach have been slightly shifted in energy to fit the experimental data. There are two reasons for the offset in frequency between experimental data and the theoretical results: (i) The crystal is subject to lattice distortion due to the wide temperature range considered in the experiment. This

leads to a change in the interaction strength which shifts all energy scales. This has been modelled by a temperature dependent J_1 in Ref. [32]. (ii) The diagrammatic Brückner approach is not able to capture the leading order of the energy shift, since the dispersion is dominated by the leading cosine term. In case of a pure cosine dispersion, it is shown in chapter 3, that the shift is an effect in order $\exp(-2\beta\Delta)$, which is not captured correctly in first order perturbation theory.

To quantify the peak width and asymmetry more specifically, we introduce a fitting function, which is a Lorentzian $L(W_L, \omega)$ where the width W_L has been replaced by $W_L \to W_L + \alpha(\omega - \omega_0)$ to model the asymmetry of the peak,

$$L\left(W_L + \alpha(\omega - \omega_0), \omega\right) = \frac{1}{\pi} \frac{\frac{W_L + \alpha(\omega - \omega_0)}{2}}{\left(\omega - \omega_0\right)^2 + \left(\frac{W_L + \alpha(\omega - \omega_0)}{2}\right)^2} \tag{5.10}$$

The fitting function must be convolved with the experimental resolution function,

$$F(\omega) = \frac{A}{\pi} \cdot L\left(W_L + \alpha(\omega - \omega_0), \omega\right) * R(\omega) \tag{5.11}$$

and the resulting function $F(\omega)$ can then be used to fit the data, using the parameters A, W_L, ω_0 and α. Note, that the parameter α quantifies the degree of the asymmetry. Experimental, DMRG as well as DBA-CUT data have been fitted with this method and the results for the width and asymmetry are found in Fig. 5.4 panel g) and h). At $T = 175$K and $T = 200$K we also plotted the fitting function with the asymmetry parameter α set to zero. This shows, that the data cannot be described, by a pure Lorentzian decay in frequency space.

Upon increasing temperature, the width as well as the asymmetry increase. Both quantities are described very well by the theories, with the DBA-CUT being better to resolve the peak width. This analysis shows, that a quantitative description of quantum correlations at finite temperature is in reach with the diagrammatic Brückner approach.

5.4 Conclusion

In this chapter we analyzed the quantum magnet $BaCu_2V_2O_8$, which realizes the $S = 1/2$ alternating Heisenberg chain with a rare ferromagnetic interdimer interaction. We applied the diagrammatic Brückner approach to model the specific shape of the single particle INS spectrum. First we derived an effective model based on CUT calculations to describe the dynamics of triplons in the system at zero temperature. This effective model served as an input for the Brückner approach to determine the frequency dependent dynamics at finite temperature. It was shown, that although the position of the peak was hard to catch, the approach yields a very good description of the width and shape of the experimental data. The asymmetry in the data shows, that quantum correlations in the system can extend even into the finite temperature regime. The deeper reason for the persisting quantum correlations can be traced back to the hard-core constraint of the underlying excitations in the system.

6 Finite temperature dynamics in the time domain: $Cu(NO_3)_2 \cdot 2.5$ D_2O

In this chapter we will investigate the dynamical correlations of $Cu(NO_3)_2 \cdot 2.5$ D_2O (copper nitrate) using a combination of high resolution neutron resonance spin-echo triple-axis spectroscopy (NRSE-TAS) and the diagrammatic Brückner approach. This renders the opportunity to explore non-conventional thermal decoherence in the time domain. In the first section 6.1 we will introduce the material and some of the research conducted on it in recent years. Next, we give some details on the experiment and on the effective model in section 6.2. We compare the experimental data with the theoretical results in section 6.3 and conclude in section 6.4.

Parts of this chapter have been published in Physical Review B as a Rapid Communication [101] [1]. The manuscript and the interpretation of the data contain contributions from many authors including myself. The experimental results from NRSE-TAS were obtained from F. Groitl, T. Keller, K. Rolfs, D. A. Tennant and K. Habicht. I provided the data for the theoretical results of the Brückner approach.

6.1 Magnetic couplings in copper nitrate

Using conventional INS and high field magnetization measurements it has been shown that copper nitrate ($Cu(NO_3)_2 \cdot 2.5$ D_2O) is a model material for a one dimensional alternating Heisenberg chain (AHC) [102,103]. The compound has a monoclinic structure with space group I12/c1 (lattice parameters $a = 16.1$Å, $b = 4.9$Å, $c = 18.8$Å, $\beta = 93.8°$). The copper ions carry a spin-1/2 which are coupled antiferromagnetically to form two equivalent chains, which lie along the $[\frac{1}{2}, \frac{1}{2}, \frac{1}{2}]$ and $[\frac{1}{2}, \frac{-1}{2}, \frac{1}{2}]$ directions. They project onto the same direction on the $(h\,0\,l)$ plane.
Similar to $BaCu_2V_2O_8$, the spins form dimers at low temperature leading to a singlet ground state and triplon excitations.

[1]

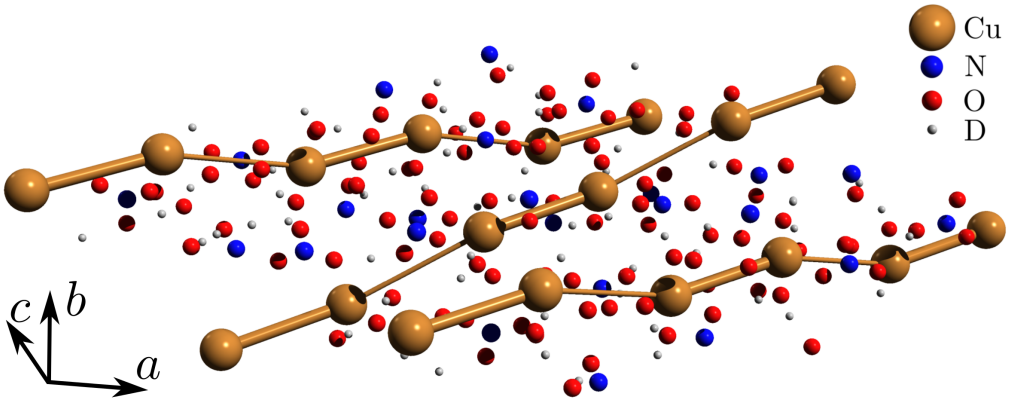

Figure 6.1: Symbolic representation of the crystal structure and the magnetic interactions in $Cu(NO_3)_2 \cdot 2.5\ D_2O$. The large bonds represent the dimers formed by the spin-1/2 of the Cu Atoms, whereas the weak inter-dimer coupling is shown as small bonds between the dimers. The coupled dimers form two equivalent chains, running along the $[\frac{1}{2}, \pm\frac{1}{2}, \frac{1}{2}]$ directions.

The values for the intradimer ($J = 0.443\,\text{meV}$) and interdimer ($J' = 0.101\,\text{meV}$) couplings were first determined by Bonner et. al. in 1983 using measurements of susceptibility, magnetization, and specific heat [103]. The crystal structure and the magnetic interactions are depicted in Fig. 6.1.
Several studies revealed, that copper nitrate displays interesting phenomena at finite temperature. As first Xu et. al. discovered, that the single triplon mode narrows in energy upon increasing temperature [22]. Investigations using inelastic neutron scattering show an asymmetric thermal line shape broadening in the frequency domain [24, 104].

6.2 Experimental details and effective model

The most recent experimental analysis was done in the time domain using the high resolution neutron resonance spin-echo triple-axis spectroscopy (NRSE-TAS) [105]. The advantage of NRSE-TAS [106, 107] is, that it gives access to slow processes corresponding to energies in the μeV range, which are not accessible by conventional INS. Neutron spin-echo measures the polarization of the neutron beam $P = \langle \sigma_x \rangle$, as function of delay time τ. It can be shown, that the echo amplitude is a direct measure of the time dependent Fourier transform of the dynamic structure factor, called the intermediate scattering function $I(\mathbf{Q}, \tau)$ [108, 109]. By mapping the data obtained in time domain, using a phenomenological model, it was shown, that NRSE-TAS is capable of describing asymmetric line shape broadening effectively.
The aim of this chapter is to reinvestigate the data obtained in [105] using the diagrammatic Brückner approach. Instead of transforming the experimental data into frequency domain, which is subject to error prone fitting, we transform the highly resolved theoretical prediction to time domain and directly compare the shape with the experimental data.

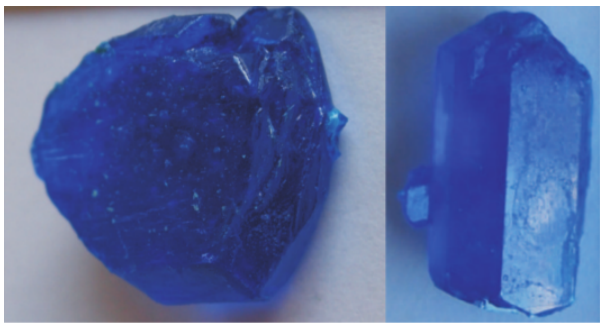

Figure 6.2: Two highly deuterated copper nitrate single crystals. They are grown using enrichment and solution growth method at the Helmholtz-Zentrum Berlin. Picture taken from Ref. [110]

This approach has two advantages: i) The time domain is the natural dimension for the observation of decaying correlations, offering a complementary view to the frequency domain on this phenomenon. ii) The transformation of the theoretical data can be done in a controlled fashion, requiring only a numerical Fourier transformation and no fitting. Finally we will compare the data to a purely statistical model [29], which predicts a Lorentzian line shape in frequency domain and correspondingly an exponential decay in the time domain. In this model the temperature dependence enters only in the width of the peak, but the form and weight is fixed.
The $(Cu(NO_3)_2 \cdot 2.5\ D_2O)$ crystal analyzed was grown at the Helmholtz-Zentrum Berlin. It has a sample mass of 4 g and a deuteration ratio of $> 99.38\%$. It is shown on the left side of Fig. 6.2. Note, that the crystal was grown from powder samples of $(Cu(NO_3)_2 \cdot 2.5\ H_2O)$ [110]. The water was replaced with deuterium using the enrichment and solution growth method, since water produces a high incoherent cross section in INS, while the cross section of deuterium is comparably low.
Copper nitrate is a model material for the spin-1/2 AHC [22]. Its Hamiltonian reads

$$H = \sum_r J\mathbf{S}_r^{\mathrm{L}} \cdot \mathbf{S}_r^{\mathrm{R}} + J'\mathbf{S}_r^{\mathrm{R}} \cdot \mathbf{S}_{r+1}^{\mathrm{L}}. \tag{6.1}$$

The index r denotes dimers with strong interaction J and R, L refer to right and left spin of the dimer respectively. The dimers are coupled by a weaker interaction J'. A graphical representation of the model is given in Fig. 6.3.

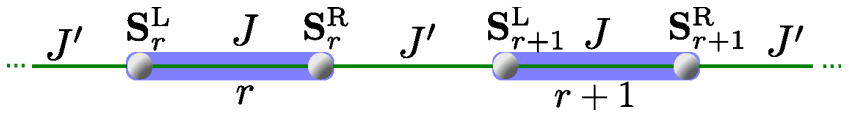

Figure 6.3: Sketch of the couplings in the Hamiltonian of the alternating Heisenberg chain.

For copper nitrate the coupling constants are $J = 0.443\,\mathrm{meV}$ and $J' = 0.101\,\mathrm{meV}$ [24]. Hence the alternation ratio $x = J'/J \approx 0.227$ is rather small and the ground state of the chain is close to the product state with singlets on each dimer, $\prod_r |s\rangle_r = \prod_r \left(|{\uparrow\downarrow}\rangle_r - |{\downarrow\uparrow}\rangle_r\right)/\sqrt{2}$.

The gap of the first excitations is given by $\Delta = 0.385\,\mathrm{meV} \approx 4.5\,\mathrm{K}k_\mathrm{B}$.
As in the case of $BaCu_2V_2O_8$, we introduce triplon operators to obtain a quasi-particle picture of the Hamiltonian [111]. To capture the zero temperature quantum fluctuations quantitatively, we apply a deepCUT [63] to map the Hamiltonian onto an effective Hamiltonian that conserves the number of triplons in the system. To first order in the parameter x the effective Hamiltonian is given by (5.7). Note, that in contrast to $BaCu_2V_2O_8$, copper nitrate has a positive alternation ratio: The strong interaction as well as the weak interaction are anti-ferromagnetic. In the calculations, the effective Hamiltonian up to order 6 is used, which is sufficient to capture all quantum effects in the model.
On top of this effective Hamiltonian we apply the Brückner approach to calculate the finite temperature effects on the spectrum. The additional interaction was included using the method described in section 4.2. The quantity of interest for inelastic neutron scattering is the dynamic structure factor which is related to the imaginary part of the Green function by means of the fluctuation-dissipation theorem. The single quasi-particle peak is the dominant contribution to the dynamic structure factor [92] and corresponds to the observable measured in NRSE-TAS. Vertex corrections are left out because their effects are negligibly small in the parameter regime investigated.

6.3 Results

Fig. 6.4 shows the spectral function, as obtained from the Brückner approach for $T = 0.5$K and $T = 2$K. For very low temperatures the response is sharply peaked at the position of the dispersion. As temperatures increases, the width of the peak increases, signalling a decrease in coherence. Note the asymmetric tail towards higher energies at $T = 2$K, especially when compared to a pure symmetric Lorentzian fit.
Since the NRSE-TAS method captures the correlations in time domain at fixed momentum p and as function of spin-echo time τ (see next section), we Fourier transform the theoretical data to the time domain, yielding the intermediate scattering function $I(p, \tau)$. Then, its envelop is compared to the experimental data of the echo amplitude $P(\tau)$.
Due to the high resolution of the theoretical spectral function, the numerical Fourier transformation provides highly accurate data for the time range measured in experiment. Fig. 6.5 shows a comparison of the experimental data points for the echo amplitude $P(\tau)$ with the theoretical results of the Brückner theory and exponential fits of the form $P(\tau) = 0.5 \cdot \exp(-\gamma\tau)$. Four different temperature sets were measured to investigate the temperature dependence of the spin-echo signal and thus the temporal correlations of the excitation. Taking the equal distribution of non-spin flip and spin flip scattering into account the theoretical curves were normalized to $P(\tau = 0) = 0.5$.
For $T = 0.5$K, close to the zero temperature limit, the excitation is still long-lived and

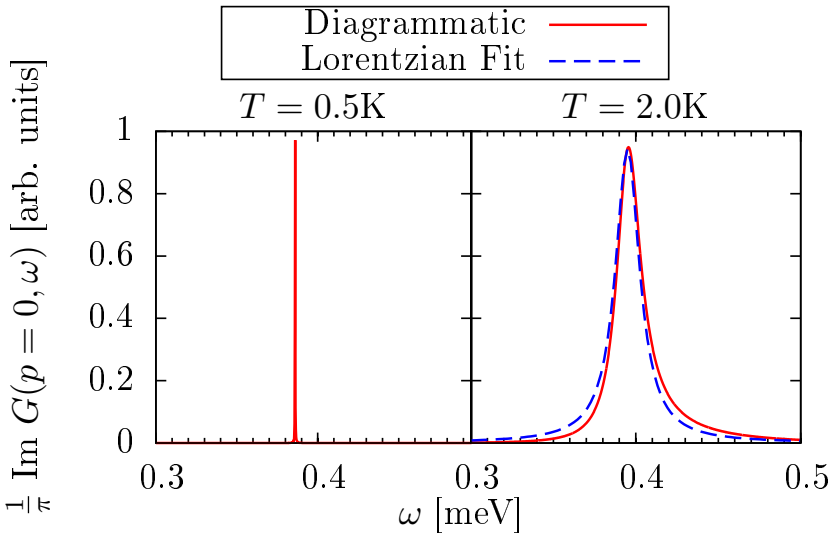

Figure 6.4: Single particle spectral function Im $G(p = 0, \omega)$ for the AHC as function of ω for $T = 0.5$K and $T = 2$K. The full red line is the result from the diagrammatic Brückner approach, while the blue dashed line shows a comparison to a pure Lorentzian line shape. The y-axis has been scaled to make the plots comparable.

shows no decay in coherence up to 112 ps corresponding to a minimal energy resolution of $\hbar/(112\,\text{ps}) \approx 5\,\mu\text{eV}$. As temperature increases, the echo amplitude shows a faster decay due to additional scattering processes and the experimental data points show a good agreement with the theoretical results up to $T = 3\text{K} \approx 0.67\Delta/k_\text{b}$. We stress that the theory has no free parameters and matches to the experiment without any fitting at all. The pure exponential fits, however, are based on four fit parameters γ, one for each temperature. They agree slightly better than the parameter free Brückner theory. Hence the process responsible for the decay can not be determined purely from the polarization.

The deeper reason for the decay lies in the imaginary part of the self-energy. Since the self-energy is determined by the effective interaction Γ, non-trivial scattering processes lead to the specific form of the decay in time domain. It is a consequence of the hard-core bosonic nature of the excitations.

Note, that the theoretical prediction of the Brückner approach shows a vanishing slope for $P(\tau = 0)$. This is expected in a full quantum mechanical description, where the decay channel has only a finite support in frequency. Due to the finite minimal correlation time $\tau_\text{min} \approx 14.5$ps, which is measurable, this feature is hardly examinable in the experiment.

Since the polarization, is not sufficient to distinguish between a simple statistical model and the results of the Brückner theory, we pass to another quantity which is accessible to theory and experiment: the intensity of the mode. The intensity of the mode is directly connected to the quasi-particle residue. In a statistical description of the decay, the quasi-particle residue is independent of temperature and stays constant [19, 29].

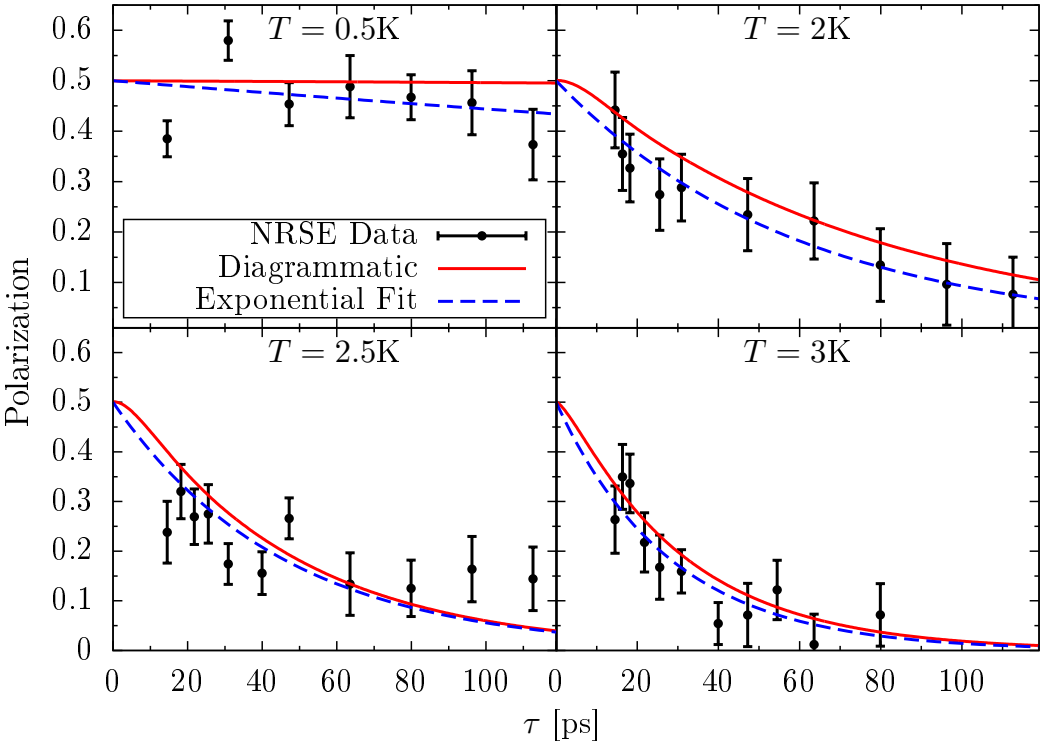

Figure 6.5: Echo amplitude as function of the spin-echo time τ for four different temperatures T. The dots are the experimental data points obtained from the NRSE-TAS measurements, full red lines indicate the theory curve from the Brückner-approach. The blue dashed lines are exponential fits of the form $P(\tau) = 0.5 \cdot \exp(-\gamma\tau)$. The fit parameters for the different temperatures are $T = 0.5\text{K} : \gamma = 0.00119\text{ps}^{-1}$, $T = 2.0\text{K} : \gamma = 0.01681\text{ps}^{-1}$, $T = 2.5\text{K} : \gamma = 0.02193\text{ps}^{-1}$ and $T = 3.0\text{K} : \gamma = 0.03559\text{ps}^{-1}$.

The Brückner theory predicts a strong dependence of the total intensity on temperature. The more hard-core bosons are thermally excited in the system, the more difficult it is to add further bosons by neutron scattering. Thus the residue decreases significantly upon increasing temperature, see Eq. (9) in Ref. [85].

Figure. 6.6 shows a comparison between the intensity measured by NRSE-TAS and the theoretical prediction. The experimental data are normalized to the low temperature regime at $T = 0.5\text{K}$.

The agreement between the Brückner theory and experiment is remarkable. The slight deviation at $T = 3\text{K}$ is in agreement with the low-temperature expansion applied in the Brückner approach. As before, the theoretical prediction of the Brückner approach results purely from the full quantum model in Eq. (6.1) and has no free parameters. In contrast, the purely statistical model fails to explain the temperature dependence of the intensity. Note, that the decreasing intensity results from the hard-core bosonic commutator relation and is not related to the temperature dependence in the fluctuation-dissipation theorem in Eq. (2.4).

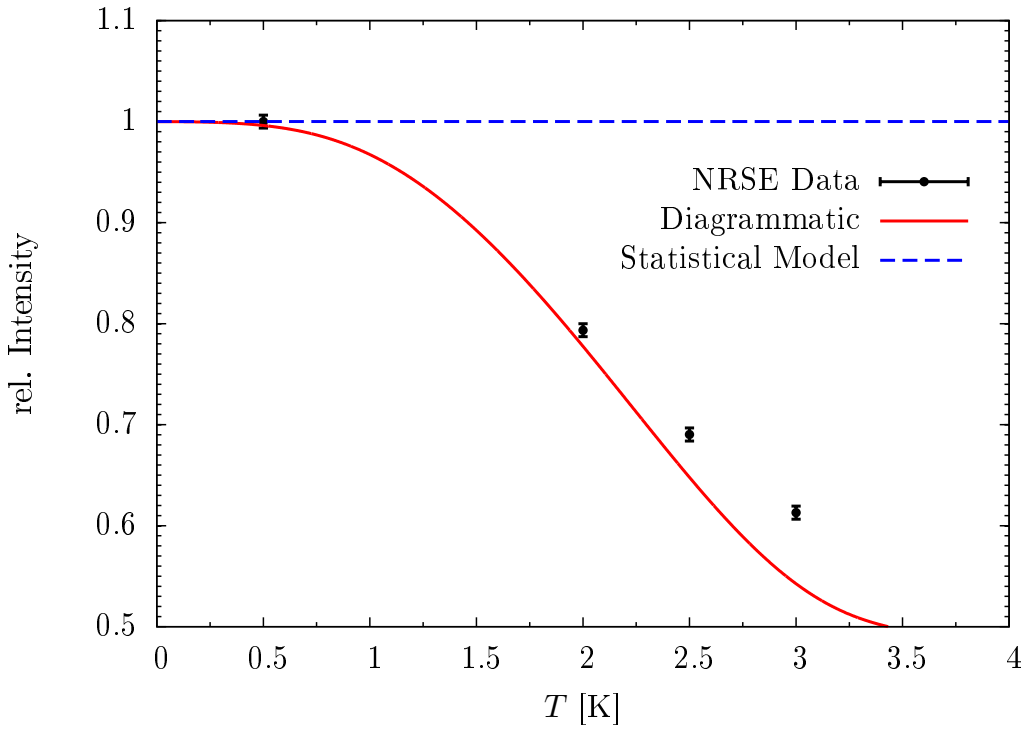

Figure 6.6: Comparison between the experimentally obtained intensity (black data points) with the prediction from the diagrammatic Brückner approach (full red line) and the constant intensity in the statistical model (blue dashed line). The experimental data were normalized to the base temperature value and are in agreement with the Brückner theory except that the experiment shows a slightly slower decay in intensity.

6.4 Conclusion

In this chapter we used the diagrammatic Brückner approach to obtain a theoretical prediction of the single particle dynamics of $Cu(NO_3)_2 \cdot 2.5\ D_2O$ in the time domain. Very good agreement between theory and experiment has been achieved without any extensive data analysis or variation of parameters. On basis of the polarization and intensity of the mode it was argued, that the single particle decoherence cannot be described by a purely statistical model, but rather by non-trivial scattering processes of the hard-core bosonic excitations. Thus the direct analysis in the time domain is a promising route to understand dynamic correlations and to deepen our understanding of quantum coherence at finite temperature. An interesting question is, whether it is possible to increase the fraction of non-trivial scattering processes and therefore the asymmetry in frequency domain to further enhance the quantum character of the excitations at finite temperature.

7 Complete diagrammatic treatment of additional interactions

In this chapter we will extend the Brückner approach to include also additional interactions besides the hard-core constraint correctly up to order $\exp(-\beta\Delta)$. In contrast to the mean-field approach applied before, all ladder diagrams are calculated for the full two particle interactions.
We start with some preliminary considerations in section 7.1. Next we will introduce a matrix valued equivalent of the Bethe-Salpeter equation, taking the hard-core constraint and the additional interactions into account simultaneously, in section 7.2. Due to the new scattering processes, the contributions from the anti-bound state will be modified. For didactic reasons we will explain the key ideas for the one dimensional single flavor case. Then a high level algorithm is sketched on how to implement the equation in section 7.3. To evaluate the approach in section 7.4, we will test it on the additional interactions of the dimerized Heisenberg ladder and chain. Finally we will conclude in section 7.5.

7.1 Preliminary considerations

In its most general form, the two-body interaction of two hard-core bosons with a single flavor in one dimension can be described by

$$V = \frac{1}{2}\sum_{j}\sum_{d_1,d_2,d_3} V(d_1,d_2,d_3) b_j^\dagger b_{j+d_1}^\dagger b_{j+d_2} b_{j+d_2+d_3}. \tag{7.1}$$

Where $d_1, d_2, d_3 \in \mathbb{Z}$ and $d_1 \neq 0$ and $d_3 \neq 0$ holds due to the hard-core constraint.

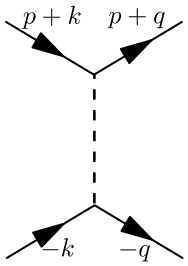

Figure 7.1: Diagrammatic representation of Eq. (7.6)

Since we want to apply momentum dependent diagrammatic perturbation theory, we transform the interaction in to reciprocal space

$$V = \frac{1}{2N^2} \sum_{q_1,q_2,q_3,q_4} \sum_{j} \sum_{d_1,d_2,d_3} V(d_1,d_2,d_3) b^\dagger_{q_1} b^\dagger_{q_2} b_{q_3} b_{q_4} e^{ij(q_1+q_2-q_3-q_4)} e^{id_1q_2} e^{-id_2q_3} e^{-i(d_2+d_3)q_4} \tag{7.2a}$$

$$= \frac{1}{2N} \sum_{q_2,q_3,q_4} \sum_{d_1,d_2,d_3} V(d_1,d_2,d_3) b^\dagger_{q_3+q_4-q_2} b^\dagger_{q_2} b_{q_3} b_{q_4} e^{id_1q_2} e^{-id_2q_3} e^{-i(d_2+d_3)q_4}. \tag{7.2b}$$

Hermiticity implies that the matrix entries can be choosen such, that

$$V(d_1,d_2,d_3) \stackrel{!}{=} V^*(d_3,-d_2,d_1) \tag{7.3}$$

is fulfilled. Further we introduce the total momentum p and the relative momenta k and q, by applying the transformations

$$q_3 + q_4 = p \quad , \quad q_2 = -q \quad , \quad q_4 = -k \tag{7.4}$$

to the momentum indices

$$V = \frac{1}{2N} \sum_{p,k,q} \sum_{d_1,d_2,d_3} V(d_1,d_2,d_3) b^\dagger_{p+q} b^\dagger_{-q} b_{p+k} b_{-k} e^{-id_1q} e^{-id_2(p+k)} e^{i(d_2+d_3)k} \tag{7.5a}$$

$$= \frac{1}{2N} \sum_{p,k,q} \sum_{d_1,d_2,d_3} V(d_1,d_2,d_3) b^\dagger_{p+q} b^\dagger_{-q} b_{p+k} b_{-k} e^{-id_2p} e^{-id_1q} e^{id_3k} \tag{7.5b}$$

Now it is possible to read off the interaction vertex, including the hard-core interaction, see Eq. (2.12),

$$V(p,k,q) = \frac{U}{N} + \frac{1}{N} \sum_{d_1,d_2,d_3} V(d_1,d_2,d_3) e^{-id_2p} e^{-id_1q} e^{id_3k}. \tag{7.6}$$

We introduce a diagrammatic representation for the new interaction vertex in Fig. 7.1.

7.2 Matrix valued Brückner approach

In order to include the additional interaction into the Brückner approach, we need to calculate the ladder diagrams with the full interaction given in Fig. 7.2. Note the additional dependence on k and q of the interaction vertex. We proceed by defining the momentum dependent vectors

$$\mathbf{f}(q) = \begin{pmatrix} 1 \\ e^{-iq} \\ e^{iq} \\ e^{-2iq} \\ e^{2iq} \\ \vdots \end{pmatrix} \quad \Rightarrow \mathbf{f}^\dagger(k) = \begin{pmatrix} 1 & e^{ik} & e^{-ik} & e^{i2k} & e^{-2ik} & \cdots \end{pmatrix} \tag{7.7}$$

Thus we can rewrite the interaction vertex as a bilinear form

$$V(p,k,q) = \frac{1}{N}\mathbf{f}^\dagger(k)\underline{\underline{\Gamma}}_0(p)\mathbf{f}(q), \tag{7.8}$$

where the dependencies on the momenta p, k, q have been factorized. The first few entries of the matrix $\underline{\underline{\Gamma}}_0(p)$ are given by

$$\underline{\underline{\Gamma}}_0(p) = \begin{pmatrix} U & 0 & 0 & \cdots \\ 0 & \sum\limits_{d_2} V(1,d_2,1)e^{-id_2p} & \sum\limits_{d_2} V(1,d_2,-1)e^{-id_2p} & \cdots \\ 0 & \sum\limits_{d_2} V(-1,d_2,1)e^{-id_2p} & \sum\limits_{d_2} V(-1,d_2,-1)e^{-id_2p} & \cdots \\ \vdots & \vdots & \vdots & \ddots \end{pmatrix} \tag{7.9a}$$

$$=: \underbrace{\begin{pmatrix} U & 0 & \cdots \\ 0 & 0 & \cdots \\ \vdots & \vdots & \ddots \end{pmatrix}}_{\underline{\underline{U}}} + \underline{\underline{V}} \tag{7.9b}$$

where we introduced the commutating matrices $\underline{\underline{U}}$ and $\underline{\underline{V}}$. Without any additional interaction, $\underline{\underline{V}}$ vanishes and the problem would be scalar as in chapter 2.
Using Eq. (7.3), it is easy to show, that the matrix entries of $\underline{\underline{V}}$ are Hermitian

$$\left(\sum_{d_2} V(d_1,d_2,d_3)e^{-id_2p}\right)^* = \sum_{d_2} V^*(d_1,d_2,d_3)e^{id_2p} \tag{7.10a}$$

$$\overset{(7.3)}{=} \sum_{d_2} V(d_3,-d_2,d_1)e^{id_2p} \tag{7.10b}$$

$$\overset{d_2\to -d_2}{=} \sum_{d_2} V(d_3,d_2,d_1)e^{-id_2p}. \tag{7.10c}$$

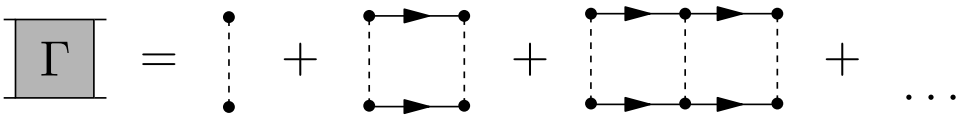

Figure 7.2: Ladder diagrams with the interaction vertex given in Eq. (7.6).

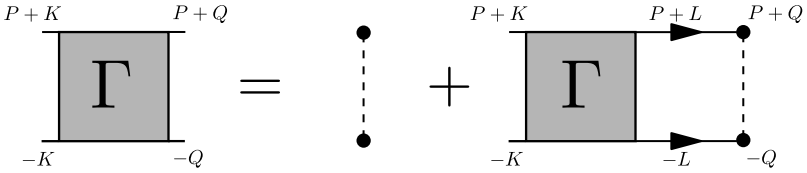

Figure 7.3: Bethe-Salpeter equation for the ladder diagrams in Fig. 7.2.

Next we want to calculate the ladder diagrams by solving the Bethe-Salpeter equation for the full interaction, given in Fig. 7.3,

$$\Gamma(P,K,Q) = \frac{V(p,k,q)}{\beta} - \frac{1}{\beta}\sum_L \Gamma(P,K,L)G(P+L)G(-L)V(p,l,q). \tag{7.11}$$

In contrast to the scalar case, the scattering amplitude Γ now also depends on the relative momenta K and Q, complicating the integration. Since the elementary interaction vertex factorizes the momenta, it is logical to apply the same Ansatz for the scattering amplitude,

$$\Gamma(P,K,Q) = \frac{1}{N}\mathbf{f}^\dagger(k)\underline{\underline{\Gamma}}(P)\mathbf{f}(q). \tag{7.12}$$

Inserting Eqs. (7.8) and (7.12) into Eq. (7.11) yields

$$\begin{aligned}\frac{1}{N}\mathbf{f}^\dagger(k)\underline{\underline{\Gamma}}(P)\mathbf{f}(q) = \frac{1}{N}\mathbf{f}^\dagger(k)\underline{\underline{\Gamma}}_0(p)\mathbf{f}(q) \\ - \frac{1}{N^2\beta}\sum_L \mathbf{f}^\dagger(k)\underline{\underline{\Gamma}}(P)\mathbf{f}(l)G(P+L)G(-L)\mathbf{f}^\dagger(l)\underline{\underline{\Gamma}}_0(p)\mathbf{f}(q).\end{aligned} \tag{7.13}$$

Note, that Eq. (7.13) is a bilinear form. The equality must hold for all k and q, hence we can separate the dependence on the relative momenta

$$\underline{\underline{\Gamma}}(P) = \underline{\underline{\Gamma}}_0(p) - \frac{1}{N\beta}\sum_L \underline{\underline{\Gamma}}(P)G(P+L)G(-L)\mathbf{f}(l)\mathbf{f}^\dagger(l)\underline{\underline{\Gamma}}_0(p). \tag{7.14}$$

We call $\underline{\underline{\Gamma}}(P)$ the scattering matrix in the following. It takes the role of the scattering amplitude $\Gamma(P)$ in the scalar case. Additionally we introduce the matrix

$$\underline{\underline{N}}(P) := \frac{1}{N}\sum_l \mathbf{f}(l)\mathbf{f}^\dagger(l)M(P,l), \tag{7.15}$$

with

$$M(P,l) := \frac{1}{\beta}\sum_{i\omega_l} G(P+L)G(-L). \tag{7.16}$$

The Matrix $\underline{\underline{N}}(P)$ has a spectral representation, which we denote with $\underline{\underline{\rho_p}}(\omega)$. It can be obtained by computing its imaginary part. Inserting the previous definitions into the Bethe-Salpeter equation yields a simplified expression for the scattering matrix

$$\underline{\underline{\Gamma}}(P) = \underline{\underline{\Gamma}}_0(p) - \underline{\underline{\Gamma}}(P)\underline{\underline{N}}(P)\underline{\underline{\Gamma}}_0(p). \tag{7.17}$$

Using the previous equations we can calculate the scattering matrix

$$\underline{\underline{\Gamma}}(P) = \underline{\underline{\Gamma}}_0(p)\left(\mathbb{I} + \underline{\underline{N}}(P)\underline{\underline{\Gamma}}_0(p)\right)^{-1} \tag{7.18a}$$

$$= \left(\left[\mathbb{I} + \underline{\underline{N}}(P)\underline{\underline{\Gamma}}_0(p)\right]\underline{\underline{\Gamma}}_0^{-1}(p)\right)^{-1} \tag{7.18b}$$

$$= \left(\underline{\underline{\Gamma}}_0^{-1}(p) + \underline{\underline{N}}(P)\right)^{-1}. \tag{7.18c}$$

Since $\mathbf{f}(l)\mathbf{f}^\dagger(l)$ is a dyadic product, it represents a hermitian matrix. The corresponding matrix elements read

$$\mathbf{f}(l)\mathbf{f}^\dagger(l) = \begin{pmatrix} 1 & e^{il} & e^{-il} & e^{2il} & e^{-2il} & \cdots \\ e^{-il} & 1 & e^{-2il} & e^{il} & e^{-3il} & \cdots \\ e^{il} & e^{2il} & 1 & e^{3il} & e^{-il} & \cdots \\ e^{-2il} & e^{-il} & e^{-3il} & 1 & e^{-4il} & \cdots \\ e^{2il} & e^{3il} & e^{il} & e^{4il} & 1 & \cdots \\ \vdots & \vdots & \vdots & \vdots & \vdots & \ddots \end{pmatrix}. \tag{7.19}$$

7.2.1 High energy contribution

Due to the additional interaction, the contribution from the high energy bound state changes. For the exact contribution we need to know the position of the pole for $\omega \propto U$. The pole can be obtained from the inverse of Eq. (7.18)

$$\underline{\underline{\Gamma}}(P)^{-1} = \underline{\underline{\Gamma}}_0^{-1}(p) + \underline{\underline{N}}(P). \tag{7.20}$$

Note, that

$$\underline{\underline{\Gamma}}_0^{-1}(p) = \underline{\underline{U}}^{-1} + \underline{\underline{V}}^{-1} \tag{7.21}$$

holds, where the inverse is implied on the Hilbert space the matrices act on, i.e.,

$$\underline{\underline{U}}^{-1} = \begin{pmatrix} \frac{1}{U} & 0 & \cdots \\ 0 & 0 & \cdots \\ \vdots & \vdots & \ddots \end{pmatrix}, \quad \underline{\underline{V}}^{-1} = \begin{pmatrix} 0 & \cdots \\ \vdots & \begin{pmatrix} \sum_{d_2} V(1,d_2,1)e^{-id_2p} & \cdots \\ \vdots & \ddots \end{pmatrix}^{-1} \end{pmatrix}. \tag{7.22}$$

In the following we need the expansion of $\underline{\underline{N}}(P)$ for $\omega \to \infty$ given by

$$\underline{\underline{N}}(P) = \int_{-\infty}^{\infty} \frac{\underline{\underline{\rho_p}}(x)}{i\omega_p - x} \mathrm{d}x = \frac{\underline{\underline{\rho_0}}(p)}{\omega} + \frac{\underline{\underline{\rho_1}}(p)}{\omega^2} + \mathcal{O}\left(\frac{1}{\omega^3}\right), \tag{7.23}$$

where $\underline{\underline{\rho_i}}(p)$ denotes the i'th moment matrix, see also the scalar case in Eq. (2.30). We introduce the parametrization $\omega = \bar{\omega}U$ such that $\bar{\omega} \in \mathcal{O}(1)$. Inserting the expansion of $\underline{\underline{N}}(P)$ into Eq. (7.20) yields

$$\begin{aligned} &\underline{\underline{U}}^{-1} + \underline{\underline{V}}^{-1} + \frac{1}{U\bar{\omega}}\underline{\underline{\rho_0}}(p) + \frac{1}{U^2\bar{\omega}^2}\underline{\underline{\rho_1}}(p) \\ &= \underline{\underline{V}}^{-1} + \frac{1}{U}\underbrace{\left(\frac{1}{\bar{\omega}}\underline{\underline{\rho_0}}(p) + U\underline{\underline{U}}^{-1}\right)}_{X_1} + \frac{1}{U^2}\underbrace{\left(\frac{\underline{\underline{\rho_1}}(p)}{\bar{\omega}^2}\right)}_{X_2}. \end{aligned} \tag{7.24}$$

To determine the correct contribution from the anti-bound state at frequencies $\omega \propto U$, we need to determine the scattering matrix in this energy range. For that purpose we use ordinary matrix perturbation theory in the parameter $1/U$. In this case, the free theory is given by $\underline{\underline{V}}^{-1}$ and the perturbation are the matrices X_1 and X_2 in first and second order respectively. We denote with $\lambda_i, \mathbf{e}_i$ the unperturbed eigenpairs of $\underline{\underline{V}}^{-1}$. The first eigenpair is trivial and reads

$$\lambda_1 = 0\,, \quad \mathbf{e}_1 = \begin{pmatrix} 1 \\ 0 \\ 0 \\ \vdots \end{pmatrix}, \tag{7.25}$$

it is associated with the anti-bound state. However, the eigenpair is mixed with higher order states in the full problem. Hence we are interested in the corrections to the first

eigenpair,

$$\Delta^1\lambda_1 = \mathbf{e}_1^\dagger X_1 \mathbf{e}_1 = \frac{\rho_0^{11}(p)}{\bar{\omega}} + 1 \tag{7.26}$$

$$\Delta^1\mathbf{e}_1 = \sum_{i\neq 1} \underbrace{\frac{\mathbf{e}_i^\dagger X_1 \mathbf{e}_1}{\lambda_i}}_{\frac{\mathbf{e}_i^\dagger \underline{\underline{\rho_0}}(p)\mathbf{e}_1}{\lambda_i\bar{\omega}}} \mathbf{e}_i \tag{7.27}$$

$$\Delta^2\lambda_1 = \sum_{i\neq 1} \underbrace{\frac{\left|\mathbf{e}_i^\dagger X_1 \mathbf{e}_1\right|^2}{\lambda_i}}_{\frac{\left|\mathbf{e}_i^\dagger \underline{\underline{\rho_0}}(p)\mathbf{e}_1\right|^2}{\lambda_i\bar{\omega}^2}} + \underbrace{\mathbf{e}_1^\dagger X_2 \mathbf{e}_1}_{\frac{\rho_1^{11}(p)}{\bar{\omega}^2}} \tag{7.28}$$

Note, that we do not need the second order corrections to the first eigenvector in the following, since it does not contribute in the relevant order. We introduce the abbreviations

$$\frac{\mathbf{e}_i^\dagger \underline{\underline{\rho_0}}(p)\mathbf{e}_1}{\lambda_i} =: w_i(p)\,, \quad \frac{\left|\mathbf{e}_i^\dagger \underline{\underline{\rho_0}}(p)\mathbf{e}_1\right|^2}{\lambda_i} =: v_i(p). \tag{7.29}$$

To find the pole of the anti-bound state the matrix $\underline{\underline{\Gamma}}(P)$ must be singular for high energies, i.e. the first eigenvalue must vanish as function of $\bar{\omega}$,

$$0 \stackrel{!}{=} \lambda_1 + \frac{1}{U}\Delta^1\lambda_1 + \frac{1}{U^2}\Delta^2\lambda_2 \tag{7.30a}$$

$$0 = \frac{\rho_0^{11}(p)}{\bar{\omega}} + 1 + \frac{1}{U}\sum_{i\neq 1} v_i(p)\frac{1}{\bar{\omega}^2} + \frac{1}{U}\frac{\rho_1^{11}(p)}{\bar{\omega}^2} \tag{7.30b}$$

$$\Rightarrow \bar{\omega} = -\rho_0^{11} + \frac{1}{U}\left(\sum_{i\neq 1}\frac{v_i(p)}{\rho_0^{11}(p)} + \frac{\rho_1^{11}(p)}{\rho_0^{11}(p)}\right) + \mathcal{O}\left(\frac{1}{U^2}\right) \tag{7.30c}$$

So that the pole is given at

$$\omega_U(p) = U\bar{\omega} = -U\rho_0^{11}(p) + \left(\sum_{i\neq 1}\frac{v_i(p)}{\rho_0^{11}(p)} + \frac{\rho_1^{11}(p)}{\rho_0^{11}(p)}\right) + \mathcal{O}\left(\frac{1}{U^1}\right) \tag{7.31}$$

Using a taylor expansion for $\lambda_1(\omega)$ at $\omega = \omega_U$ we can approximate the eigenvalue by

$$\lambda_1(\omega) \approx (\omega - \omega_U(p))\,\frac{-1}{U^2\rho_0^{11}(p)} \tag{7.32}$$

To obtain an effective matrix at high energies the correction to the eigenvector must be taken into account as well

$$\mathbf{e}_1' = \mathbf{e}_1 + \frac{1}{U\bar{w}}\Delta^1\mathbf{e}_1 = \mathbf{e}_1 - \frac{1}{U}\sum_{i\neq 1}\frac{w_i(p)}{\rho_0^{11}(p)}\mathbf{e}_i. \tag{7.33}$$

Thus we can approximate the scattering matrix for large energy

$$\left(\underline{\underline{\Gamma}}_0^{-1} + \underline{\underline{N}}(P)\right)^{-1} \approx \frac{-U^2\rho_0^{11}(p)}{(\omega - \omega_U(p))}\mathbf{e}_1'(p)\mathbf{e}_1'^{\dagger}(p) \tag{7.34a}$$

$$= \frac{-U^2\rho_0^{11}(p)}{(\omega - \omega_U(p))}\left(\mathbf{e}_1\mathbf{e}_1^{\dagger} - \frac{1}{U}\left(\mathbf{e}_1\sum_{i\neq 1}\frac{w_i^*(p)}{\rho_0^{11}(p)}\mathbf{e}_i^{\dagger} + \sum_{i\neq 1}\mathbf{e}_i\frac{w_i(p)}{\rho_0^{11}(p)}\mathbf{e}_1^{\dagger}\right)\right.$$

$$\left. + \mathcal{O}\left(\frac{1}{U^2}\right)\right) \tag{7.34b}$$

To obtain the correct scalar contribution to the self-energy, we need to calculate the bilinear form in Eq. (7.12). To shorten the notation, we first introduce

$$f_i(q) = \mathbf{e}_i^{\dagger}\mathbf{f}(q). \tag{7.35}$$

Next we compute the imaginary part of the scattering function for large energy up to order $1/U$

$$\frac{-1}{\pi}\mathrm{Im}\lim_{i\omega_p\to\omega+i0+}\frac{1}{N}\mathbf{f}^{\dagger}(k)\underline{\underline{\Gamma}}(P)\mathbf{f}(q) = \frac{-U^2\rho_0^{11}(p)}{N\beta}\delta\left(\omega - \omega_U(p)\right)$$

$$\cdot\left[1 - \frac{1}{U}\sum_{j\neq 1}\frac{1}{\rho_0^{11}(p)}\left(w_j^*(p)f_j(q) + w_j(p)f_j(k)^*\right)\right]. \tag{7.36}$$

The self-energy contribution from the anti-bound state at high energy (he) is given by the Hartree and the Fock contributions,

$$\Sigma_{\mathrm{he}}(P) = \sum_K G(K)\Gamma(P+K,-P,-P) + \sum_K G(K)\Gamma(P+K,-K,-P). \tag{7.37}$$

The Matsubara summation is similar to the one found in appendix B.2. Inserting the expression for the effective interaction yields for the Hartree contribution,

$$\Sigma_{\mathrm{he,Hartree}}(P) =$$

$$-\frac{1}{N}\sum_k\int_{-\infty}^{\infty}\mathrm{d}x'\frac{A_k(x')U^2\rho_0^{11}(p+k)\left[1 - \frac{1}{U}\sum\limits_{j\neq 1}\frac{1}{\rho_0^{11}(p+k)}2\mathrm{Re}\left(w_j(p+k)^*f_j(-p)\right)\right]}{i\omega_p - (\omega_U(p+k) - x')}\frac{1}{e^{\beta x'}-1}. \tag{7.38}$$

The expansion of the fraction in $1/U$ reads

$$\frac{U^2\rho_0^{11}(p+k)}{i\omega_p - (\omega_U(p+k) - x')} = U - \frac{i\omega_p - \frac{\sum\limits_{i\neq 1}v_i(p+k)}{\rho_0^{11}(p+k)} - \frac{\rho_1^{11}(p+k)}{\rho_0^{11}(p+k)} + x'}{\rho_0^{11}(p+k)} + \mathcal{O}\left(\frac{1}{U}\right). \tag{7.39}$$

The first term compensates for the Hartree term $\Sigma_{\text{Hartree},U}$ of the pure hard-core interaction (see also Eq. (2.39) in chapter 2),

$$\Sigma_{\text{he,Hartree}}(P) + \Sigma_{\text{Hartree},U} = -\frac{1}{N}\sum_k \int_{-\infty}^{\infty} \mathrm{d}x' A_k(x') \left[\frac{-i\omega_p}{\rho_0^{11}(p+k)} - \frac{\sum_{i\neq 1} v_i(p+k)}{{\rho_0^{11}}^2(p+k)} \right. \\ \left. - \frac{\rho_1^{11}(p+k)}{{\rho_0^{11}}^2(p+k)} + \frac{x'}{\rho_0^{11}(p+k)} - \sum_{j\neq 1} \frac{1}{\rho_0^{11}(p+k)} 2\mathrm{Re}\left(w_j(p+k)^* f_j(-p)\right) \right] \frac{1}{e^{\beta x'}-1} \tag{7.40}$$

The Fock term can be computed in a similar fashion, yielding

$$\Sigma_{\text{he,Fock}}(P) = \frac{1}{N\beta}\sum_{k,i\omega_k} \int_{-\infty}^{\infty}\int_{-\infty}^{\infty} \mathrm{d}x\mathrm{d}x' \frac{A_k(x')}{i\omega_k - x'} \frac{U^2 \rho_0^{11}(p+k)\delta\left(x - \omega_U(p+k)\right)}{i\omega_p + i\omega_k - x} \\ \cdot \left[1 - \frac{1}{U}\sum_{j\neq 1} \frac{1}{\rho_0^{11}(p+k)} \left(w_j(p+k)^* f_j(-p) + w_j(p+k) f_j(-k)^* \right) \right]. \tag{7.41}$$

Applying the same expansion in $1/U$ and calculating the Matsubara summation yields

$$\Sigma_{\text{he,Fock}}(P) + \Sigma_{\text{Fock},U} = -\frac{1}{N}\sum_k \int_{-\infty}^{\infty} \mathrm{d}x' \frac{A_k(x')}{e^{\beta x'}-1} \left[\frac{-i\omega_p}{\rho_0^{11}(p+k)} - \frac{\sum_{i\neq 1} v_i(p+k)}{{\rho_0^{11}}^2(p+k)} \right. \\ \left. - \frac{\rho_1^{11}(p+k)}{{\rho_0^{11}}^2(p+k)} + \frac{x'}{\rho_0^{11}(p+k)} - \sum_{j\neq 1} \frac{1}{\rho_0^{11}(p+k)} \left(w_j(p+k)^* f_j(-p) + w_j(p+k) f_j(-k)^* \right) \right]. \tag{7.42}$$

Comparing this results to the scalar case in Eq. (2.40a), we see, that two new contributions to the real part of the self-energy arise due to the additional interactions.

7.2.2 Hartree-Fock contribution for additional interactions

The pure Hartree-Fock contribution for the additional interaction is not included in the spectral representation of $\Gamma(P)$, hence it has to be calculated separately. The pure Hartree-Term reads

$$\Sigma_{\text{Hartree},V} = -\frac{1}{N}\sum_k \int_{-\infty}^{\infty} \mathrm{d}x' A_k(x') \frac{1}{e^{\beta x'}-1} \mathbf{f}^\dagger(-p) \underline{\underline{V}}(p+k) \mathbf{f}(-p). \tag{7.43}$$

The Fock term for the additional interaction is given by

$$\Sigma_{\text{Fock},V} = -\frac{1}{N}\sum_k \int_{-\infty}^{\infty} \mathrm{d}x' A_k(x') \frac{1}{e^{\beta x'}-1} \mathbf{f}^\dagger(-k) \underline{\underline{V}}(p+k) \mathbf{f}(-p). \tag{7.44}$$

In the single flavor case, both diagrams have a prefactor of 1.

7.2.3 Low energy contribution

In the low energy sector we can take the limit $U \to \infty$. The matrix $\underline{\underline{\Gamma_0}}^{-1}$ is then directly given by $\underline{\underline{V}}^{-1}$. We use the Hilbert representation of $\underline{\underline{N}}$ to calculate the Hilbert representation of $\underline{\underline{\Gamma}}(P) - \underline{\underline{V}}(p)$, i.e. the ladder diagrams minus the Hartree-Fock diagrams,

$$\begin{aligned} \underline{\underline{\Gamma}}(P) - \underline{\underline{V}}(p) &= \int_{-\infty}^{\infty} \mathrm{d}x' \frac{\underline{\underline{\underline{\underline{\rho_\Gamma}}}}(p, x')}{i\omega_p - x'}, \\ \underline{\underline{\underline{\underline{\rho_\Gamma}}}}(p, \omega) &= \begin{pmatrix} \rho_\Gamma^{11} & \rho_\Gamma^{12} & \cdots \\ \rho_\Gamma^{21} & \rho_\Gamma^{22} & \cdots \\ \vdots & \vdots & \ddots \end{pmatrix} = \frac{-1}{\pi} \mathrm{Im} \lim_{i\omega_p \to \omega + i0+} \left(\underline{\underline{V}}^{-1} + \underline{\underline{N}}(P) \right)^{-1} - \underline{\underline{V}}. \end{aligned} \tag{7.45}$$

Technically the spectral matrix $\underline{\underline{\underline{\underline{\rho_\Gamma}}}}(p, \omega)$ is obtained by first inverting the matrix $(\underline{\underline{V}}^{-1} + \underline{\underline{N}}(P))$ point wise for every ω and p numerically and then taking the imaginary part. Next we determine the low energy (le) contributions to the self-energy. Similar to the high energy case, they contain two kinds of contributions: the Hartree- and the Fock-like diagrams,

$$\Sigma_{\mathrm{le}}(P) = \sum_K G(K)(\Gamma(P+K, -P, -P) + \Gamma(P+K, -K, -P)) \tag{7.46a}$$

$$= \frac{-1}{N\beta} \sum_{k, i\omega_k} \int_{-\infty}^{\infty} \int_{-\infty}^{\infty} \mathrm{d}x' \mathrm{d}x'' \frac{A_k(x')}{i\omega_k - x'} \left(\mathbf{f}^\dagger(-p) + \mathbf{f}^\dagger(-k) \right) \frac{\underline{\underline{\underline{\underline{\rho_\Gamma}}}}(p+k, x'')}{i\omega_p + i\omega_k - x''} \mathbf{f}\,(-p)\,. \tag{7.46b}$$

Summing over all Matsubara frequencies and substituting $k \to k - p$ leads to

$$\begin{aligned} \Sigma_{\mathrm{le}}(P) = \frac{1}{N} \sum_k \int_{-\infty}^{\infty} \mathrm{d}x'' \left[\mathbf{f}^\dagger\,(-p) + \mathbf{f}^\dagger\,(-(k-p)) \right] A_{k-p}(x'' - \omega) \underline{\underline{\underline{\underline{\rho_\Gamma}}}}(k, x'') \mathbf{f}\,(-p) \\ \cdot \left[\frac{1}{e^{\beta(x''-\omega)} - 1} - \frac{1}{e^{\beta x''} - 1} \right]. \end{aligned} \tag{7.47}$$

Now we can sum all contributions to the self-energy in leading order of $\exp(-\beta\Delta)$

$$\Sigma = \Sigma_{\mathrm{le}} + \Sigma_{\mathrm{Fock},V} + \Sigma_{\mathrm{Hartree},V} + \Sigma_{\mathrm{he,Fock}} + \Sigma_{\mathrm{Fock},U} + \Sigma_{\mathrm{he,Hartree}} + \Sigma_{\mathrm{Hartree},U}. \tag{7.48}$$

We omitted the dependency on total momentum P for the sake of brevity.

7.3 Implementation

The implementation of the Brückner approach including additional interactions is similar to the case without additional interaction, but requires more memory due to the matrix form of the equations. To speed up the computation, FFT algorithms can be used, wherever a convolution is required. A high level algorithm that computes the self-energy is outlined in the following.

The input parameters are given by

- Initial form of $A(p, \omega)$
- Dispersion $\omega(p)$
- Interaction matrix $V(d_1, d_2, d_3)$

First step: Calculate the contribution of the anti-bound state

- Calculate matrix $\underline{\underline{\rho_p}}(\omega)$
- Calculate moment matrices $\underline{\underline{\rho_0}}(p)$ and $\underline{\underline{\rho_1}}(p)$
- Calculate eigenpairs $\mathbf{e}_i$ and λ_i
- Calculate $w_i(p)$ and $v_i(p)$
- Calculate frequency independent contribution to anti-bound state
- Calculate prefactor of frequency dependent term ($\propto i\omega_p$)

Second step: Calculate Hartree-Fock contribution of additional interaction

- Calculate the weight $A_k n_\mathrm{B}$ as function of k and convolve with all matrix elements in $V(p, k, q)$

Third step: Calculate the low energy contribution

- Calculate $\underline{\underline{\rho_\Gamma}}$ as point wise inversion
- Calculate low energy self-energy $\Sigma_\mathrm{le}(P)$ from $\underline{\underline{\rho_\Gamma}}(P)$

Final Step: Calculate new spectral function

- Combine contributions from the anti-bound state, Hartree-Fock diagrams, low energy contribution
- Calculate new spectral function $A(p,\omega)$ from self-energy $\Sigma(p,\omega)$

7.4 Results for the Heisenberg ladder and chain

The dimerized Heisenberg ladder and chain are used in order to test the complete diagrammatic treatment of additional interactions in the following section. The Hamiltonian of the Heisenberg ladder is given by

$$H = \sum_r J_\perp \mathbf{S}_r^{\mathrm{L}} \cdot \mathbf{S}_r^{\mathrm{R}} + J_\parallel \left(\mathbf{S}_r^{\mathrm{R}} \cdot \mathbf{S}_{r+1}^{\mathrm{R}} + \mathbf{S}_r^{\mathrm{L}} \cdot \mathbf{S}_{r+1}^{\mathrm{L}} \right), \tag{7.49}$$

where we assume that $J_\perp$ is the strong bond, defining the dimers and $x = J_\parallel / J_\perp$ is the perturbation parameter. Note, that the index r denotes dimers, and L and R refer to the left and right leg of the ladder respectively. The Hamiltonian is represented in Fig. 7.4. The Hamiltonian of the Heisenberg chain is given in Eq. (6.1), where the equivalent perturbation parameter is given by $x = J'/J$. Similar to the Heisenberg chain, the Heisenberg ladder has triplon excitations. A deepCUT calculation yields an effective Hamiltonian for the hopping and interaction of the triplons.
In order to include the additional interaction, two types of interaction vertices present in both models must be dealt with: (i) ingoing particles have the flavor α and outgoing particles have the flavor β, where $\alpha = \beta$ is possible and (ii) two particles with flavor α and β, with $\alpha \neq \beta$ interact with each other. For the first kind of interaction, Hartree- as well as Fock-like diagrams contribute to the self-energy. The second kind of interaction can only contribute with the Hartree-like diagrams, but the closed loop obtaines a prefactor of 2, since there are two types of possible flavors for the Green functions in the closed loop.
Therefore we define two types of interaction matrices: $\underline{\underline{V}}^{\alpha\alpha}_{\beta\beta}$ for the type (i) interactions and $\underline{\underline{V}}^{\alpha\beta}_{\alpha\beta}$ for the type (ii) interactions.
Since we focus on small parameters x in the ladder and chain model, a finite order in the deepCUT calculation is sufficient. For the Heisenberg ladder, the matrices up to second order can be obtained from table F.2 in the appendix. In our calculations we included the additional interactions correctly up to second order in x for the chain as well as for the ladder.

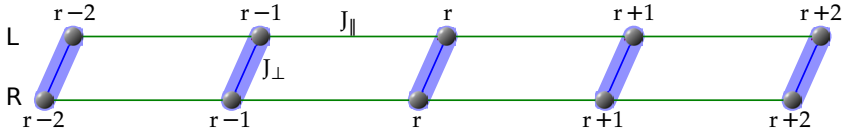

Figure 7.4: Interactions in the Heisenberg ladder.

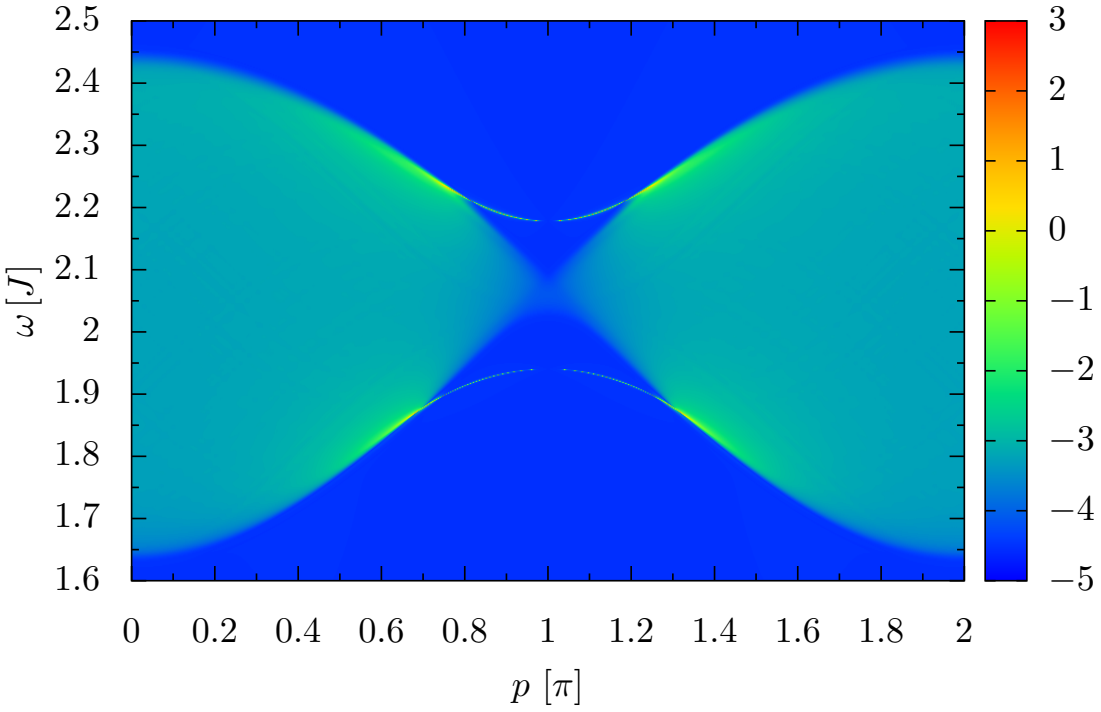

Figure 7.5: Diagonal element of the scattering matrix spectral function $\underline{\underline{\rho_\Gamma^{22}}}$ for the Heisenberg ladder for $x = 0.2$ at $T = 0.3J$ as function of total momentum p and frequency ω. The z axis has a logarithmic scale to account for strong peaks.

Higher order contributions up to order 6 are included if they match the specific operator structure of the first and second order operators.

We have to differentiate between three different types of diagrams. First, Fock-like diagrams have an interaction matrix given by $\underline{\underline{U}} + \underline{\underline{V}}^{\alpha\alpha}_{\beta\beta}$, next the Hartree-like diagrams with the same flavor structure have the same interaction matrix but different momentum sums and third, the Hartree-like diagrams with different flavor in the upper and lower leg have the interaction matrix $\underline{\underline{U}} + \underline{\underline{V}}^{\alpha\beta}_{\alpha\beta}$. The diagrams of the first and second type can be calculated in the same way in the Bethe-Salpter equation but yield different contributions on the level of the self-energy, due to the different momentum summations. For a more detailed overview we refer the reader to appendix F.

The most striking effect of the additional interaction is that it also includes effects of bound and anti-bound states in the low energy sector. This is best observed in the matrix elements of $\underline{\underline{\Gamma}}$. In Fig. 7.5 we show a matrix entry of the spectral function $\underline{\underline{\rho_\Gamma}}^{\alpha\beta}_{\alpha\beta}$ for the Heisenberg ladder. The scattering matrix is dominated by a two-particle continuum with a bound state below the continuum and an anti-bound state above the continuum at $p \approx \pi$. The bound and anti-bound states coincide with $S = 1$ and $S = 2$ excitations in the triplon language [112, 113]. Note, that the $S = 0$ bound state does not show up, because it has no overlapp with the interaction matrix $\underline{\underline{V}}^{\alpha\beta}_{\alpha\beta}$.

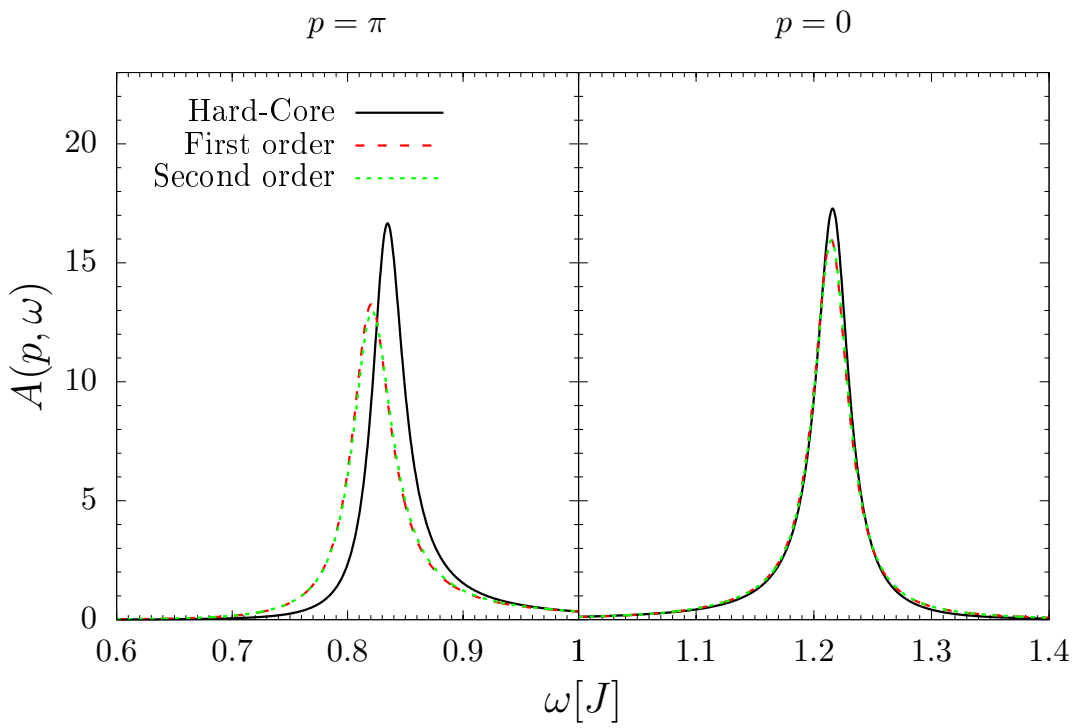

Figure 7.6: Spectral function of the Heisenberg ladder for $x = 0.2$ at momentum $p = \pi$ on the left panel and $p = 0$ on the right panel. The temperature is fixed to $T = 0.3J$. Comparison between the computation with the pure hard-core interaction, additional interactions up to first order and second order in x.

Next we investigate the spectral function $A(p, \omega)$. To compare the effect of the additional interaction to the pure hard-core interaction, we choose the small parameter $x = 0.2$ for both models. In Fig. 7.6 we compare the spectral function of the Heisenberg ladder at $T = 0.3J$ computed for the pure hard-core interaction with the spectral function computed including only the first order interactions and also the second order interactions. The same quantities are depicted for the chain model in Fig. 7.8. Due to the fact, that the interaction between the dimers is weaker in case of the chain model, the bandwidth of the chain model is roughly half the bandwidth of the ladder model.

For the maximum mode at $p = 0$ in the Heisenberg ladder the additional interaction has only a small effect on the spectral function, by decreasing the peak further. The effect is enhanced at the gap mode, where the additional scattering processes also lead to shift of the mode to lower energies. The same holds for the chain model, but here the maximum mode is at $p = \pi$ while the gap mode is at $p = 0$.

A similar effect can be observed upon increasing temperature, although the difference between the first and second order seem to decrease. This is shown in Fig. 7.7 for the ladder and in Fig. 7.9 for the chain, for a temperature of $T = 0.4J$.

This analysis shows, that for a qualitative understanding of the line shape broadening in dimerized models the hard-core scattering provides the major explanation. However for a quantitative analysis of the spectral function, the additional interactions must be taken into account.

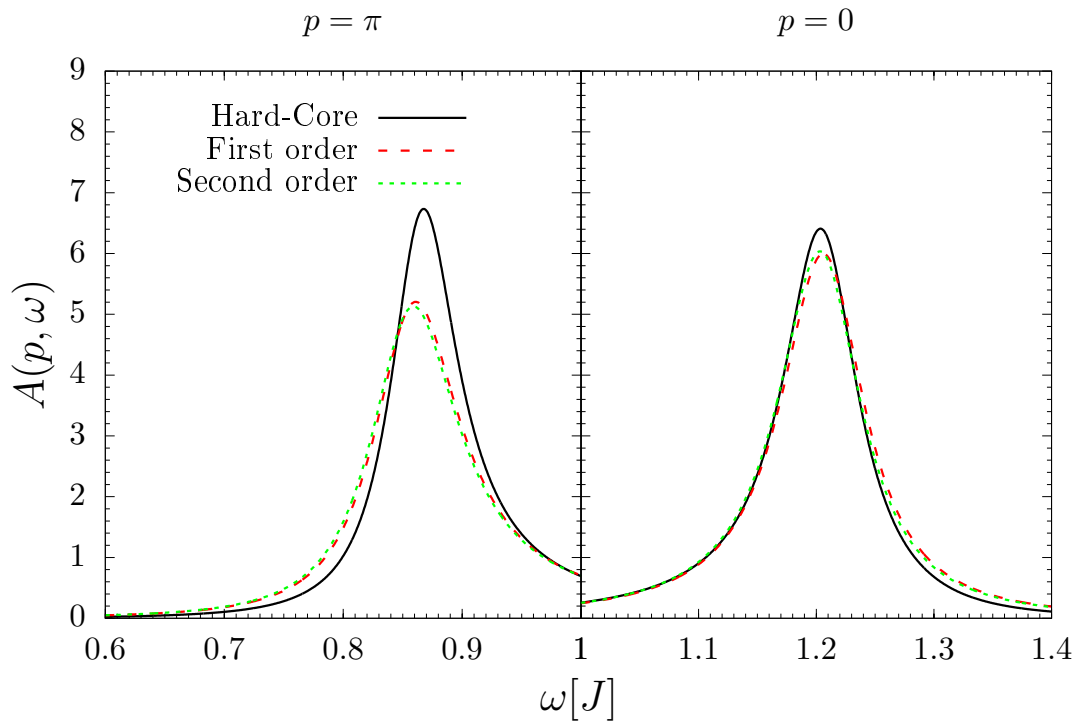

Figure 7.7: Spectral function of the Heisenberg ladder for $x = 0.2$ at momentum $p = \pi$ on the left panel and $p = 0$ on the right panel. The temperature is fixed to $T = 0.4J$. Comparison between the computation with the pure hard-core interaction, additional interactions up to first order and second order in x.

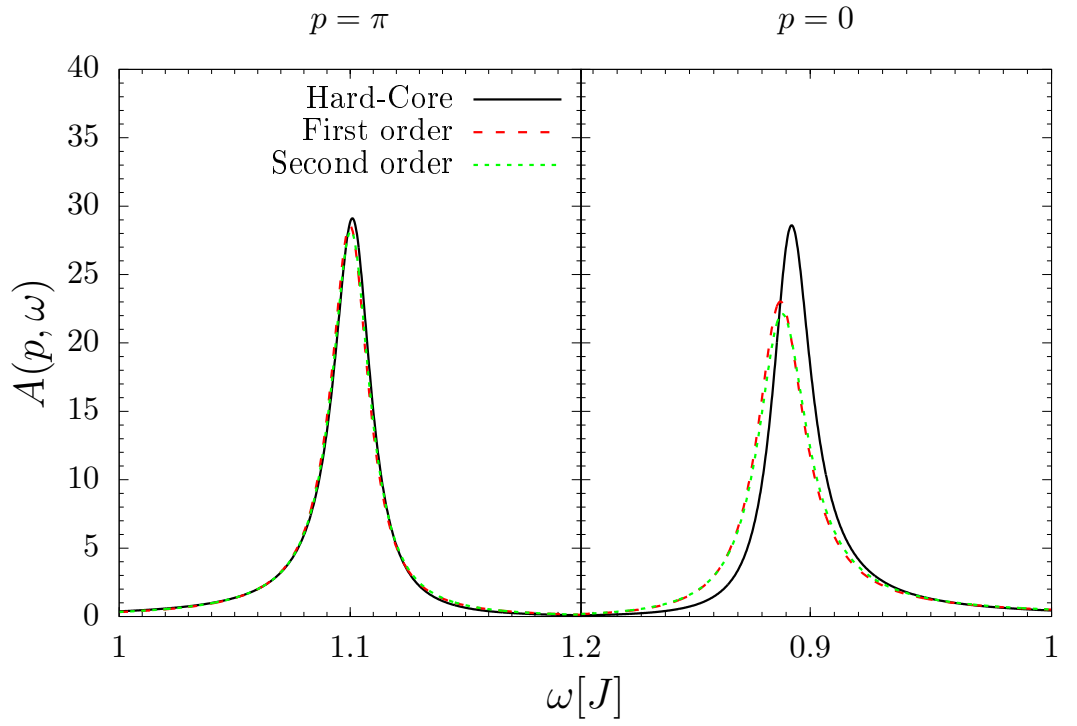

Figure 7.8: Spectral function of the Heisenberg chain for $x = 0.2$ at momentum $p = \pi$ on the left panel and $p = 0$ on the right panel. The temperature is fixed to $T = 0.3J$. Comparison between the computation with the pure hard-core interaction, additional interactions up to first order and second order in x.

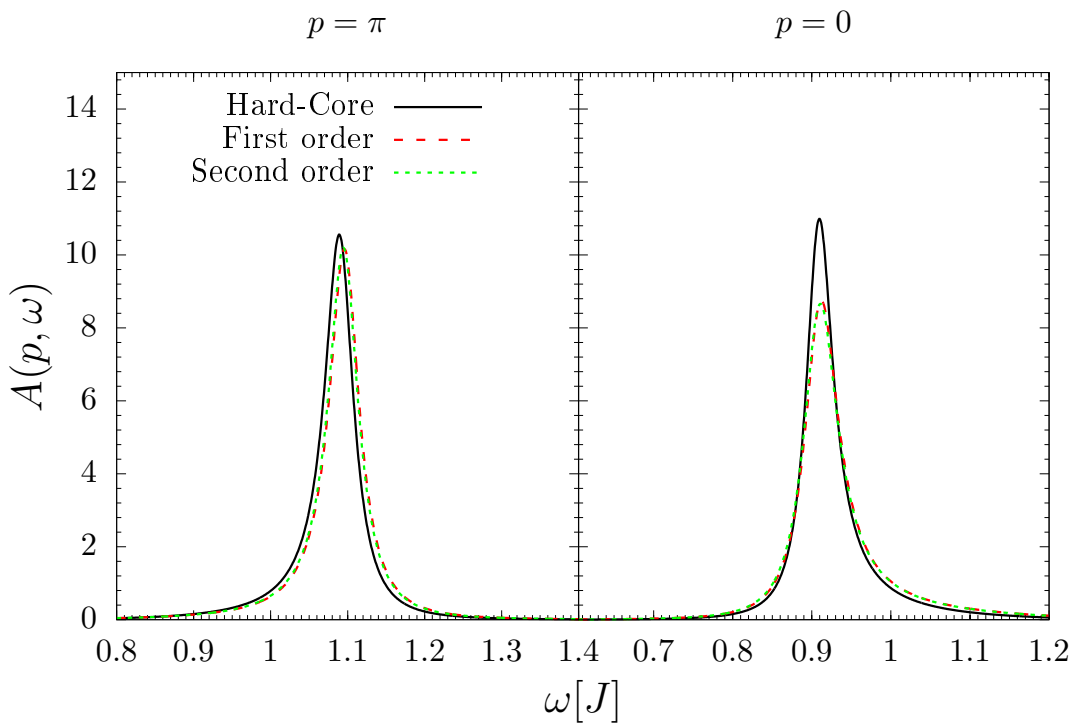

Figure 7.9: Spectral function of the Heisenberg chain for $x = 0.2$ at momentum $p = \pi$ on the left panel and $p = 0$ on the right panel. The temperature is fixed to $T = 0.4J$. Comparison between the computation with the pure hard-core interaction, additional interactions up to first order and second order in x.

7.5 Conclusion

In this chapter we showed, how additional interactions besides the hard-core constraint can be taken into account using the diagrammatic Brückner approach. For this purpose we introduced the interaction matrix, which describes the simultaneous interaction of a particle with the hard-core constraint and the additional interaction. The Bethe-Salpeter equation for the ladder-diagrams is replaced by an equivalent matrix valued equation, describing all possible infinite 2-particle scattering processes. The solution of this equation is called the scattering matrix. We derived the corrections to the anti-bound state at high energies due to the additional interactions as well as the new low energy contribution to the self-energy. As an example we examined the Heisenberg ladder and chain in the limit of strong dimer coupling and how the additional interactions between the triplon excitations change the specific form of the spectral function. It turns out, that the main reason for the line shape broadening is the hard-core constraint, as expected. However, the full treatment of the interactions leads to additional scattering processes, which slightly shift the peak and decrease the coherence of the excitation further, especially for the gap mode. Thus, for a highly quantitative analysis, e.g. when comparing different theoretical approaches, the additional interactions can play a significant role.

8 Summary & Outlook

8.1 Summary

In this thesis we investigated anomalous line shape broadening and finite temperature quantum coherence in magnets. To obtain a valid description of the finite temperature correlations, we developed the diagrammatic Brückner theory for thermal fluctuations. The theory takes into account, that the thermal fluctuations in quantum magnets are hard-core bosons, by including an infinite on-site interaction into the standard bosonic description. The exact expression for the self-energy in first order of $\exp(-\beta\Delta)$ was derived for gapped systems. In particular, we identified a subtle but important contribution to the real part of the self-energy, which comes from an anti-bound state at infinite energy. The method yields the single particle spectral function, which is directly connected to the experimentally relevant dynamic structure factor.
We benchmarked the method by using a one dimensional nearest neighbor chain of hard-core bosons, for which a mapping to non-interacting fermions is available. The comparison of the spectral function calculated by the fermionic approach to the diagrammatic Brückner theory was very good. Especially, the results for the thermal occupation function and for the sum rules showed an excellent agreement with the fermionic results, even beyond the low temperature regime. For higher temperatures this agreement was also attributed to the property, that the Brückner theory provides a conserving approximation in the sense of Kadanoff and Baym.
With minor changes the theory is also applicable for excitations with multiple flavors. It was shown, that for multiple flavors, the results for the thermal occupation function and for the sum rules are not as satisfying as in the the single flavor case, but they are still correct in the expected first order of $\exp(-\beta\Delta)$. We investigated this phenomenon in more detail, by computing the spectral function also for a finite on-site repulsion. It was deduced, that the concept of conserving approximations is not directly applicable to hard-core bosonic systems with multiple flavors.
One advantage of the Brückner theory is, that it can be directly combined with effective models coming from various renormalization schemes. We showed how additional interactions and vertex corrections can be included using a mean field approximation. These methods were used to investigate the temperature dependence of the static structure factor of the transverse field Ising model close to a quantum critical point.

A main result of this thesis is the analysis of the quantum magnet $BaCu_2V_2O_8$. In this dimerized system, the threefold degenerate triplon excitations are dispersive along a single axis with a rare ferromagnetic interdimer interaction. For this material we investigated the thermal line-shape broadening and found an excellent agreement between the theoretical prediction and the experimental data.
Additionally we showed, that the Brückner approach is also able to describe correlations in the time domain, by analyzing the quantum magnet copper-nitrate. Specifically we studied the time dependent echo amplitude and compared the experimental results with the diagrammatic results and a statistical model. Here, the Brückner theory provided the most compelling explanation for the observed time dependence.
Finally the effect of additional interactions was addressed in more detail, in order to assess its significance in comparison with the hard-core constraint. To that end, we developed a matrix valued Brückner approach to include the additional interaction for all ladder diagrams. To evaluate the approach, we used the Heisenberg chain and ladder, two models with particular strong two particle interactions, leading to the formation of bound and anti-bound states in the dynamic structure factor. The analysis demonstrated, that for a quantitative description of the decay, the additional interaction should be taken into account. But the main mechanism behind the observed correlations are the hard-core bosonic scattering processes.

8.2 Outlook

This thesis shows, that the Brückner theory is a promising route to understand dynamic correlation and to deepen our understanding of quantum coherence at finite temperature. We emphasize, that the presented diagrammatic approach does not rely on integrable field theories or other properties specific to one dimension. Thus, various extensions suggest themselves. Most importantly, it is conceptually possible to extend the presented approach to higher dimensions and to different models which are currently subject of ongoing experimental research, see for instance Refs. [33, 34].
Further extensions concern the addition of diagrams with two backward running propagators providing an approximation exact up to order $\exp(-2\beta\Delta)$.
An interesting question is, whether it is possible to increase the fraction of non-trivial scattering processes to further enhance the quantum character of the excitations at finite temperature. This could be a promising route to extend the quantum description of materials further to higher temperatures, paving the way for potential quantum applications.

Appendix

A Diagrammatic perturbation theory

To introduce the diagrammatic perturbation theory for bosons, we start from a bilinear Hamiltonian in a translational invariant system. In that case we can use a Fourier-transformation in order to diagonalize the problem,

$$H_0 = \sum_q \omega(q) b_q^\dagger b_q. \tag{A.1}$$

where q denotes momentum and $\omega(q)$ is the dispersion relation. The system H_0 is perturbed by a quartic interaction,

$$H_V = \frac{1}{2} \sum_{klmn} V_{mn}^{kl} b_m^\dagger b_n^\dagger b_k b_l \,. \tag{A.2}$$

We introduce the thermodynamic Green function for bosons

$$G(\tau) = - \left\langle T \left[A(-i\tau), B(0) \right] \right\rangle \tag{A.3}$$

with the observables $A(-i\tau) = \exp(H\tau) A \exp(-H\tau)$ and B. The time ordering super operator T is defined by,

$$T \left[A(-i\tau), B(-i\tau') \right] = A(-i\tau) B(-i\tau') \theta(\tau - \tau') - B(-i\tau') A(-i\tau) \theta(\tau' - \tau). \tag{A.4}$$

A short calculation shows that $G(\tau)$ is a periodic function of τ with periodicity β,

$$G(\tau) = G(\tau + \beta). \tag{A.5}$$

Hence we can perform a Fourier analysis,

$$G(\tau) = \frac{1}{\beta} \sum_\nu G(i\omega_\nu) e^{i\omega_\nu \tau} \tag{A.6}$$

where $\omega_\nu = 2\pi\nu/\beta$, with$\nu \in \mathbb{Z}$, are the bosonic Matsubara frequencies. For $G(i\omega_\nu)$ there exists a Hilbert representation,

$$G(i\omega_\nu) = \int_{-\infty}^{\infty} \frac{A(x)}{i\omega_\nu - x} \mathrm{d}x. \tag{A.7}$$

Using a Lehmann representation, one can show that the spectral function $A(x)$ of the thermal Green function equals the spectral function for the retarded, advanced and causal Green functions,

$$A(x) = \frac{1}{Z} \sum_{m,n} \left(e^{-\beta E_m} - e^{-\beta E_n}\right) A_{mn} B_{mn} \delta(x - (E_n - E_m)) \tag{A.8}$$

The spectral function can be obtained via analytical continuation $i\omega_\nu \to \omega + 0^+$ of the Green function

$$A(\omega) = \frac{1}{\pi} \lim_{\delta \to 0+} \mathrm{Im} G(\omega + i\delta) \tag{A.9}$$

For $A = b_k^\dagger$ and $B = b_k$ the Green function describes the propagation of a single particle. The free propagators, i.e. $H_V = 0$, are trivial

$$G_{k,0}(i\omega_\nu) = \frac{1}{i\omega_\nu - \omega(k)}. \tag{A.10}$$

The free propagator is depicted as an arrow in diagrammatic perturbation theory, see Fig. A.1, symbolizing the propagation of a free particle.

Figure A.1: Depiction of the free propagator.

In order to calculate the properties of the full Hamiltonian $H = H_0 + H_V$ we study the full propagator $G_k(i\omega_\nu)$ in the interacting system. In general, the full propagator contains all information about the single particle dynamics of the Hamiltonian H. It is depicted as a double arrow in diagrammatic perturbation theory, see Fig. A.2.

Figure A.2: Depiction of the full propagator.

For a general two body interaction H_V, the full propagator is unknown. Fortunately, it can be expanded in terms of bare propagators $G_{k,0}(i\omega_\nu)$ and interaction vertices. An interaction vertex is an interaction matrix element V_{mn}^{kl}, with two ingoing particles with momenta k, l and two outgoing momenta m, n. In case of translational invariance, the total momentum is a conserved quantity, so that $k + l = m + n$ holds. The interaction vertex is depicted as a wiggly line, see Fig. A.3.

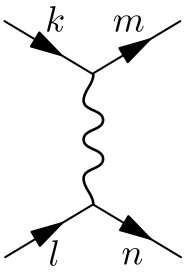

Figure A.3: Depiction of an interaction matrix element.

The free propagator is given by

$$G_{k,0}(i\omega_k) = G_0(K) = \frac{1}{i\omega_k - \omega(k)} \tag{A.11}$$

We assume that the system is translational invariant in space and time, so that the total 2-momentum is conserved. Applying perturbation theory for the full propagator results in the following rules for the contribution to the full single particle propagator of order n

Feynman Rules for $G_p(i\omega_p)$

- Draw all open, connected diagrams with n vertices, which are topologicaly different
- Every vertex contributes with $V^{kl}_{mn}\frac{1}{\beta}\delta_{K+L,M+N}$
- Solid inner lines: $-\delta_{K,L}G_0(K) = \frac{-1}{i\omega_k - \omega(k)}$ (note the difference between the dispersion $\omega(k)$ an the Matsubara frequency ω_k).
- Non Propagating lines have an extra factor $e^{i\omega_\nu 0+}$
- Solid outer lines: $-\delta_{K,P}G_0(K)$
- Sum over all inner momenta and frequencies
- Global prefactor $(-1)^{n+1}$

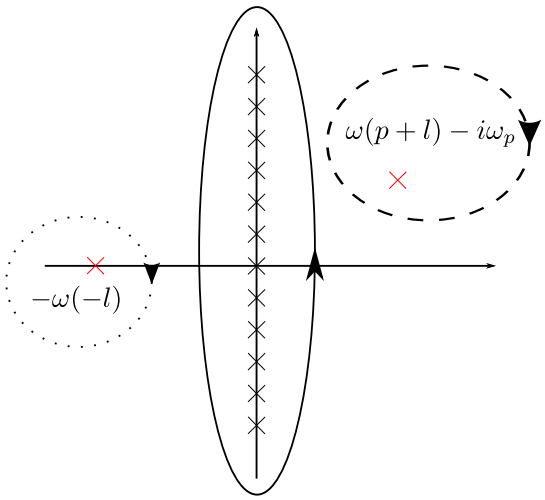

Figure B.1: Position of singularities for the Matsubara sum.

B Matsubara summations

B.1 $M(P)$

We concentrate on the sum $M(P) = \frac{1}{N\beta} \sum_L G_0(P+L)G_0(-L)$. First we want to calculate the matsubara sum,

$$M(P) = \frac{1}{N} \sum_l \frac{1}{\beta} \sum_{i\omega_l} \frac{1}{i\omega_p + i\omega_l - \omega(p+l)} \cdot \frac{1}{-i\omega_l - \omega(-l)} \tag{B.1a}$$

$$= \frac{1}{N} \sum_l \frac{1}{2\pi i} \oint \frac{1}{i\omega_p + \omega - \omega(p+l)} \cdot \frac{1}{-\omega - \omega(-l)} \cdot \frac{1}{e^{\beta\omega} - 1} \tag{B.1b}$$

$$= \frac{1}{N} \sum_l \frac{-1}{2\pi i} \oint \frac{1}{\omega - [\omega(p+l) - i\omega_p]} \cdot \frac{1}{\omega - [-\omega(-l)]} \cdot \frac{1}{e^{\beta\omega} - 1} \tag{B.1c}$$

The integral follows the solid line in Fig. B.1. The integral over the solid line equals the integral over the dashed and the dotted lines (take note, that the integrals rotate in opposite directions), due to the residue theorem. Hence we conclude for $M(P)$,

$$\begin{aligned} M(P) &= \frac{1}{N} \sum_l \left(\frac{1}{[\omega(p+l) - i\omega_p] - [-\omega(-l)]} \cdot \frac{1}{e^{\beta[\omega(p+l) - i\omega_p]} - 1} \right. \\ &\quad \left. + \frac{1}{[-\omega(-l)] - [\omega(p+l) - i\omega_p]} \cdot \frac{1}{e^{\beta[-\omega(-l)]} - 1} \right) \\ &= \frac{1}{N} \sum_l \left(\frac{-1}{i\omega_p - [\omega(-l) + \omega(p+l)]} \cdot \frac{1}{e^{\beta\omega(p+l)} - 1} \right. \\ &\quad \left. + \frac{1}{i\omega_p - [\omega(-l) + \omega(p+l)]} \cdot \frac{1}{e^{-\beta\omega(-l)} - 1} \right) \\ &= \frac{1}{N} \sum_l \frac{1}{i\omega_p - [\omega(-l) + \omega(p+l)]} \cdot \left(\frac{1}{e^{-\beta\omega(-l)} - 1} - \frac{1}{e^{\beta\omega(p+l)} - 1} \right) \end{aligned} \tag{B.2}$$

Note, that $\exp(-\beta i\omega_p) = \exp(-i2\pi n) = 1$ holds.

B.2 Self-energy

We sum over all Matsubara frequencies $i\omega_k$ in,

$$\Sigma(P) = \frac{-2}{N\beta} \sum_K G_0(K) \cdot e^{i\omega_k 0^+} \left(\int_{-\infty}^{\infty} \frac{\bar{\rho}_{p+k}(x)}{i\omega_p + i\omega_k - x} \mathrm{d}x + U \right). \tag{B.3}$$

We start with the second term $\propto U$, which yields

$$\Sigma(P) = \frac{-2}{N\beta} \sum_k \sum_{i\omega_k} \frac{1}{i\omega_k - \omega(k)} e^{i\omega_k 0+} \int_{-\infty}^{\infty} \frac{\bar{\rho}_{p+k}(x)}{i\omega_p + i\omega_k - x} \mathrm{d}x + \frac{2}{N} \sum_k \frac{U}{e^{\beta\omega(k)} - 1}. \tag{B.4}$$

And the first part yields

$$\frac{-2}{N\beta} \sum_k \sum_{i\omega_k} \frac{1}{i\omega_k - \omega(k)} e^{i\omega_k 0+} \int_{-\infty}^{\infty} \mathrm{d}x \frac{\bar{\rho}_{p+k}(x)}{i\omega_k - (x - i\omega_p)} \tag{B.5}$$

$$= \frac{-2}{N} \sum_k \int_{-\infty}^{\infty} \frac{1}{2\pi i} \oint_C \frac{e^{\omega 0+}}{\omega - \omega(k)} \frac{\bar{\rho}_{p+k}(x)}{\omega - (x - i\omega_p)} \cdot \frac{1}{e^{\beta\omega} - 1} \mathrm{d}\omega \mathrm{d}x \tag{B.6}$$

$$= \frac{2}{N} \sum_k \int_{-\infty}^{\infty} \frac{1}{2\pi i} \oint_{C'} \frac{e^{\omega 0+}}{\omega - \omega(k)} \cdot \frac{\bar{\rho}_{p+k}(x)}{\omega - (x - i\omega_p)} \cdot \frac{1}{e^{\beta\omega} - 1} \mathrm{d}\omega \mathrm{d}x \tag{B.7}$$

$$= \frac{2}{N} \sum_k \int_{-\infty}^{\infty} \left[\frac{\bar{\rho}_{p+k}(x)}{\omega(k) - (x - i\omega_p)} \cdot \frac{1}{e^{\beta\omega(k)} - 1} + \frac{\bar{\rho}_{p+k}(x)}{(x - i\omega_p) - \omega(k)} \cdot \frac{1}{e^{\beta x} - 1} \right] \mathrm{d}x \tag{B.8}$$

$$= \frac{2}{N} \sum_k \int_{-\infty}^{\infty} \frac{\bar{\rho}_{p+k}(x)}{i\omega_p - [x - \omega(k)]} \left[\frac{1}{e^{\beta\omega(k)} - 1} - \frac{1}{e^{\beta x} - 1} \right] \mathrm{d}x \tag{B.9}$$

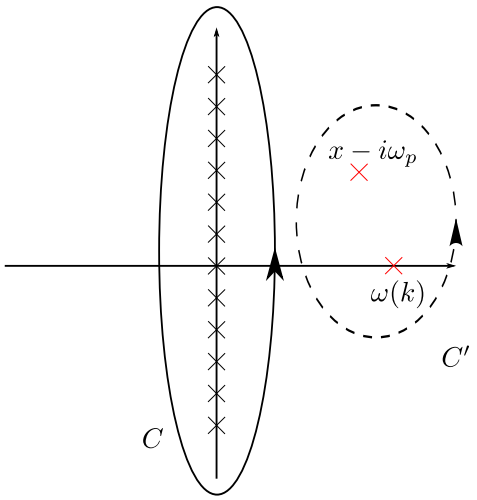

Figure B.2: Position of singularities for the Matsubara sum of the self-energy.

C Bilinear expectation values

We want to calculate the quantitiy $\langle b_k^\dagger, b_k \rangle$. Recall the thermodynamic Greenfunction in time-domain

$$G_k(\tau) = -\left\langle T\left[b_k(-i\tau), b_k^\dagger(0)\right]\right\rangle. \tag{C.1}$$

We want to show the identity

$$\langle b_k^\dagger b_k \rangle = \int_{-\infty}^{\infty} \frac{A(\omega)}{e^{\beta\omega} - 1}, \tag{C.2}$$

and use

$$\lim_{\tau\to 0+} G_k(-\tau) = \lim_{\tau\to 0+} -\langle -b_k^\dagger(0) b_k(i\tau)\rangle \tag{C.3a}$$

$$= \lim_{\tau\to 0+} \langle b_k^\dagger e^{-H\tau} b_k e^{H\tau}\rangle \tag{C.3b}$$

$$= \langle b_k^\dagger b_k \rangle. \tag{C.3c}$$

Thus we conclude

$$\langle b_k^\dagger b_k \rangle = \lim_{\tau\to 0+} G_k(-\tau) \tag{C.4a}$$

$$= \lim_{\tau\to 0+} \frac{1}{\beta} \sum_\nu G_k(i\omega_\nu) e^{-i\omega_\nu \tau} \tag{C.4b}$$

$$= \lim_{\tau\to 0+} \frac{1}{2\pi i} \oint_C \frac{G_k(z) e^{\tau z}}{e^{\beta z} - 1} \mathrm{d}z. \tag{C.4c}$$

Where the contour C includes the whole imaginary axis but no poles of $G_k(z)$ (which are on the real axis). Next we insert the spectral representation of $G_k(z)$

$$G_k(z) = \int_{-\infty}^{\infty} \frac{A_k(\omega)}{z-\omega} \mathrm{d}\omega, \tag{C.5}$$

which leads to

$$\langle b_k^\dagger b_k \rangle = \lim_{\tau \to 0+} \frac{1}{2\pi i} \int_{-\infty}^{\infty} \mathrm{d}\omega \oint_C \mathrm{d}z \frac{A_k(\omega)}{z-\omega} \cdot \frac{e^{\tau z}}{e^{\beta z}-1}. \tag{C.6}$$

Since $A_k(\omega)$ has no poles in the imaginary plane, we can replace the countour C with a negative countour integral C', which encloses the point $z = \omega$. We then use the residue theorem to calculate this integral explicitly

$$\langle b_k^\dagger b_k \rangle = \lim_{\tau \to 0+} \frac{1}{2\pi i} \int_{-\infty}^{\infty} \mathrm{d}\omega \int_{C'} \mathrm{d}z \frac{A_k(\omega)}{z-\omega} \cdot \frac{e^{\tau z}}{e^{\beta z}-1} \tag{C.7a}$$

$$= \lim_{\tau \to 0+} \int_{-\infty}^{\infty} \mathrm{d}\omega \frac{A_k(\omega) e^{\tau \omega}}{e^{\beta \omega}-1} \tag{C.7b}$$

$$= \int_{-\infty}^{\infty} \mathrm{d}\omega \frac{A_k(\omega)}{e^{\beta \omega}-1} \tag{C.7c}$$

With this we can also calculate bilinear expectation values in real space explicitly

$$\langle b_j^\dagger b_{j+d} \rangle = \frac{1}{N} \sum_j \langle b_j^\dagger b_{j+d} \rangle \tag{C.8a}$$

$$= \frac{1}{N^2} \sum_{j,k,k'} \langle b_k^\dagger b_{k'} \rangle e^{ikj} e^{-ik'(j+d)} \tag{C.8b}$$

$$= \frac{1}{N} \sum_k \langle b_k^\dagger b_k \rangle e^{-ikd} \tag{C.8c}$$

$$= \int_{-\infty}^{\infty} \mathrm{d}\omega \frac{A_k(\omega)}{e^{\beta \omega}-1} e^{-ikd}. \tag{C.8d}$$

D Generalization of two-particle interactions in the TFIM

We want to generalize the mean-field decoupling in Eq. (4.43) to operators the form

$$b_j^\dagger b_{j+d_1}^\dagger b_{j+d_1} b_{j+d_2} \approx \langle b_j^\dagger b_{j+d_1}\rangle b_{j+d_1}^\dagger b_{j+d_2} \tag{D.1a}$$
$$+ \langle b_j^\dagger b_{j+d_2}\rangle b_{j+d_1}^\dagger b_{j+d_1} \tag{D.1b}$$
$$+ \langle b_{j+d_1}^\dagger b_{j+d_1}\rangle b_j^\dagger b_{j+d_2} \tag{D.1c}$$
$$+ \langle b_{j+d_1}^\dagger b_{j+d_2}\rangle b_j^\dagger b_{j+d_1}, \tag{D.1d}$$

where $0 < d_1 < d_2$. Note the definition of $h(d)$ in Eq. (4.21). Next we compute,

$$b_j^\dagger b_{j+d_1}^\dagger b_{j+d_1} b_{j+d_2} \approx h(d_1) b_{j+d_1}^\dagger b_{j+d_2} \tag{D.2a}$$
$$+ h(d_2) b_{j+d_1}^\dagger b_{j+d_1} \tag{D.2b}$$
$$+ h(0) b_j^\dagger b_{j+d_2} \tag{D.2c}$$
$$+ h(d_2 - d_1) b_j^\dagger b_{j+d_1}. \tag{D.2d}$$

Including the h.c. terms leads to

$$2\sum_j \left(b_j^\dagger b_{j+d_1}^\dagger b_{j+d_1} b_{j+d_2} + \text{h.c.}\right) \tag{D.3a}$$
$$= 2\sum_q \left(2h(d_1)\cos([d_2 - d_1]q) + 2h(d_2) + 2h(0)\cos(d_2 q) + 2h(d_2 - d_1)\cos(d_1 q)\right) b_q^\dagger b_q \tag{D.3b}$$
$$= 4\sum_q \left(h(d_1)\cos([d_2 - d_1]q) + h(d_2) + h(0)\cos(d_2 q) + h(d_2 - d_1)\cos(d_1 q)\right) b_q^\dagger b_q, \tag{D.3c}$$

so that the correction to the dispersion is given by

$$\tilde{\omega}(q) = \omega(q) + \sum_{d_2=2}^{\infty} 4t_{d_2}^{+-}(-1)^{d_2} \sum_{d_1=1}^{d_2-1} \left(h(d_1)\cos([d_2 - d_1]q) + h(d_2) + h(0)\cos(d_2 q) + h(d_2 - d_1)\cos(d_1 q)\right). \tag{D.4}$$

E Vertex corrections in the TFIM

For the TFIM we need a CUT to transform the observables to effective observables:

$$S_l^+ \to S_{l,\text{eff}}^+ = t_0 S_l^+ + t_1 \left(S_{l+1}^+ + S_{l-1}^+\right) + \dots \tag{E.1}$$

The dots imply terms further away from l and multi particle contributions. We are interested in the Fourier transformed spin operator

$$S_q^+ = \frac{1}{\sqrt{N}} \sum_l e^{-iql} S_l^+ \to S_{q,\text{eff}}^+ = \frac{1}{\sqrt{N}} \sum_l e^{-iql} S_{l,\text{eff}}^+. \tag{E.2}$$

The terms consisting of single S^+ operators are easy to incorporate

$$S_{q,\text{eff}}^+ = \frac{1}{\sqrt{N}} \sum_l e^{-iql} S_l^+ \left(t_0 + \sum_{d=1}^{\infty} 2t_d \cos(dq) + \dots \right) \tag{E.3}$$

There are also other terms contributing, i.e. conditional excitations. From these terms only a certain kind matter in first order in $\exp(-\beta\Delta)$. Namely:

$$\sum_{\{j,k,m\dots\},d} t^d_{\{j,k,m\dots\}} S^+_{l+d} \sigma^z_{l+j} \sigma^z_{l+k} \sigma^z_{l+m} \cdots \tag{E.4}$$

and

$$\sum_{\{j,k,m\dots\},d_1,d_2,d_3} t^{d_1,d_2,d_3}_{\{j,k,m\dots\}} S^+_{l+d_1} S^+_{l+d_2} S^-_{l+d_3} \sigma^z_{l+j} \sigma^z_{l+k} \sigma^z_{l+m} \cdots \tag{E.5}$$

where $\{j,k,m\dots\}$ denotes a multiindex for all sigma z matrices in the term. We use a mean-field decoupling to deal with these terms, for the first kind:

$$\begin{aligned}
t^d_{\{j,k,m\dots\}} S^+_{l+d} \sigma^z_{l+j} \sigma^z_{l+k} \sigma^z_{l+m} \cdots \approx\ & t^d_{\{j,k,m\dots\}} S^+_{l+d} (-1)^{\#\{j,k,m\dots\}} && \text{(E.6a)}\\
& + t^d_{\{j,k,m\dots\}} S^+_{l+d} \left(2 \left\langle S^+_{l+j} S^-_{l+j} \right\rangle\right) (-1)^{\#\{j,k,m\dots\}-1} && \text{(E.6b)}\\
& + t^d_{\{j,k,m\dots\}} S^+_{l+j} \left(2 \left\langle S^+_{l+d} S^-_{l+j} \right\rangle\right) (-1)^{\#\{j,k,m\dots\}-1} && \text{(E.6c)}\\
& + \dots && \text{(E.6d)}
\end{aligned}$$

Where the dots imply the exchange of j with all other indices for the last two terms. Take note, that the expression $\#\{j,k,m\dots\}$ refers to the total number of indices $\{j,k,m\dots\}$ present in the operator. And for the second kind:

$$\begin{aligned}
t^{d_1,d_2,d_3}_{\{j,k,m\dots\}} S^+_{l+d_1} S^+_{l+d_2} S^-_{l+d_3} \sigma^z_{l+j} \sigma^z_{l+k} \sigma^z_{l+m} \cdots \approx\ & t^{d_1,d_2,d_3}_{\{j,k,m\dots\}} (-1)^{\#\{j,k,m\dots\}} \\
& \cdot \left(S^+_{l+d_1} \left\langle S^+_{l+d_2} S^-_{l+d_3} \right\rangle + S^+_{l+d_2} \left\langle S^+_{l+d_1} S^-_{l+d_3} \right\rangle \right).
\end{aligned}$$

We introduce the shortcut

$$\left\langle S^+_d S^-_j \right\rangle = \tau(d-j) = \tau(j-d) \tag{E.7}$$

and calculate the Fourier transformation

$$\begin{aligned}
&\frac{1}{\sqrt{N}}\sum_l e^{-iql}\sum_{\{j,k,m\dots\},d} t^d_{\{j,k,m\dots\}} S^+_{l+d}\sigma^z_j\sigma^z_k\sigma^z_m\dots \\
&= \frac{1}{\sqrt{N}}\sum_l e^{-iql} S^+_l \sum_{\{j,k,m\dots\},d} t^d_{\{j,k,m\dots\}} \Bigg[e^{iqd}(-1)^{\#\{j,k,m\dots\}} \\
&+ (-1)^{\#\{j,k,m\dots\}-1} 2 \sum_{\xi\in\{j,k,m\dots\}} e^{iqd}\tau(0) + e^{iq\xi}\tau(d-\xi)\Bigg]
\end{aligned} \tag{E.8}$$

and

$$\begin{aligned}
&\frac{1}{\sqrt{N}}\sum_l e^{-iql}\sum_{\{j,k,m\dots\},d_1,d_2,d_3} t^{d_1,d_2,d_3}_{\{j,k,m\dots\}} S^+_{l+d_1}S^+_{l+d_2}S^-_{l+d_3}\sigma^z_{l+j}\sigma^z_{l+k}\sigma^z_{l+m}\dots \\
&= \frac{1}{\sqrt{N}}\sum_l e^{-iql} S^+_l \sum_{\{j,k,m\dots\},d_1,d_2,d_3} t^{d_1,d_2,d_3}_{\{j,k,m\dots\}}(-1)^{\#\{j,k,m\dots\}}\left[e^{iqd_1}\tau(d_2-d_3)+e^{iqd_2}\tau(d_1-d_3)\right]
\end{aligned} \tag{E.9}$$

Now the vertex correction is given by the l-independent prefactor of the S^+_l operator.

F Complete diagrammatic treatment of additional interactions with flavored particles

In case of flavored particles, the most general two body interaction reads

$$V = \sum_j \sum_{d_1,d_2,d_3} \sum_{\alpha,\beta,\gamma,\delta} V^{\alpha\beta}_{\gamma\delta}(d_1,d_2,d_3) t^\dagger_{j,\alpha} t^\dagger_{j+d_1,\beta} t_{j+d_2,\gamma} t_{j+d_2+d_3,\delta}. \tag{F.1}$$

Where $d_1, d_2, d_3 \in \mathbb{Z}$ and $d_1 \neq 0$ and $d_3 \neq 0$ holds due to the hard-core constraint. The flavor indices are given by $\alpha, \beta, \gamma, \delta$. Note, that hermiticity now implies a different condition for the matrix elements,

$$V^{\alpha\beta}_{\gamma\delta}(d_1,d_2,d_3) \overset{!}{=} V^{\gamma\delta\star}_{\alpha\beta}(d_3,-d_2,d_1). \tag{F.2}$$

This symmetry *can* be chosen, but even if the matrix does not fulfil this property, the corresponding interaction would still be hermitian. In momentum space the interaction reads

$$V = \frac{1}{N}\sum_{p,k,q}\sum_{d_1,d_2,d_3}\sum_{\alpha,\beta,\gamma,\delta} V^{\alpha\beta}_{\gamma\delta}(d_1,d_2,d_3) t^\dagger_{p+k,\alpha} t^\dagger_{-k,\beta} t_{p+q,\gamma} t_{-q,\delta} \cdot e^{-id_2p} e^{-id_1k} e^{id_3q} \tag{F.3}$$

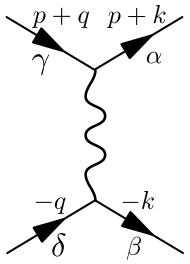

Figure F.1: Diagrammatic representation of Eq. (F.5)

Note the special symmetry in case two flavor indices are the same

$$\frac{1}{N}\sum_{p,k,q}\sum_{d_1,d_2,d_3}\sum_{\alpha,\beta} V^{\alpha\beta}_{\beta\alpha}(d_1,d_2,d_3)t^\dagger_{p+k,\alpha}t^\dagger_{-k,\beta}t_{p+q,\beta}t_{-q,\alpha}\cdot e^{-id_2p}e^{-id_1k}e^{id_3q}$$

$$\overset{\alpha\leftrightarrow\beta}{=}\frac{1}{N}\sum_{p,k,q}\sum_{d_1,d_2,d_3}\sum_{\alpha,\beta} V^{\beta\alpha}_{\alpha\beta}(d_1,d_2,d_3)t^\dagger_{p+k,\beta}t^\dagger_{-k,\alpha}t_{p+q,\alpha}t_{-q,\beta}\cdot e^{-id_2p}e^{-id_1k}e^{id_3q}$$

$$\overset{k\to -k-p}{}$$

$$\overset{q\to -q-p}{=}\frac{1}{N}\sum_{p,k,q}\sum_{d_1,d_2,d_3}\sum_{\alpha,\beta} V^{\beta\alpha}_{\alpha\beta}(d_1,d_2,d_3)t^\dagger_{-k,\beta}t^\dagger_{p+k,\alpha}t_{-q,\alpha}t_{p+q,\beta}\cdot e^{-id_2p}e^{-id_1(-k-p)}e^{id_3(-q-p)}$$

$$\overset{d_2\to d_2+d_1-d_3}{=}\frac{1}{N}\sum_{p,k,q}\sum_{d_1,d_2,d_3}\sum_{\alpha,\beta} V^{\beta\alpha}_{\alpha\beta}(d_1,d_2+d_1-d_3,d_3)t^\dagger_{p+k,\alpha}t^\dagger_{-k,\beta}t_{p+q,\beta}t_{-q,\alpha}\cdot e^{-id_2p}e^{-id_1(-k)}e^{id_3(-q)}$$

$$\overset{d_1\to -d_1}{}$$

$$\overset{d_3\to -d_3}{=}\frac{1}{N}\sum_{p,k,q}\sum_{d_1,d_2,d_3}\sum_{\alpha,\beta} V^{\beta\alpha}_{\alpha\beta}(-d_1,d_2-d_1+d_3,-d_3)t^\dagger_{p+k,\alpha}t^\dagger_{-k,\beta}t_{p+q,\beta}t_{-q,\alpha}\cdot e^{-id_2p}e^{-id_1k}e^{id_3q}.$$

Hence we have the symmetry

$$V^{\alpha\beta}_{\beta\alpha}(d_1,d_2,d_3) = V^{\beta\alpha}_{\alpha\beta}(-d_1,d_2-d_1+d_3,-d_3). \tag{F.4}$$

The interaction vertex in case of flavored particles reads

$$V^{\alpha\beta}_{\gamma\delta}(p,k,q) = \frac{U}{N}+\frac{1}{N}\sum_{d_1,d_2,d_3} V^{\alpha\beta}_{\gamma\delta}(d_1,d_2,d_3)e^{-id_2p}e^{-id_1k}e^{id_3q}. \tag{F.5}$$

The corresponding diagram is represented in Fig. F.1. In order to calculate the Heisenberg ladder, we need two kinds of matrices: $V^{\alpha\alpha}_{\beta\beta}$ for interactions with the same flavor for the ingoing particles and the same flavor for the outgoing particles and $V^{\alpha\beta}_{\alpha\beta}$ for interactions between different flavors.

i	A_i	$h_i(0)$	$h_i(\infty)$	$O_{\min}$	$O_{\max}^{0\mathrm{QP}}$	$O_{\max}^{1\mathrm{QP}}$
0	$\sum_r \mathbb{1}$	$-\frac{3}{4}$	$-\frac{3}{4}-\frac{3x^2}{8}$	0	2	2
1	$\sum_{r,\alpha} t^\dagger_{\alpha,r}t_{\alpha,r}$	1	$1+\frac{3x^2}{4}$	0	0	2
2	$\sum_{r,\alpha\neq\beta} t^\dagger_{\alpha,r}t^\dagger_{\alpha,r+1}t_{\beta,r}t_{\beta,r+1}$	$-\frac{x}{2}$	$-\frac{x}{2}+\frac{x^2}{8}$	1	0	0
3	$\sum_{r,\alpha\neq\beta} t^\dagger_{\alpha,r}t^\dagger_{\beta,r+1}t_{\beta,r}t_{\alpha,r+1}$	$\frac{x}{2}$	$\frac{x}{2}$	1	–	–
4	$\sum_{r,\alpha} t^\dagger_{\alpha,r}t^\dagger_{\alpha,r+1}+\mathrm{h.c.}$	$\frac{x}{2}$	0	1	1	1
5	$\sum_{r,\alpha} t^\dagger_{\alpha,r}t_{\alpha,r+1}+\mathrm{h.c.}$	$\frac{x}{2}$	$\frac{x}{2}$	1	–	2
6	$\sum_{r,\alpha\neq\beta} t^\dagger_{\alpha,r+2}t_{\alpha,r}t_{\beta,r+1}t_{\beta,r+2}+t^\dagger_{\alpha,r}t_{\beta,r}t_{\beta,r+1}t_{\alpha,r+2}+\mathrm{h.c.}$	0	0	2	–	–
7	$\sum_{r,\alpha\neq\beta} t^\dagger_{\beta,r+2}t_{\alpha,r}t_{\beta,r+1}t_{\alpha,r+2}+t^\dagger_{\beta,r}t_{\alpha,r}t_{\beta,r+1}t_{\alpha,r+2}+\mathrm{h.c.}$	0	0	2	–	–
8	$\sum_{r,\alpha} t^\dagger_{\alpha,r}t_{\alpha,r+2}+\mathrm{h.c.}$	0	$-\frac{x^2}{8}$	2	–	2
9	$\sum_{r,\alpha} t^\dagger_{\alpha,r+1}t^\dagger_{\alpha,r+2}t_{\alpha,r}t_{\alpha,r+1}+\mathrm{h.c.}$	0	$\frac{x^2}{4}$	2	–	–
10	$\sum_{r,\alpha\neq\beta} t^\dagger_{\beta,r+1}t^\dagger_{\alpha,r+2}t_{\alpha,r}t_{\beta,r+1}+\mathrm{h.c.}$	0	$\frac{x^2}{8}$	2	–	–
11	$\sum_{r,\alpha} t^\dagger_{\alpha,r}t^\dagger_{\alpha,r+1}t_{\alpha,r}t_{\alpha,r+1}$	0	$-\frac{x^2}{4}$	2	–	–
12	$\sum_{r,\alpha\neq\beta} t^\dagger_{\alpha,r}t^\dagger_{\beta,r+1}t_{\alpha,r}t_{\beta,r+1}$	0	$-\frac{3x^2}{8}$	2	–	–
13	$\sum_{r,\alpha\neq\beta} t^\dagger_{\beta,r+1}t^\dagger_{\beta,r+2}t_{\alpha,r}t_{\alpha,r+1}+\mathrm{h.c.}$	0	$\frac{x^2}{8}$	2	–	–
14	$\sum_{r,\alpha} t^\dagger_{\alpha,r+1}t_{\alpha,r}t_{\alpha,r+1}t_{\alpha,r+2}+\mathrm{h.c.}$	0	0	2	–	–
15	$\sum_{r,\alpha} t^\dagger_{\alpha,r}t^\dagger_{\alpha,r+2}+\mathrm{h.c.}$	0	0	2	–	–
16	$\sum_{r,\alpha\neq\beta} t^\dagger_{\beta,r+1}t_{\alpha,r}t_{\beta,r+1}t_{\alpha,r+2}+\mathrm{h.c.}$	0	0	2	–	–
17	$\sum_{r,\alpha\neq\beta} t^\dagger_{\alpha,r+1}t_{\alpha,r}t_{\beta,r+1}t_{\beta,r+2}+t^\dagger_{\alpha,r+1}t_{\beta,r}t_{\beta,r+1}t_{\alpha,r+2}+\mathrm{h.c.}$	0	0	2	–	–

Figure F.2: Table of the effective operators in the effective Hamiltonian up to order 2 in the parameter x from Ref. [63]. The first column numbers the different operators, the second column includes the actual operators in second quantization. The fourth and the fifth column represent the prefactors of the initial and effective Hamiltonian respectively. The last three columns refer to the reduction of the differential equation system in the deepCUT approach, they are irrelevant for our investigations.

A detailed analysis of the effective Hamiltonian of the Heisenberg ladder is given in Ref. [63]. We will explain how to include the additional interactions based on all interactions up to order 2 from table F.2. Note, that the prefactors of operators, which change the total number of triplons in the system, are zero in the effective Hamiltonian, due to the particle-conserving generator of the CUT.

The first operator refers to the ground state energy of the Hamiltonian at $T = 0$, while the single particle hopping terms define the energy dispersion of the triplons. In this chapter we are mainly interested in the two-particle interactions in the effective Hamiltonian. They are given by the terms 2, 3, 9, 10, 11, 12, and 13. The terms 2 and 13 contribute to the interaction matrix $V^{\alpha\alpha}_{\beta\beta}$ with different flavors $\alpha \neq \beta$. Thus we deduce for these matrix elements

$$2) \quad \Rightarrow V^{\alpha\alpha}_{\beta\beta}(1,0,1) = \frac{-x}{2} + \frac{x^2}{8} \tag{F.6}$$

$$13) \quad \Rightarrow V^{\alpha\alpha}_{\beta\beta}(1,-1,1) = \frac{x^2}{8} \quad \overset{\text{h.c.}}{\Rightarrow} V^{\alpha\alpha}_{\beta\beta}(1,1,1) = \frac{x^2}{8} \tag{F.7}$$

with $\alpha \neq \beta$.

For the case $V^{\alpha\alpha}_{\alpha\alpha}$ we deduce

$$9) \quad \Rightarrow \quad V^{\alpha\alpha}_{\alpha\alpha}(1,-1,1) = \frac{x^2}{8} \quad \overset{\text{h.c.}}{\Rightarrow} V^{\alpha\alpha}_{\alpha\alpha}(1,1,1) = \frac{x^2}{8} \tag{F.8}$$

$$\overset{\text{(F.4)}}{\Rightarrow} \quad V^{\alpha\alpha}_{\alpha\alpha}(-1,-1,-1) = \frac{x^2}{8} \quad \overset{\text{h.c.}}{\Rightarrow} V^{\alpha\alpha}_{\alpha\alpha}(-1,1,-1) = \frac{x^2}{8} \tag{F.9}$$

$$11) \quad \Rightarrow \quad V^{\alpha\alpha}_{\alpha\alpha}(1,0,1) = -\frac{x^2}{8} \quad \overset{\text{(F.4)}}{\Rightarrow} \quad V^{\alpha\alpha}_{\alpha\alpha}(-1,0,-1) = -\frac{x^2}{8}. \tag{F.10}$$

In the case $V^{\alpha\beta}_{\alpha\beta}$ with $\alpha \neq \beta$ we read off

$$3) \quad \Rightarrow \quad V^{\alpha\beta}_{\alpha\beta}(1,1,-1) = \frac{x}{4} \quad \overset{\text{h.c.}}{\Rightarrow} V^{\alpha\beta}_{\alpha\beta}(-1,-1,1) = \frac{x}{4} \tag{F.11}$$

$$10) \quad \Rightarrow \quad V^{\alpha\beta}_{\alpha\beta}(1,0,-1) = \frac{x^2}{8} \quad \overset{\text{h.c.}}{\Rightarrow} V^{\alpha\beta}_{\alpha\beta}(-1,0,1) = \frac{x^2}{8} \tag{F.12}$$

$$12) \quad \Rightarrow \quad V^{\alpha\beta}_{\alpha\beta}(1,0,1) = -\frac{3x^2}{8} \tag{F.13}$$

Note, that we have divided matrix entries that do not contain the hermitian conjugate or the symmetry F.4 by 2 to not over count their contributions. Hence the matrices read:

$$V^{\alpha\alpha}_{\beta\beta} = \begin{pmatrix} 0 & 0 & 0 \\ 0 & \frac{-x}{2} + \frac{x^2}{8}\left(1 + e^{ip} + e{-ip}\right) & 0 \\ 0 & 0 & 0 \end{pmatrix} \tag{F.14}$$

with $\alpha \neq \beta$ and

$$V^{\alpha\alpha}_{\alpha\alpha} = \begin{pmatrix} 0 & 0 & 0 \\ 0 & -\frac{x^2}{8} + \frac{x^2}{8}\left(e^{-ip} + e^{ip}\right) & 0 \\ 0 & 0 & -\frac{x^2}{8} + \frac{x^2}{8}\left(e^{-ip} + e^{ip}\right) \end{pmatrix} \tag{F.15}$$

and

$$V^{\alpha\beta}_{\alpha\beta} = \begin{pmatrix} 0 & 0 & 0 \\ 0 & \frac{-3x^2}{8} & \frac{x}{4}e^{-ip} + \frac{x^2}{8} \\ 0 & \frac{x}{4}e^{ip} + \frac{x^2}{8} & 0 \end{pmatrix} \tag{F.16}$$

Now we need to solve the Bethe-Salpeter equation for the two cases: 1) $V^{\alpha\alpha}_{\beta\beta}$

$$\underline{\underline{\Gamma}}^{\alpha\alpha}_{\beta\beta}(P) = \left(\underline{\underline{\Gamma}}^{\beta\beta}_{0,\alpha\alpha}{}^{-1}(p) + \underline{\underline{N}}(P)\right)^{-1} \tag{F.17}$$

and for 2) $V^{\alpha\beta}_{\alpha\beta}$

$$\underline{\underline{\Gamma}}^{\alpha\beta}_{\alpha\beta}(P) = \left(\underline{\underline{\Gamma}}^{\alpha\beta}_{0,\alpha\beta}{}^{-1}(p) + \underline{\underline{N}}(P)\right)^{-1}. \tag{F.18}$$

Here we assume that the dispersion of the different flavors is the same. This is the case if the SU(2) invariance is not broken within the Hamiltonian. From the Matrix $\underline{\underline{\Gamma}}^{\alpha\alpha}_{\beta\beta}(P)$ we will only need the flavor diagonal parts $\alpha = \beta$, although the non diagonal parts of $V^{\alpha\alpha}_{\beta\beta}$ will play a role during the diagonalization of the matrix. Then we can calculate the Hartree- and Fock-like diagrams for the self-energy. Note, that for $\underline{\underline{\Gamma}}^{\alpha\beta}_{\alpha\beta}(P)$ only the Hartree-like diagrams contribute, while for the $\underline{\underline{\Gamma}}^{\alpha\alpha}_{\alpha\alpha}(P)$ both, the Hartree and the Fock like diagrams contribute. Besides the distinction between the two different $\underline{\underline{\Gamma}}$ matrices, the calculation of the self-energy remains invariant and is shown in chap. 7.

List of Figures

Bibliography

[1] J.M. Kosterlitz, D.J. Thouless, J. Phys. C **5**, L124 (1972)

[2] J.M. Kosterlitz, D.J. Thouless, J. Phys. C **6**, 1181 (1973)

[3] D.J. Thouless, M. Kohmoto, M.P. Nightingale, M. den Nijs, Phys. Rev. Lett. **49**, 405 (1982)

[4] F. Haldane, Phys. Lett. A **93**, 464 (1983)

[5] F.D.M. Haldane, Phys. Rev. Lett. **50**, 1153 (1983)

[6] H.K. Onnes, Commun. Phys. Lab. Univ. Leiden **12**, 120+ (1911)

[7] P. Kapitza, Nature **141**, 74 (1938)

[8] J.F. Allen, A.D. Misener, Nature **141**, 75 (1938)

[9] K. von Klitzing, Rev. Mod. Phys. **58**, 519 (1986)

[10] I. Bloch, J. Dalibard, W. Zwerger, Rev. Mod. Phys. **80**, 885 (2008)

[11] G. Schmid, S. Todo, M. Troyer, A. Dorneich, Phys. Rev. Lett. **88**, 167208 (2002)

[12] C.M. Varma, P.B. Littlewood, S. Schmitt-Rink, E. Abrahams, A.E. Ruckenstein, Phys. Rev. Lett. **63**, 1996 (1989)

[13] P.W. Anderson, Nature Physics **2**, 626 (2006)

[14] S. Ballmann, R. Härtle, P.B. Coto, M. Elbing, M. Mayor, M.R. Bryce, M. Thoss, H.B. Weber, Phys. Rev. Lett. **109**, 056801 (2012)

[15] D.C. Tsui, H.L. Stormer, A.C. Gossard, Phys. Rev. Lett. **48**, 1559 (1982)

[16] R.B. Laughlin, Phys. Rev. Lett. **50**, 1395 (1983)

[17] J. Miller, *Extended Linear Chain Compounds*, 1 (Kluwer Academic Pub, Dor-

drecht, 1982)

[18] M. Hase, I. Terasaki, K. Uchinokura, Phys. Rev. Lett. **70**, 3651 (1993)

[19] S. Sachdev, *Quantum Phase Transitions* (Cambridge University Press, Cambridge, 2001)

[20] T. Giamarchi, C. Rüegg, O. Tchernyshyov, Nature Phys. **4**, 198 (2008)

[21] S. Lovesey, *Theory of neutron scattering from condensed matter* (Oxford University Press, Oxford, 1987)

[22] G. Xu, C. Broholm, D.H. Reich, M.A. Adams, Phys. Rev. Lett. **84**, 4465 (2000)

[23] K.P. Schmidt, C. Knetter, G.S. Uhrig, acta phys. polo. B **34**, 1481 (2003)

[24] D.A. Tennant, B. Lake, A.J.A. James, F.H.L. Essler, S. Notbohm, H.J. Mikeska, J. Fielden, P. Kögerler, P.C. Canfield, M.T.F. Telling, Phys. Rev. B **85**, 014402 (2012)

[25] A.J.A. James, F.H.L. Essler, R.M. Konik, Phys. Rev. B **78**, 094411 (2008)

[26] A.B. Harris, D. Kumar, B.I. Halperin, P.C. Hohenberg, Phys. Rev. B **3**, 961 (1971)

[27] S. Tyč, B.I. Halperin, Phys. Rev. B **42**, 2096 (1990)

[28] S.P. Bayrakci, T. Keller, K. Habicht, B. Keimer, Science **312**, 1926 (2006)

[29] K. Damle, S. Sachdev, Phys. Rev. B **57**, 8307 (1998)

[30] T. Huberman, D.A. Tennant, R.A. Cowley, R. Coldea, C.D. Frost, J. Stat. Mech.: Theor. Exp. **2008**, P05017 (2008)

[31] S.P. Bayrakci, D.A. Tennant, P. Leininger, T. Keller, M.C.R. Gibson, S.D. Wilson, R.J. Birgeneau, B. Keimer, Phys. Rev. Lett. **111**, 017204 (2013)

[32] E.S. Klyushina, A.C. Tiegel, B. Fauseweh, A.T.M.N. Islam, J.T. Park, B. Klemke, A. Honecker, G.S. Uhrig, S.R. Manmana, B. Lake, Phys. Rev. B **93**, 241109 (2016)

[33] D.L. Quintero-Castro, B. Lake, A.T.M.N. Islam, E.M. Wheeler, C. Balz, M. Månsson, K.C. Rule, S. Gvasaliya, A. Zheludev, Phys. Rev. Lett. **109**, 127206 (2012)

[34] C. Rüegg, B. Normand, M. Matsumoto, C. Niedermayer, A. Furrer, K.W. Krämer,

H.U. Güdel, P. Bourges, Y. Sidis, H. Mutka, Phys. Rev. Lett. **95**, 267201 (2005)

[35] K. Fabricius, U. Löw, J. Stolze, Phys. Rev. B **55**, 5833 (1997)

[36] H.J. Mikeska, C. Luckmann, Phys. Rev. B **73**, 184426 (2006)

[37] F.H.L. Essler, R.M. Konik, Phys. Rev. B **78**, 100403 (2008)

[38] F.H.L. Essler, R.M. Konik, J. Stat. Mech.: Theor. Exp. **2009**, P09018 (2009)

[39] A.J.A. James, W.D. Goetze, F.H.L. Essler, Phys. Rev. B **79**, 214408 (2009)

[40] W.D. Goetze, U. Karahasanovic, F.H.L. Essler, Phys. Rev. B **82**, 104417 (2010)

[41] I. Exius, K.P. Schmidt, B. Lake, D.A. Tennant, G.S. Uhrig, Phys. Rev. B **82**, 214410 (2010)

[42] B. Lake, D.A. Tennant, J.S. Caux, T. Barthel, U. Schollwöck, S.E. Nagler, C.D. Frost, Phys. Rev. Lett. **111**, 137205 (2013)

[43] A.C. Tiegel, S.R. Manmana, T. Pruschke, A. Honecker, Phys. Rev. B **90**, 060406 (2014)

[44] J. Jensen, D.L. Quintero-Castro, A.T.M.N. Islam, K.C. Rule, M. Månsson, B. Lake, Phys. Rev. B **89**, 134407 (2014)

[45] J. Jensen, J. Phys. C **17**, 5367 (1984)

[46] J. Jensen, Phys. Rev. B **49**, 11833 (1994)

[47] J. Jensen, Phys. Rev. B **83**, 064420 (2011)

[48] J. Slyom, Adv. Phys. **28**, 201 (1979)

[49] W. Metzner, M. Salmhofer, C. Honerkamp, V. Meden, K. Schönhammer, Rev. Mod. Phys. **84**, 299 (2012)

[50] C. Knetter, G.S. Uhrig, Eur. Phys. J. B **13**, 209 (2000)

[51] C. Knetter, K.P. Schmidt, G.S. Uhrig, J. Phys. A: Math. Gen. **36**, 7889 (2003)

[52] S. Kehrein, *The Flow Equation Approach to Many-Particle Systems*, Vol. 217 of *Springer Tracts in Modern Physics* (Springer, Berlin, 2006)

[53] T. Fischer, S. Duffe, G.S. Uhrig, New J. Phys. **10**, 033048 (2010)

[54] B.S. Shastry, B. Sutherland, Phys. Rev. Lett. **47**, 964 (1981)

[55] G.S. Uhrig, F. Schönfeld, M. Laukamp, E. Dagotto, Eur. Phys. J. B **7**, 67 (1999)

[56] J. Haegeman, S. Michalakis, B. Nachtergaele, T.J. Osborne, N. Schuch, F. Verstraete, Phys. Rev. Lett. **111**, 080401 (2013)

[57] F. Keim, G.S. Uhrig, Eur. Phys. J. B **88**, 154 (2015)

[58] L. Vanderstraeten, F. Verstraete, J. Haegeman, Phys. Rev. B **92**, 125136 (2015)

[59] B. Fauseweh, G.S. Uhrig, Phys. Rev. B **87**, 184406 (2013)

[60] P. Pfeuty, Ann. of Phys. **57**, 79 (1970)

[61] B. Fauseweh, J. Stolze, G.S. Uhrig, Phys. Rev. B **90**, 024428 (2014)

[62] H.Y. Yang, K.P. Schmidt, Europhys. Lett. **94**, 17004 (2011)

[63] H. Krull, N. A. Drescher and G. S. Uhrig, Phys. Rev. B **86**, 125113 (2012)

[64] K. Coester, K.P. Schmidt, Phys. Rev. E **92**, 022118 (2015)

[65] A.L. Fetter, J.D. Walecka, *Quantum Theory of Many-Particle Systems* (Dover Publications, New York, 2003)

[66] L. Kadanoff, G. Baym, D. Pines, *Quantum Statistical Mechanics*, Advanced Books Classics Series (Perseus Books, New York, 1994)

[67] V.N. Kotov, O. Sushkov, Z. Weihong, J. Oitmaa, Phys. Rev. Lett. **80**, 5790 (1998)

[68] O.P. Sushkov, V.N. Kotov, Phys. Rev. Lett. **81**, 1941 (1998)

[69] V.N. Kotov, O.P. Sushkov, R. Eder, Phys. Rev. B **59**, 6266 (1999)

[70] P.V. Shevchenko, A.W. Sandvik, O.P. Sushkov, Phys. Rev. B **61**, 3475 (2000)

[71] H.P. Liu, D.D. Kosloff, Geophys. J. Roy. Astr. S. **67**, 791 (1981)

[72] P. Jordan and E. Wigner, Z. Phys. A **47**, 631 (1928)

[73] J.B. Parkinson, D.J.J. Farnell, *An Introduction to Quantum Spin Systems* (Springer, New York, 2010)

[74] M. Gaudin, Nucl. Phys. **15**, 89 (1960)

[75] O. Derzhko, T. Krokhmalskii, phys. stat. sol. (b) **208**, 221 (1998)

[76] X. Jia, S. Chakravarty, Phys. Rev. B **74**, 172414 (2006)

[77] O. Derzhko, T. Krokhmalskii, J. Stolze, J. Phys. A: Math. Gen. **33**, 3063 (2000)

[78] O. Derzhko, T. Krokhmalskii, J. Stolze, J. Phys. A: Math. Gen. **35**, 3573 (2002)

[79] G. Baym, L.P. Kadanoff, Phys. Rev. **124**, 287 (1961)

[80] G. Baym, Phys. Rev. **127**, 1391 (1962)

[81] M. Troyer, H. Tsunetsugu, D. Würtz, Phys. Rev. B **50**, 13515 (1994)

[82] B. Normand, C. Rüegg, Phys. Rev. B **83**, 054415 (2011)

[83] B. Náfrádi, T. Keller, H. Manaka, A. Zheludev, B. Keimer, Phys. Rev. Lett. **106**, 177202 (2011)

[84] T. Fischer, S. Duffe, G.S. Uhrig, Europhys. Lett. **96**, 47001 (2011)

[85] B. Fauseweh, G.S. Uhrig, Phys. Rev. B **92**, 214417 (2015)

[86] F.J. Wegner, Ann. Physik **3**, 77 (1994)

[87] S.D. Głazek, K.G. Wilson, Phys. Rev. D **48**, 5863 (1993)

[88] S.D. Głazek, K.G. Wilson, Phys. Rev. D **49**, 4214 (1994)

[89] A. Mielke, Eur. Phys. J. B **5**, 605 (1998)

[90] C. Knetter and G.S. Uhrig, Eur. Phys. J. B **13**, 209 (2000)

[91] M. Powalski, G.S. Uhrig, K.P. Schmidt, Phys. Rev. Lett. **115**, 207202 (2015)

[92] K.P. Schmidt, G.S. Uhrig, Phys. Rev. Lett. **90**, 227204 (2003)

[93] S. Streib, P. Kopietz, Phys. Rev. B **92**, 094442 (2015)

[94] Z. He, T. Kyômen, M. Itoh, Phys. Rev. B **69**, 220407(R) (2004)

[95] Y. Singh, D.C. Johnston, Phys. Rev. B **76**, 012407 (2007)

[96] D.C. Johnston, *Handbook of Magnetic Materials*, Vol. 10 (Elsevier Science, Netherlands, 1997)

[97] Z. He, T. Taniyama, M. Itoh, J. Magn. Magn. Mater. **306**, 277 (2006)

[98] S.S. Salunke, A.V. Mahajan, I. Dasgupta, Phys. Rev. B **77**, 012410 (2008)

[99] K. Ghoshray, B. Pahari, B. Bandyopadhyay, R. Sarkar, A. Ghoshray, Phys. Rev. B **71**, 214401 (2005)

[100] C.S. Lue, B.X. Xie, Phys. Rev. B **72**, 052409 (2005)

[101] B. Fauseweh, F. Groitl, T. Keller, K. Rolfs, D.A. Tennant, K. Habicht, G.S. Uhrig, Phys. Rev. B **(In Press)** (2016)

[102] J. Eckert, D.E. Cox, G. Shirane, S.A. Friedberg, H. Kobayashi, Phys. Rev. B **20**, 4596 (1979)

[103] J.C. Bonner, S.A. Friedberg, H. Kobayashi, D.L. Meier, H.W.J. Blöte, Phys. Rev. B **27**, 248 (1983)

[104] D.A. Tennant, C. Broholm, D.H. Reich, S.E. Nagler, G.E. Granroth, T. Barnes, K. Damle, G. Xu, Y. Chen, B.C. Sales, Phys. Rev. B **67**, 054414 (2003)

[105] F. Groitl, T. Keller, K. Rolfs, D.A. Tennant, K. Habicht, Phys. Rev. B **93**, 134404 (2016)

[106] T. Keller, K. Habicht, H. Klann, M. Ohl, H. Schneider, B. Keimer, Appl. Phys. A **74**, S332 (2002)

[107] K. Habicht, R. Golub, F. Mezei, B. Keimer, T. Keller, Phys. Rev. B **69**, 104301 (2004)

[108] R. Gähler, J. Felber, F. Mezei, R. Golub, Phys. Rev. A **58**, 280 (1998)

[109] K. Habicht, R. Golub, R. Gähler, T. Keller, *Space-Time View of Neutron Spin Echo, Correlation Functions and Phonon Focusing, in Neutron Spin Echo Spectroscopy*, Lecture Notes in Physics (Springer-Verlag, Berlin, Heidelberg, 2003)

[110] F. Groitl, Ph.D. thesis, Technische Universität Berlin, Berlin (2012)

[111] S. Sachdev, R.N. Bhatt, Phys. Rev. B **41**, 9323 (1990)

[112] W. Zheng, C.J. Hamer, R.R.P. Singh, S. Trebst, H. Monien, Phys. Rev. B **63**, 144410 (2001)

[113] C. Knetter, K.P. Schmidt, G.S. Uhrig, Eur. Phys. J. B **36**, 525 (2003)

Danksagung

An dieser Stelle möchte ich mich bei Prof. Dr. Götz S. Uhrig für die Vergabe des interessanten Themas und die hervorragende Betreuung und Zusammenarbeit während der Doktorarbeit bedanken.

Prof. Dr. Ilya Eremin und Prof. Dr. Peter Kopietz danke ich für die Begutachtung der Arbeit.

Für die exzellente Zusammenarbeit möchte ich mich besonders bedanken bei Prof. Dr. Joachim Stolze, Prof. Dr. Bella Lake, PD. Dr. Salvatore R. Manmana, Dr. Ekaterina S. Klyushina, Dr. Alexander C. Tiegel und bei Dr. Felix Groitl.

Für die Gastfreundschaft möchte ich mich insbesondere bei Prof. Dr. Bella Lake und Dr. Ekaterina S. Klyushina in Berlin und bei PD. Dr. Salvatore R. Manmana und Dr. Alexander C. Tiegel in Göttingen, herzlich bedanken.

Bei Prof. Dr. Fabian H. L. Essler möchte ich mich für die Gastfreundschaft und die Zusammenarbeit in Oxford bedanken.

Besonders bedanken möchte ich mich auch bei Frederik Keim, für die vielen hilfreichen Gespräche und vor allem dafür, dass er mein bester Freund ist.

Meinen Bürokollegen danke ich für die interessanten Diskussionen, die auch über die Physik hinaus gingen.

Bei Frederik Keim, Leanna Splinter und Dr. Mohsen Hafez-Torbati bedanke ich mich für das Korrekturlesen und die Hilfestellung.

Ich möchte mich auch bei der gesamten Arbeitsgruppe bedanken, die immer Hilfsbereit ist und in der es immer ein angenehmes Arbeitsklima gibt.

Meinen Freunden möchte ich für die Unterstützung und die angenehme Zeit auch außerhalb der Physik danken.

Zuletzt möchte ich meiner Familie und meiner Freundin Marianne danken, dafür das sie jederzeit hinter mir stehen. Ohne euch hätte ich nichts von dem erreicht und ich freue mich jeden Erfolg mit euch teilen zu dürfen.